



저작자표시-비영리-변경금지 2.0 대한민국

이용자는 아래의 조건을 따르는 경우에 한하여 자유롭게

- 이 저작물을 복제, 배포, 전송, 전시, 공연 및 방송할 수 있습니다.

다음과 같은 조건을 따라야 합니다:



저작자표시. 귀하는 원저작자를 표시하여야 합니다.



비영리. 귀하는 이 저작물을 영리 목적으로 이용할 수 없습니다.



변경금지. 귀하는 이 저작물을 개작, 변형 또는 가공할 수 없습니다.

- 귀하는, 이 저작물의 재이용이나 배포의 경우, 이 저작물에 적용된 이용허락조건을 명확하게 나타내어야 합니다.
- 저작권자로부터 별도의 허가를 받으면 이러한 조건들은 적용되지 않습니다.

저작권법에 따른 이용자의 권리는 위의 내용에 의하여 영향을 받지 않습니다.

이것은 [이용허락규약\(Legal Code\)](#)을 이해하기 쉽게 요약한 것입니다.

[Disclaimer](#)

공학박사 학위논문

Synthesis and thermal and charge
transport properties of 2D metal
chalcogenides

2차원 금속 칼코젠 화합물의 합성과 열 및 전하
운송 특성에 대한 연구

2020 년 2 월

서울대학교 대학원

화학생물공학부

차 준 일

Synthesis and thermal and charge transport properties of 2D metal chalcogenides

지도 교수 정 인

이 논문을 공학박사 학위논문으로 제출함
2020 년 02 월

서울대학교 대학원
화학생물공학부
차 준 일

차준일의 공학박사 학위논문을 인준함
2020 년 2 월

위 원 장 _____ 이 규 태 _____ (인)

부위원장 _____ 정 인 _____ (인)

위 원 _____ 이 원 보 _____ (인)

위 원 _____ 박 정 원 _____ (인)

위 원 _____ 김 명 길 _____ (인)

Abstract

Synthesis and thermal and charge transport properties of 2D metal chalcogenides

Joonil Cha

School of Chemical and Biological Engineering

The Graduate School

Seoul National University

Both the rapid growth of the global population and environmental problems ask to develop sustainably and environmentally friendly alternative energy resources. Thermoelectric technology is a good candidate because it directly converts heat into electric energy without releasing undesirable gaseous chemical residues. In order for this technology to be practically and broadly applied, the conversion efficiency of thermoelectrics should be improved, which is a main interest in the field. In this dissertation, I will discuss the new thermoelectric materials and their thermoelectric properties. Among many thermoelectric materials, I will focus on the Pb and Cl introduced n-type SnSe and Cu doped n-type Bi₂Te₃ based compounds. In addition, I discuss the performances of the thermoelectric device with a new

metallization layer for minimal energy loss.

First, I introduce both Cl and PbSe to induce n-type conduction in intrinsic p-type SnSe. PbSe alloying enhances power factor and suppresses lattice thermal conductivity at the same time, giving a highest thermoelectric figure of merit ZT of 1.2 at 823 K for n-type polycrystalline SnSe materials. The best composition is $\text{Sn}_{0.90}\text{Pb}_{0.15}\text{Se}_{0.95}\text{Cl}_{0.05}$. Samples prepared by solid state reaction show a high maximum ZT (ZT_{max}) ~ 1.1 and ~ 0.8 parallel and perpendicular to the press direction of spark plasma sintering, respectively. Remarkably, post ball-mill and annealing processes considerably reduce structural anisotropy, thereby leading to a $ZT_{\text{max}} \sim 1.2$ along both the directions. Hence, the direction giving a ZT_{max} is controllable for this system using the specialized preparation methods for specimens. Spherical aberration-corrected scanning transmission electron microscopic analyses reveal the presence of heavily dense edge dislocations and strain fields, not observed in the p-type counterparts, which contribute to decreasing lattice thermal conductivity.

Second, I report an ultrahigh carrier mobility $\sim 467 \text{ cm}^2 \text{ V}^{-1} \text{ s}^{-1}$ and power factor $\sim 45 \mu\text{W cm}^{-1} \text{ K}^{-2}$ in a new n-type Bi_2Te_3 system with the nominal composition $\text{Cu}_x\text{Bi}_2\text{Te}_{3.17}$ ($x = 0.02, 0.04, \text{ and } 0.06$). It is obtained by reacting Bi_2Te_3 with surplus Cu and Te and subsequently pressing

powder products by spark plasma sintering (SPS). SPS discharges excess Te but stabilizes the high extent of Cu in the structure, giving unique SPS $\text{Cu}_x\text{Bi}_2\text{Te}_{3.17}$ samples. The analyzed composition is close to “ $\text{Cu}_x\text{Bi}_2\text{Te}_3$ ”. Their charge transport properties are highly unusual. Hall carrier concentration and mobility simultaneously increase with the higher mole fraction of Cu contrary to the typical carrier scattering mechanism. As a consequence, the electrical conductivity is considerably enhanced with Cu incorporation. The Seebeck coefficient is nearly unchanged by increasing the Cu content in contrast to the general understanding of inverse relationship between electrical conductivity and Seebeck coefficient. These effects synergistically lead to a record high power factor among all polycrystalline n-type Bi_2Te_3 -based materials.

Third, the most reported thermoelectric modules suffer from considerable power loss due to high electrical and thermal resistivity arising at the interface between thermoelectric legs and metallic contacts. I devised the metallization layer of Fe-Ni alloy seamlessly securing skutterudite materials and metallic electrodes, allowing for a minimal loss of energy transferred from the former. It is applied to an 8 couple thermoelectric module that consists of n-type $(\text{Mm},\text{Sm})_y\text{Co}_4\text{Sb}_{12}$ ($ZT_{\text{max}} = 0.9$) and p-type $\text{DDyFe}_3\text{CoSb}_{12}$ ($ZT_{\text{max}} = 0.7$) skutterudite materials. It performs as a diffusion barrier suppressing chemical reactions to produce a secondary phase at the

interface. Consequent high thermal stability of the module results in the lowest reported electrical contact resistivity of 2.2–2.5 $\mu\text{C cm}^2$ and one of the highest thermoelectric power density of 2.1 W cm^{-2} for a temperature difference of 570 K. Employing a scanning transmission electron microscope equipped with an energy dispersive X-ray spectroscopy detector, we confirmed that it is negligible for atomic diffusion across the interface and resulting formation of a detrimental secondary phase to energy transfer and thermal stability of the thermoelectric module.

Keywords: Thermoelectrics, Polycrystalline, n-type, Tin selenide, Bismuth telluride, Module.

Student Number : 2015-31028

Contents

Chapter 1. Introduction: High performance bulk thermoelectric materials and Dissertation Overview	1
1.1 Introduction of Thermoelectrics	1
1.2 General background	7
1.3 Advanced approaches for thermoelectric materials	12
1.3.1 Doping and alloying	12
1.3.2 Nanostructuring	16
1.3.3 All-scale hierarchical architecturing	20
1.3.4 Discoveries of promising materials with intrinsically low thermal conductivity	24
1.3.5 Increasing the power factor through band engineering	30
1.4 Dissertation Overview	37
 Chapter 2. High Thermoelectric Performance in n-Type Polycrystalline SnSe via Dual Incorporation of Cl and PbSe and Dense Nanostructures	50
2.1 Introduction	50
2.2 Experimental section	56
2.3 Results and discussion	61
2.4 Conclusion	109
2.5 References	111

Chapter 3. Ultrahigh Power Factor and Electron Mobility in n-Type $\text{Bi}_2\text{Te}_{3-x}\%$ Cu Stabilized under Excess Te Condition	121
3.1 Introduction.....	121
3.2 Experimental section.....	128
3.3 Results and discussion	133
3.4 Conclusion	172
3.5 References.....	173
Chapter 4. High Power Density Skutterudite-based Thermoelectric Modules with Ultralow Contact Resistivity Using Fe-Ni Metallization Layers	184
4.1 Introduction.....	184
4.2 Experimental section.....	189
4.3 Results and discussion	193
4.4 Conclusion	214
4.5 References.....	216
Bibliography	227
국문 초록 (Abstract in Korean).....	229

List of Tables

Table 2. 1. Variation in carrier concentration (n_H), mobility (μ_H), and apparent density at room temperature according to the fraction of PbSe alloying (x) for the melt-synthesized (MS) $\text{Sn}_{1.05-x}\text{Pb}_x\text{Se}_{0.95}\text{Cl}_{0.05}$ sample, measured parallel to the press direction of spark plasma sintering (SPS). The n_H and μ_H values were obtained by the Hall effect measurement.	77
Table 2. 2. Comparison of carrier concentration (n_H), mobility (μ_H), and apparent density at room temperature between the ball milled and annealed (BA) and the MS samples. The n_H and μ_H values were obtained by the Hall effect measurement. The measurement direction with respect to the SPS press direction is noted.	90
Table 3. 1. Mass density of the SPS $\text{Cu}_x\text{Bi}_2\text{Te}_{3.17}$ ($x=0.02, 0.04, \text{ and } 0.06$) and control samples.	132
Table 3. 2. The analyzed average chemical composition by EDS before and after SPS process for the title samples with the nominal composition $\text{Cu}_x\text{Bi}_2\text{Te}_{3.17}$ ($x=0.02, 0.04, \text{ and } 0.06$) and the control ingot sample with the nominal composition $\text{Cu}_{0.06}\text{Bi}_2\text{Te}_{3.17}$	138
Table 3. 3. The analyzed average chemical composition by EDS for control samples with the nominal composition $\text{Cu}_x\text{Bi}_2\text{Te}_3$ ($x=0.02 \text{ and } 0.04$) before and after SPS process.	139

Table 3. 4. The refined cell parameters for SPS $\text{Cu}_x\text{Bi}_2\text{Te}_{3.17}$ ($x = 0.02, 0.04,$
and 0.06) and the control SPS $\text{Cu}_x\text{Bi}_2\text{Te}_3$ ($x = 0.02$ and 0.04). 140

Table 4. 1. Specific contact resistance for representative TE modules based
on various classes of materials.202

List of Figures

Figure 1. 1. Schematic illustrations of thermoelectric modules Seebeck effect for power generation and Peltier effect for active refrigeration. (a) Seebeck effect for the power generation, (b) power generation efficiency as a function of average ZT_{ave} , (c) Peltier effect for the active refrigeration, (d) cooling efficiency as a function of average ZT_{ave} . (from Ref [4] Zhang X.; Zhao, L. *J. Materiomics*, **2015**, 1, 92e105)..... 5

Figure 1. 2. Schematic illustration for typical thermoelectric module composed of p-type and n-type legs. (from Ref. [8], Bubnova, O.; Crispin, X. *Energy Environ. Sci.*, **2012**, 5, 9345) 6

Figure 1. 3. Optimizing ZT through tuning the carrier concentration. Good thermoelectric materials are typically heavily doped semiconductors with a carrier concentration between 10^{19} and 10^{21} cm^{-3} . (from Ref. [18], Snyder J.; Toberer E. *Nat. Mater.* **2008**, 7, 105e14.) 10

Figure 1. 4. State-of-the-art bulk thermoelectric materials. The thermoelectric figure-of-merit ZT as a function of temperature and year. (from Ref. [9], Tan, G.; Zhao, L. D.; Kanatzidis, M. G. *Chem. Rev.* **2016**, 116, 12123)..... 11

Figure 1. 5. Schematic representation of various types of point defects: (a) single doping, (b) cross-substitution, and (c) lattice vacancy formation. (from Ref. [9], Tan, G.; Zhao, L. D.; Kanatzidis, M. G. *Chem. Rev.* **2016**, 116, 12123 15

Figure 1. 6. Temperature-dependent (a) charge, (b) thermal transport, and (c) ZT for $\text{AgPb}_{18}\text{SbTe}_{20}$. (d) High resolution TEM image of $\text{AgPb}_{18}\text{SbTe}_{20}$ sample shows “nanodot”. (from Ref. [35], Hsu, K. F.; Loo, S.; Guo, F.; Chen, W.; Dyck, J. S.; Uher, C.; Hogan, T.; Polychroniadis, E. K.; Kanatzidis, M. G. *Science* **2004**, 303, 818). 18

Figure 1. 7. (a) HRTEM image for PbTe-PbS mixed matrix. (b) Schematic illustration for structure of the mixture that shows PbS stripes and dots. (c) Temperature dependent ZT for PbTe-PbS system. (from Ref. [39], Androulakis, J.; Lin, C.; Kong, H.; Uher, C.; Wu, C.; Hogan, T.; Cook, B. A.; Caillat, T.; Paraskevopoulos, K. M.; Kanatzidis, M. G. *J. Am. Chem. Soc.* **2007**, 129, 9780). 19

Figure 1. 8. Schematic illustrations of microstructures for (a) single crystals/ingots and (b) polycrystalline samples with mesoscale grains. The grain size of polycrystalline sample is much lower than those of single crystals/cast ingots. (from Ref. [9], Tan, G.; Zhao, L. D.; Kanatzidis, M. G. *Chem. Rev.* **2016**, 116, 12123). 22

Figure 1. 9. All-scale hierarchical architectures and lattice thermal conductivity: (a) all-scale hierarchical architectures, and (b) cumulativedistribution function of lattice thermal conductivity with respect to the phonon mean free path in Si or PbTe bulk. (from Ref. [10], Zhao, L. D.; Dravid, V.; Kanatzidis, M. G. *Energy Environ. Sci.*, **2014**, 7, 251-268) ...23

Fig. 1. 10. (a) Crystal structure of SnSe at room temperature along the a -axis (gray atoms are Sn and red atoms are Se). (b) Highly distorted SnSe₇ polyhedra showing three short and four long Sn–Se bonds. (c and d) SnSe crystal structures along the b - and c -axis, respectively, presenting the accordion like character. (from Ref. [31], Zhao, L. D.; Dravid, V.; Kanatzidis, M. G. *Energy Environ. Sci.*, **2014**, 7, 251-268)28

Figure 1. 11. Temperature dependent (a) power factor, (b) total thermal conductivity, and figure of merit ZT for single crystal SnSe along different axial direction. The inset of (b) presents their lattice thermal conductivity. (from Ref. [31], Zhao, L. D.; Dravid, V.; Kanatzidis, M. G. *Energy Environ. Sci.*, **2014**, 7, 251-268)29

Figure 1. 12. Hypothetical band structure with a) single and b) multiple peaks. Because the power factor is proportional to the number of populated peaks, the system (b) will have a higher power factor. (from Ref. [61], Sootsman, J. R.; Chung, D. Y.; Kanatzidis, M. G. *Angew. Chem., Int. Ed.* **2009**, 48, 8616–8639.).....33

Figure 1. 13. Relative energy of the valence bands for PbTe_{1-x}Se_x. The two valence bands can converge at around 500 K, leading both the L and Σ bands to contribute transport. (C is a conduction band, L is a low degeneracy hole band, and Σ is a high degeneracy hole band, respectively. (from Ref. [56], Pei, Y.; Shi, X.; LaLonde, A.; Wang, H.; Chen, L.; Snyder. J. Convergence of Electronic Bands for High Performance Bulk Thermoelectrics. *Nature*, **2011**, 473, 66-69).34

Figure 1. 14. Schematic illustration for the resonant level effect on the electronic density of states (DOS). (from Ref. [63], Minnich, A.; Dresselhaus, M.; Ren, Z.; Chen, G. Bulk Nanostructured Thermoelectric Materials: Current Research and Future Prospects. *Energy Environ. Sci.* **2009**, *2*, 466–479.).....35

Figure 1. 15. (a) The small valence band offsets between matrix and second phase allow facile carrier transmission, simultaneously scattering heat carrying phonons at the matrix/second phase interface. (b) Schematically illustration for small band offset in valence band between matrix and second phase. (from Ref. [9], Zhao, L. D.; Dravid, V.; Kanatzidis, M. G. *Energy Environ. Sci.*, **2014**, *7*, 251-268).....36

Figure 2. 1. Typical dense pellets prepared by an SPS process with a typical diameter of 13 mm and a height of ~14 mm. The obtained specimens were cut and polished for measuring electrical (a disk for measurements perpendicular to the SPS press direction and a bar for measurements parallel to the SPS press direction) and thermal transport properties (a small disk).57

Figure 2. 2. Powder X-ray diffraction data for the melt-synthesized $\text{Sn}_{1.05-x}\text{Pb}_x\text{Se}_{0.95}\text{Cl}_{0.05}$ ($x = 0-0.2$) samples compared with the simulated patterns of SnSe (the International Center for Diffraction Data PDF 48-1224) and Sn (PDF 86-2264). Sn Bragg peaks are marked by asterisks.63

Figure 2. 3. (a-c) The cell dimensions and (d) volume as a function of the fraction of PbSe alloying (x) for the $\text{Sn}_{1.05-x}\text{Pb}_x\text{Se}_{0.95}\text{Cl}_{0.05}$ sample ($x = 0, 0.05, 0.10, 0.15, 0.20$)..... 64

Figure 2. 4. (a) SEM image and (b–e) respective elemental maps of Sn, Pb, Se, and Cl atoms depicted in green, cyan, red, and yellow color by EDS for the melt-synthesized $\text{Sn}_{0.90}\text{Pb}_{0.15}\text{Se}_{0.95}\text{Cl}_{0.05}$ sample. These four elemental maps jointly create the image in (f) showing elemental distribution. Sn precipitate is clearly seen. Scale bar: 10 μm 65

Figure 2. 5. Temperature dependence of (a) electrical conductivity, (b) Seebeck coefficient, (c) power factor, (d) total thermal conductivity, and (e) ZT for the melt-synthesized $\text{SnSe}_{1-y}\text{Cl}_y$ ($y = 0.02, 0.03, 0.05, \text{ and } 0.08$) samples measured parallel to the SPS direction. 70

Figure 2. 6. Temperature dependence of (a) electrical conductivity, (b) Seebeck coefficient, (c) power factor, (d) total thermal conductivity, and (e) ZT for the melt-synthesized $\text{Sn}_{1+z}\text{Se}_{0.95}\text{Cl}_{0.05}$ ($z = 0, 0.01, 0.02, 0.05, \text{ and } 0.10$) samples measured parallel to the SPS direction. 71

Figure 2. 7. Temperature dependence of (a) electrical conductivity, (b) Seebeck coefficient, and (c) power factor for the melt-synthesized $\text{Sn}_{1.05-x}\text{Pb}_x\text{Se}_{0.95}\text{Cl}_{0.05}$ samples measured parallel to the SPS direction. 72

Figure 2. 8. Temperature dependence of (a) total and (b) lattice thermal conductivity, and (c) thermoelectric figure of merit ZT for the melt-

synthesized $\text{Sn}_{1.05-x}\text{Pb}_x\text{Se}_{0.95}\text{Cl}_{0.05}$ samples measured parallel to the SPS direction.....73

Figure 2. 9. Temperature dependence of (a) electrical conductivity, (b) Seebeck coefficient, and (c) power factor for the melt-synthesized $\text{Sn}_{1.05-x}\text{Pb}_x\text{Se}_{0.95}\text{Cl}_{0.05}$ ($x = 0, 0.05, 0.10, 0.15,$ and 0.20) samples measured perpendicular to the SPS direction.74

Figure 2. 10. Temperature dependence of (a) total and (b) lattice thermal conductivity, and (c) ZT for the melt-synthesized $\text{Sn}_{1.05-x}\text{Pb}_x\text{Se}_{0.95}\text{Cl}_{0.05}$ ($x = 0, 0.05, 0.10, 0.15,$ and 0.20) samples measured perpendicular to the SPS direction.75

Figure 2. 11. Carrier concentration at room temperature as a function of the extent of (a) Cl doping (y) for $\text{SnSe}_{1-y}\text{Se}_y$ ($y = 0 - 0.08$) and (b) excess Sn (z) for $\text{Sn}_{1+z}\text{Se}_{0.95}\text{Cl}_{0.05}$ ($z = 0 - 0.10$).....76

Figure 2. 12. Experimental Seebeck coefficient (S) as a function of carrier concentration (n_H) with the theoretical Pisarenko line based on a single parabolic band model at room temperature. The experimental S of the MS and BA samples falls well on the Pisarenko line, indicating electronic structure of SnSe is not changed by PbSe alloying, Cl doping, and ball-mill and annealing process.78

Figure 2. 13. XRD patterns of the melt-synthesized (MS) and further ball-milled and annealed (BA) powder samples of $\text{Sn}_{0.90}\text{Pb}_{0.15}\text{Se}_{0.95}\text{Cl}_{0.05}$ in

comparison with the simulated patterns of SnSe (PDF 48-1224) and Sn (PDF 86-2264). Sn Bragg peaks are denoted by asterisks. 85

Figure 2. 14. XRD patterns of the SPS processed BA and the MS samples with the composition $\text{Sn}_{0.90}\text{Pb}_{0.15}\text{Se}_{0.95}\text{Cl}_{0.05}$ measured perpendicular (\perp) and parallel (\parallel) to the press direction in comparison with the theoretically simulated patterns of SnSe (PDF 48-1224) and Sn (PDF 86-2264). Major Bragg peaks are indexed..... 86

Figure 2. 15. (a) SEM image and (b–e) respective elemental maps of Sn, Pb, Se, and Cl atoms displayed in green, cyan, red, and orange color by EDS for the BA $\text{Sn}_{0.90}\text{Pb}_{0.15}\text{Se}_{0.95}\text{Cl}_{0.05}$ sample. These four panels jointly create the image in (f) showing elemental distribution. Scale bar: 50 μm 87

Figure 2. 16. Temperature dependence of (a) electrical conductivity, (b) Seebeck coefficient, and (c) power factor for the BA and MS $\text{Sn}_{0.90}\text{Pb}_{0.15}\text{Se}_{0.95}\text{Cl}_{0.05}$ samples measured perpendicular (\perp) and parallel (\parallel) to the press direction of SPS. Note that the BA sample exhibits a comparable ZT along both the directions..... 88

Figure 2. 17. Temperature dependence of (a) total thermal conductivity, (b) lattice thermal conductivity, and (c) ZT for the BA and MS $\text{Sn}_{0.90}\text{Pb}_{0.15}\text{Se}_{0.95}\text{Cl}_{0.05}$ samples measured perpendicular (\perp) and parallel (\parallel) to the press direction of SPS. Note that the BA sample exhibits a comparable ZT along both the directions..... 89

Figure 2. 18. Hall effect measurements for (a) Carrier concentration (n_H) and (b) mobility (μ_H) of the MS and BA samples with the composition $\text{Sn}_{0.90}\text{Pb}_{0.15}\text{Se}_{0.95}\text{Cl}_{0.05}$ perpendicular to the SPS press direction as a function of temperature.....91

Figure 2. 19. Temperature-dependent (a) electrical conductivity, (b) Seebeck coefficient, (c) total thermal conductivity, and (d) ZT for the BA $\text{Sn}_{0.90}\text{Pb}_{0.15}\text{Se}_{0.95}\text{Cl}_{0.05}$ samples. Three samples were independently prepared and characterized. These results indicate the excellent reproducibility of thermoelectric properties of BA samples.92

Figure 2. 20. Temperature-dependent (a) electrical conductivity, (b) Seebeck coefficient, (c) thermal conductivity and (d) ZT for the BA $\text{Sn}_{0.90}\text{Pb}_{0.15}\text{Se}_{0.95}\text{Cl}_{0.05}$ sample during multiple heating cycles, demonstrating the high repeatability of TE properties as well as the thermal and chemical stability of this material.....93

Figure 2. 21. (a) Differential thermal analysis (DTA) diagram of the BA $\text{Sn}_{0.90}\text{Pb}_{0.15}\text{Se}_{0.95}\text{Cl}_{0.05}$ sample at a rate of 10 K min^{-1} . Exo- and endothermic peaks (Δ) can be assigned to melting and recrystallization of Sn considering the melting point of Sn at $\sim 505 \text{ K}$.⁽¹⁾ The region for such thermal events is enlarged in the inset. (b) X-ray powder diffraction patterns for the $\text{Sn}_{0.90}\text{Pb}_{0.15}\text{Se}_{0.95}\text{Cl}_{0.05}$ BM sample before and after the DTA cycle. No discernible change is observed after DTA. The Bragg peaks from elemental Sn are indicated by the asterisk mark (*), which is due to excess Sn in the composition. The theoretically simulated patterns of SnSe (PDF 48-1224) and elemental Sn (PDF 86-2264) are given for comparison. Major peaks are

indexed. 94

Figure 2. 22. Typical cross-sectional STEM images of $\text{Sn}_{0.90}\text{Pb}_{0.15}\text{Se}_{0.95}\text{Cl}_{0.05}$. (a) Low magnification annular bright field (ABF) and (b) medium-magnification high-angle annular dark-field (HAADF) STEM images. Inset in (b) shows the fast Fourier transform (FFT) image along the [201] axis. (c) Inverse FFT (IFFT) image taken at the red rectangle in (b). Red symbols indicate edge dislocations. 101

Figure 2. 23. Typical cross-sectional low magnification annular bright-field (ABF) scanning transmission electron microscope (STEM) images of the SPS-processed MS sample with the composition $\text{Sn}_{0.90}\text{Pb}_{0.15}\text{Se}_{0.95}\text{Cl}_{0.05}$ showing a substantial degree of moiré structures and edge dislocations 102

Figure 2. 24. Elemental maps scanned on the region with moiré structures by STEM-EDS. EDS signals for (a) Sn, (b) Pb, (c) Se, and (d) Cl atoms are depicted in cyan, magenta, red, and green color, respectively. These four panels jointly create the image in (e). Scale bar: 50 nm. 103

Figure 2. 25. (a) Typical medium-magnification ABF-STEM images of the MS sample of $\text{Sn}_{0.90}\text{Pb}_{0.15}\text{Se}_{0.95}\text{Cl}_{0.05}$. Inset: fast Fourier transform (FFT) image along the [201] axis. (b-d) are inverse FFT images for the red rectangles of 1, 2, and 3 in (a), respectively. Red symbols indicate edge dislocations. Average density of dislocations is given with standard deviation. 104

Figure 2. 26. (a) Representative HAADF-STEM image of $\text{Sn}_{0.90}\text{Pb}_{0.15}\text{Se}_{0.95}\text{Cl}_{0.05}$ viewed down the [201] direction. Dotted lines outline the regions with a discernible contrast. Inset: the magnified atomic-resolution HAADF-STEM image showing the SnSe structure at the atomic scale. (b) IFFT image of (a). Red symbols indicate edge dislocations. (c) and (d) are lattice strain maps of the HAADF-STEM image in (a) demonstrating strain distributions around dislocations. The color bar displays the lattice strains from +30 to -30%. 105

Figure 2. 27. (a) Representative high angle annular dark-field (HAADF) STEM image of $\text{Sn}_{0.90}\text{Pb}_{0.15}\text{Se}_{0.95}\text{Cl}_{0.05}$ viewed down the [123] direction. Irregular atomic arrangements are observed in the red rectangle. (b) IFFT image of (a). Red symbols indicate edge dislocations. Inset: fast Fourier transform (FFT) image along the [123] axis. (c) and (d) are lattice strain maps of HAADF-STEM image in (a) showing severe strain distributions around dislocations. The color bar indicates the lattice strain ranging from +30 to -30%. 106

Figure 2. 28. (a) Magnified atomic-resolution HAADF-STEM image taken through the [123] zone axis. Atomic-resolution elemental mapping of (b) Sn, (c) Pb, (d) Se, and (e) Cl atoms depicted in green, cyan, red, and orange color, respectively, by STEM-EDS scanned on the red rectangle in (a). These four panels jointly create the image in (f), demonstrating direct observation of the crystal structure of $\text{Sn}_{0.90}\text{Pb}_{0.15}\text{Se}_{0.95}\text{Cl}_{0.05}$ at the atomic level and verifying the arrangement of constituent atoms. Scale bar: 0.5 nm. 107

Figure 2. 29. Comparison of experimental (circles) and calculated κ_{lat} based on Umklapp, point defect, lattice strain, and dislocation scattering processes using a Callaway–Debye model (dotted line) for the MS sample of $\text{Sn}_{0.90}\text{Pb}_{0.15}\text{Se}_{0.95}\text{Cl}_{0.05}$ parallel to the press direction. The calculated κ_{lat} is further modified by the hypothesis that dislocation density can be linearly reduced above 550 K (solid line)..... 108

Figure 3. 1. (a) A photograph of the graphite mold after SPS for the $\text{Cu}_{0.06}\text{Bi}_2\text{Te}_{3.17}$ sample. Gray bubbles are seen, which were squeezed out of the pellet during SPS. (b) Powder XRD pattern for the ejected material in comparison with those of reference Bi_2Te_3 and Te. (The International Centre for Diffraction Data (ICDD) Bi_2Te_3 (PDF# 15-0863) and Te (PDF# 36-1452)). 137

Figure 3. 2. (a) Powder XRD data for the SPS $\text{Cu}_x\text{Bi}_2\text{Te}_{3.17}$ ($x = 0\text{--}0.06$) samples in comparison with the theoretical pattern for Bi_2Te_3 (JCPDS 15-0863). (b) The (006) reflection peak shifts downward with the higher Cu concentration. The refined lattice parameters with respect to the Cu content along (c) the c - and (d) the a -axes are given with the standard deviation. 141

Figure 3. 3. (a) Powder XRD patterns for control $\text{Cu}_x\text{Bi}_2\text{Te}_3$ ($x = 0.02$ and 0.04) samples before and after SPS process. The refined lattice parameters with respect to the Cu content for control SPS $\text{Cu}_x\text{Bi}_2\text{Te}_3$ samples along (b) the a - and (c) the c -axes..... 142

Figure 3. 4. (a) Powder XRD patterns and (b) magnified XRD patterns around $10 \sim 40^\circ$ for SPS $\text{Cu}_{0.06}\text{Bi}_2\text{Te}_{3.17}$ and control ingot $\text{Cu}_{0.06}\text{Bi}_2\text{Te}_{3.17}$ samples, which have the same nominal composition. The theoretically calculated patterns for Bi_2Te_3 , CuTe , and Te are given for comparison. (ICDD Bi_2Te_3 (PDF# 15-0863), CuTe (PDF# 01-070-8050), and Te (PDF# 36-1452)). The Bragg diffraction peaks for CuTe and Te are marked by asterisks and triangles, respectively. (c) Powder XRD patterns and (d) magnified XRD patterns around $10 \sim 40^\circ$ for $\text{Cu}_x\text{Bi}_2\text{Te}_{3.17}$ before SPS process..... 143

Figure 3. 5. Thermogravimetric analysis (TGA) data demonstrate the phase homogeneity and thermal stability of the SPS $\text{Cu}_{0.06}\text{Bi}_2\text{Te}_{3.17}$ sample. The control $\text{Cu}_{0.06}\text{Bi}_2\text{Te}_{3.17}$ ingot sample shows a weight loss around 680 K due to the evaporation of excess tellurium, as confirmed by the thermal behavior of elemental tellurium (melting point of $\text{Te} \sim 720 \text{ K}$)..... 144

Figure 3. 6. Typical SEM image of the SPS $\text{Cu}_{0.06}\text{Bi}_2\text{Te}_{3.17}$ sample showing the highly oriented lamellar morphology. Scale bar: 100 μm 147

Figure 3. 7. (a) Typical SEM image and (b–d) EDS elemental maps for (b) Cu , (c) Bi , and (d) Te atoms on the polished surface of the SPS $\text{Cu}_{0.06}\text{Bi}_2\text{Te}_{3.17}$ sample show the homogeneous distribution of the constituent elements without phase segregation. White scale bar corresponds to 50 μm 148

Figure 3. 8. (a) Typical SEM image of the control ingot $\text{Cu}_{0.06}\text{Bi}_2\text{Te}_{3.17}$ sample and EDS elemental maps (b-d) taken at the rectangular region in (a) reveal that the line features, consisting of Cu and Te and being absent of Bi atoms,

are embedded in the Bi_2Te_3 matrix. White scale bar corresponds to 50 μm .

..... 149

Figure 3. 9. Temperature dependence of (a) electrical conductivity, (b) Seebeck coefficient, (c) total thermal conductivity, and (d) thermoelectric figure of merit (ZT) for the control $\text{Cu}_{0.06}\text{Bi}_2\text{Te}_{3.17}$ ingot sample. Note that the control ingot sample shows p-type conduction. The corresponding data for pristine Bi_2Te_3 sample, which is similarly prepared to the other samples, are given for comparison. 156

Figure 3. 10. Charge transport properties for the SPS $\text{Cu}_x\text{Bi}_2\text{Te}_{3.17}$ samples measured perpendicular to the SPS press direction. (a) Temperature dependence of the Seebeck coefficient in comparison with that of the control SPS $\text{Cu}_x\text{Bi}_2\text{Te}_3$ samples. (b) The Pisarenko relation based on a single parabolic band (SPB) model at room temperature. The reported experimental data for Cu-doped Bi_2Te_3 -based materials are given for comparison.^{41, 47} (c) Hall-effect charge-carrier concentration and (d) Hall mobility with respect to the Cu concentration at room temperature. Note that the nominal composition of samples are given in the panels..... 157

Figure 3. 11. (a) The Hall carrier concentration (n_H) and (b) the Hall mobility (μ_H) at room temperature for control SPS $\text{Cu}_x\text{Bi}_2\text{Te}_3$ samples measured perpendicular to the press direction..... 158

Figure 3. 12. Calculated μ_H with respect to n_H (solid lines) assuming acoustic phonon scattering. Experimental values for SPS $\text{Cu}_x\text{Bi}_2\text{Te}_{3.17}$ samples at room temperature are much higher than the theoretical prediction and increase with

the higher concentration of Cu. Experimental data for single-crystal Bi_2Te_3 ,⁵² polycrystalline $\text{Cu}_{0.07}\text{Bi}_2\text{Te}_3$,⁴⁷ and polycrystalline $\text{Cu}_{0.01}\text{Bi}_2\text{Te}_{2.7}\text{Se}_{0.3}$ ⁴¹ from previous reports are also given for comparison..... 159

Figure 3. 13. Temperature-dependence of (a) n_H and (b) μ_H for the SPS $\text{Cu}_{0.06}\text{Bi}_2\text{Te}_{3.17}$ sample. (c) A $\log(\mu_H)$ – $\log(T)$ plot shows different slopes with respect to temperature..... 160

Figure 3. 14. The temperature-dependent Hall coefficient (R_H) for the SPS $\text{Cu}_{0.06}\text{Bi}_2\text{Te}_{3.17}$ sample. The R_H gradually decreases with increasing temperature..... 161

Figure 3. 15. Temperature dependence of (a) electrical conductivity and (b) power factor for the SPS $\text{Cu}_x\text{Bi}_2\text{Te}_{3.17}$ samples measured perpendicular to the SPS press direction. (c) Comparison of the power factor achieved in this work with those of the previous reports on Cu-doped Bi_2Te_3 -based compounds.^{41, 47} 162

Figure 3. 16. (a) Powder XRD patterns for the SPS $\text{Cu}_x\text{Bi}_2\text{Te}_3$ ($x = 0.06, 0.08$ and 0.10) samples. Temperature dependence of (b) electrical conductivity, (c) Seebeck coefficient, and (d) power factor for the SPS $\text{Cu}_x\text{Bi}_2\text{Te}_{3.17}$ samples measured perpendicular to the SPS press direction..... 163

Figure 3. 17. The relative electrical resistance with respect to time for the SPS $\text{Cu}_{0.06}\text{Bi}_2\text{Te}_{3.17}$ sample under the current density of 12 A cm^{-2} at room temperature, demonstrating the high stability of this material under a large

current flow..... 164

Figure 3. 18. Temperature dependence of (a) total, (b) electrical, and (c) lattice thermal conductivity. (d) Figure of merit ZT for the SPS $\text{Cu}_x\text{Bi}_2\text{Te}_3$ and control SPS $\text{Cu}_x\text{Bi}_2\text{Te}_3$ samples, measured perpendicular to the SPS press direction..... 169

Figure 3. 19. (a, b) Typical low-magnification TEM images of SPS $\text{Cu}_{0.06}\text{Bi}_2\text{Te}_{3.17}$ specimen showing dislocations with a density of $\sim 2 \times 10^{12} \text{ cm}^{-2}$ embedded in the matrix. Inset of (b) shows the selected area electron diffraction pattern along the [001] zone axis, which is taken on the entire area of (b) that includes both the matrix and dislocations. (c) High-resolution TEM image taken on dislocations. (d) The corresponding inverse fast Fourier transform (IFFT) image indicates the presence of edge dislocations, indicated by red symbols..... 170

Figure 3. 20. (a) The calculated temperature-dependent bipolar (κ_{bip}) and lattice thermal conductivity (κ_{lat}). (b) The Comparison of experimental (triangles) and calculated κ_{lat} considering Umklapp (U), grain boundary (B), point defect (PD), and dislocation (DS) scattering processes using a Callaway-Debye model (solid line) for the SPS $\text{Cu}_{0.06}\text{Bi}_2\text{Te}_{3.17}$ sample. 171

Figure 4. 1. (a) Electrical conductivity (σ), (b) Seebeck coefficient (S), (c) power factor (σS^2), and (d) total thermal conductivity (κ_{tot}) for the n-type $(\text{Mm,Sm})_y\text{Co}_4\text{Sb}_{12}$ and p-type $\text{DD}_y\text{Fe}_3\text{CoSb}_{12}$ as a function of temperature. 196

Figure 4. 2. Thermoelectric figure of merit for n-type $(Mm,Sm)_yCo_4Sb_{12}$ and p-type $DD_yFe_3CoSb_{12}$ as a function of temperature. 197

Figure 4. 3. (a) A schematic illustration of a TE module showing consecutive layers of a TE leg, metallization layer, brazing filler and metallic electrode on a ceramic substrate and (b) potential interfacial diffusion and intermetallic layer growth occurring at the metallization interface. 200

Figure 4. 4. SEM images, SEM-EDS line scan profiles, and electrical resistivity profiles taken on the interface between the Fe-Ni metallization layer and n- (left) and p-type (right) SKD legs, respectively, before (a-d) and after (e-h) heat treatment at 773 K for 10 h in a vacuum. 201

Figure 4. 5. HAADF-STEM images and STEM-EDS results at the interface of the p-type (a and c) and n-type (b and d) Fe-Ni/SKD interfaces and SAED patterns characterized by the $[uvw]$ indices on the corresponding regions (e-j) shown in the HAADF-STEM images..... 208

Figure 4. 6. Indexing of the selected area electron diffraction (SAED) patterns the interface of the Fe-Ni metallized p-type and n-type skutterudite/Fe-Ni: (a) indexing for zone axis $[\bar{1} 0 0]$ of the diffraction pattern of Region B in Figure 4. 5; (b) indexing for zone axis $[\bar{1} 1 1]$ of the diffraction pattern of Region C in Figure 4.5; (c) indexing for zone axis $[\bar{1} 1 1]$ of the diffraction pattern of Region D in Figure 4.5; (d) indexing for zone axis $[\bar{2} 2 0]$ of the diffraction pattern of Region F in Figure 4.5; (e) indexing for zone axis $[0 0 1]$ of the diffraction pattern of Region H in Figure 4.5; (f) indexing

for zone axis [0 1 0] of the diffraction pattern of Region I in Figure 4. 5.....
.....209

Figure 4. 7. (a) A photograph of the Fe-Ni metallized-SKD TE module and
(b) its output power characteristics at various hot side temperature (T_h).....
.....212

Figure 4. 8. Comparison of output power density for representative TE
modules with their device internal resistance. The internal resistance is
normalized to one thermocouple resistance.....213

Chapter 1. Introduction: High performance bulk thermoelectric materials and Dissertation Overview

1.1 Introduction of Thermoelectrics

The global population growth and economic development require the 50% increased use of fossil fuels by 2040, which are being depleted rapidly.^[1] Their consumption is inevitably accompanied by a large amount of CO₂ emission, causing serious environmental problems. In addition, they are main sources for generating electric energy, more than a half of which is lost as waste heat upon consumption.^[2] Therefore, the need for sustainable energy sources to replace the fossil fuels has become the one of the most critical issues. Thermoelectric (TE) technology is a promising candidate to address these multiple issues because it can convert heat into electrical energy directly without releasing undesirable gaseous residues. TE devices also operate with no noise and vibration, giving high mechanical reliability. The performance of TE materials is typically expressed by a dimensionless figure of merit $ZT = \sigma S^2 T / \kappa_{\text{tot}}$, where σ is the electrical conductivity, S is the Seebeck coefficient, the product σS^2 is the power factor (PF), κ_{tot} is the total thermal conductivity, and T is absolute temperature.^[3] The κ_{tot} comprises electrical (κ_{ele}), lattice (κ_{lat}), and bipolar thermal conductivities (κ_{bip}).^[4]

Before investigating the strategies to increase thermoelectric performances, we discuss the fundamental thermoelectric phenomena. Historically, Thomas Johann Seebeck reported an interesting experimental result that a needle of compass was deflected by a circuit made from two dissimilar metals with a temperature difference between junctions, called as the Seebeck effect (Figure 1. 1a). The temperature difference drives charge carriers (electrons and/or holes) in the metals to move from hot to cold side, which induces electrical current through the circuit.^[5] The power generation efficiency as a function of average ZT_{ave} is presented in figure 1.1, and the relationship can be expressed by,^[6, 7]

$$\eta_p = \frac{T_h - T_c}{T_h} \left[\frac{\sqrt{1 + ZT_{ave}} - 1}{\sqrt{1 + ZT_{ave}} + T_c/T_h} \right]$$

where ZT_{ave} is the average value of both p-type and n-type materials, T_h and T_c are the temperature at the hot and cold sides, respectively, and the ZT_{ave} per leg is averaged over the temperature between T_h and T_c .

$$ZT_{ave} = \frac{1}{T_h - T_c} \int_{T_c}^{T_h} ZT dT$$

The figure 1. 1b shows that the higher conversion efficiency can be obtained by a higher ZT_{ave} and/or a larger temperature difference. For example, if the ZT_{ave} is 3.0 and the temperature difference is 400 K, the efficiency of power generation can reach 25%, which is comparable to that of the traditional heat

engines.

In contrast to the Seebeck effect, heating or cooling at an electrified junction of two different metals is observed, which is called as the Peltier effect (figure 1. 1c). Figure 1. 1c shows that when a current flows the circuit, heat can be absorbed at the upper junction and release at the lower junction, which means upper end is active cooling. The efficiency of thermoelectric cooling hc is given by,

$$n_c = \frac{T_h}{T_h - T_c} \left[\frac{\sqrt{1 + ZT_{ave}} - T_c/T_h}{\sqrt{1 + ZT_{ave}} + 1} \right]$$

Similar to the thermoelectric power generation, a larger efficiency of thermoelectric cooling can be obtained by a higher ZT_{ave} . For instance, when ZT_{ave} is 3.0 and temperature difference is 20 K, hc reaches 6%. The Peltier effect is the model of the thermoelectric cooling, which have already been used in some electronic devices for military use. Thermoelectric coolers can also be used to refrigeration devices to keep temperatures and to maintain stable functioning.

As shown in Figure 1. 2, a typical thermoelectric module consists of a number of alternating rectangular legs of n- and p-type thermoelectric materials, generally semiconductor. The thermoelectric devices allow electrical current and heat to flow through each leg in parallel. A thermoelectric device can be used for both power generation and cooling

because the relation between Peltier effect and Seebeck effect is thermodynamically reversible. To generate more energy, the both type thermoelectric materials with high performance are required. It should be noted that the thermoelectric legs should be coupled to metallic electrodes with minimal contact resistance and energy loss at the interface. In addition, chemical reactions and interdiffusion occurring at that interface can also reduce the performances of devices. However, the problems discussed above have been relatively less studied.

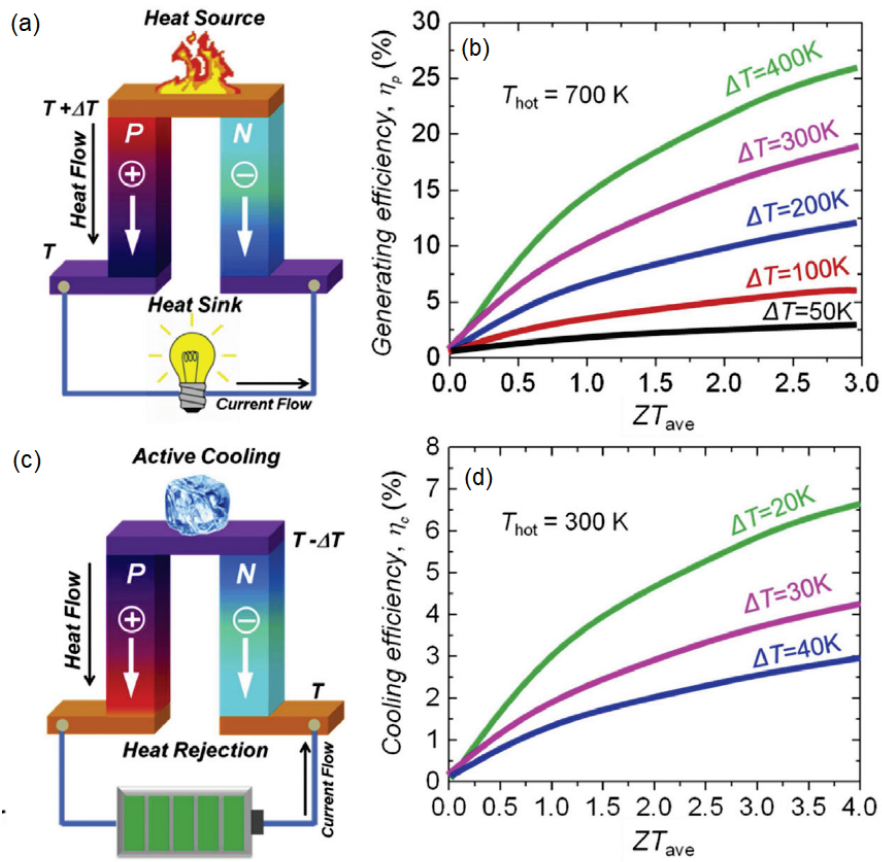


Figure 1. Schematic illustrations of thermoelectric modules Seebeck effect for power generation and Peltier effect for active refrigeration. (a) Seebeck effect for the power generation, (b) power generation efficiency as a function of average ZT_{ave} , (c) Peltier effect for the active refrigeration, (d) cooling efficiency as a function of average ZT_{ave} . (from Ref [4] Zhang X.; Zhao, L. J. *Materiomics* **2015**, 1, 92e105)

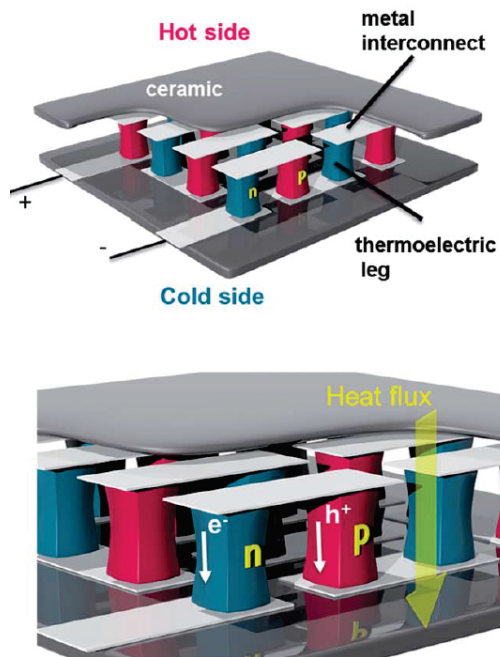


Figure 1. 2. Schematic illustration for typical thermoelectric module composed of p-type and n-type legs. (from Ref. [8], Bubnova, O.; Crispin, X. *Energy Environ. Sci.*, **2012**, 5, 9345)

1.2 General background

For a good thermoelectric material, a large Seebeck coefficient (S) that is usually present in semiconductors, high electrical conductivity (σ) just like metals, and poor thermal conductivity (κ) as in glasses are required. A combination of these features in a single material enables to realize high thermoelectric performance. However, it should be noted that the combination is almost impossible due to the close correlation of the parameters with each other. The Wiedemann–Franz relation shows that total thermal conductivity (κ_{tot}) is composed of both phonon and electronic part. It means that thermal conductivity is proportional to electrical conductivity (σ). In addition, the Pisarenko relation limits the simultaneous both large S and σ . The complex relationships of these thermoelectric parameters is defined by:^{[9-}

18]

$$S = \frac{8\pi^2 k_B^2}{3eh^2} m^* \left(\frac{\pi}{3n}\right)^{2/3}$$

$$\sigma = n e \mu = \frac{n \tau e^2}{m^*}$$

$$\kappa_{tot} = \kappa_{lat} + \kappa_{ele} = \kappa_{lat} + L \sigma T$$

where k_B is the Boltzmann constant, m^* is the density of states effective mass, h is the Planck constant, n is the carrier concentration, e is per electron charge, μ is the carrier mobility, τ is the relaxation time, κ_{tot} is the total thermal

conductivity, κ_{lat} is the lattice thermal conductivity, κ_{ele} is the electronic thermal conductivity, and L is the Lorenz number.

For instance, the approach of tuning carrier concentration alone is difficult to enhance ZT . Figure 1. 2 shows the compromise between thermopower and electrical conductivity in thermoelectric materials, which means that there is struck to maximize the ZT . The maximum ZT is typically obtained at carrier concentrations between 10^{19} and 10^{21} cm^{-3} , which is depending on each material systems.

Since the historic discoveries of thermoelectric effect in the 19th century, a number of materials have been explored and used to generate thermoelectricity, including metals,^[19-22] ceramics,^[23-25] and semiconductors.^[26-28] It should be noted that because almost all these materials were initially obtained through countless attempts, the thermoelectric community had grown very slowly in in the beginning until the 1950s. Since the basic science of thermoelectric effects was established, the field of thermoelectrics is rapidly advanced, especially in the past two decades. Figure 1. 3 shows the ZT values of developed bulk materials over the last two decades as a function of both year and temperature. Especially since the 2010, the great developments have been achieved in thermoelectric materials with the greatest ZT s above 2.^[12, 29-30] Traditional thermoelectric materials, namely, bismuth telluride and lead chalcogenides are intensively

studied in their respective working temperature region. On the other hand, because of the abundance of Te and the toxicity of Pb in lead chalcogenides, many researchers explore the materials of Te- and Pb-free compounds, among which tin chalcogenides,^[31] and skutterudites^[32] appear as most promising. Particularly, a simple binary compound of single crystalline SnSe presents an excitingly high ZT of ~ 2.6 at 923 K along the crystallographic *b*-axis.^[31] This can be achieved because of the giant anharmonic and anisotropic chemical bonding in SnSe, which makes an extremely low thermal conductivity

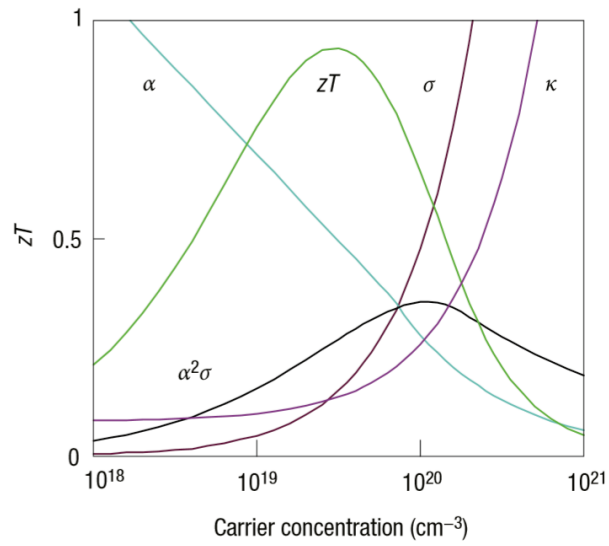


Figure 1. 3. Optimizing ZT through tuning the carrier concentration. Good thermoelectric materials are typically heavily doped semiconductors with a carrier concentration between 10^{19} and 10^{21} cm^{-3} . (from Ref. [18], Snyder J.; Toberer E. *Nat. Mater.* **2008**, 7, 105e14.)

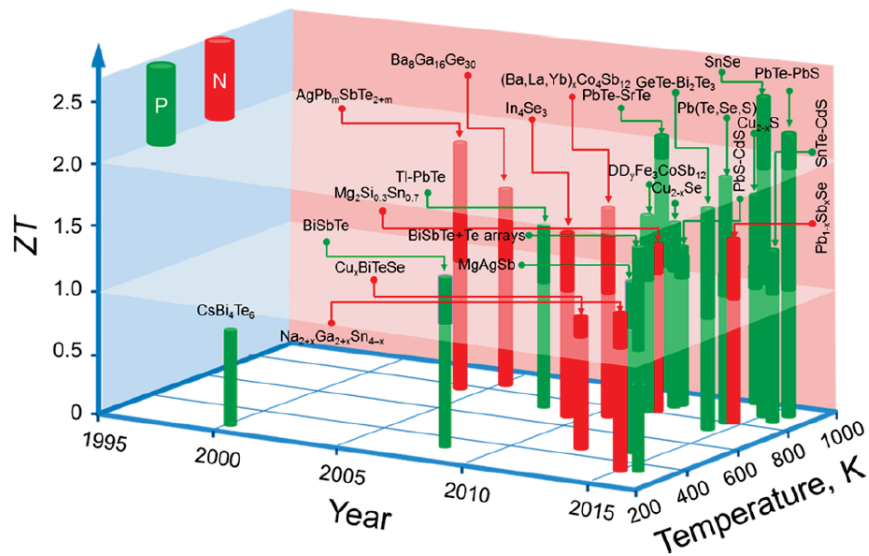


Figure 1. 4. State-of-the-art bulk thermoelectric materials. The thermoelectric figure-of-merit ZT as a function of temperature and year. (from Ref. [9], Tan, G.; Zhao, L. D.; Kanatzidis, M. G. *Chem. Rev.* **2016**, 116, 12123).

1.3 Advanced approaches for thermoelectric materials

There are two possible approaches to increase ZT : either the power factor is enhanced and/or the thermal conductivity is minimized. As mentioned above, optimizing each parameter solely is very difficult because the properties are interdependent. However, in the last two decades, ZT has been greatly enhanced mainly due to many innovative strategies to reduce κ_{lat} . For instance, solid-solution alloying, doping, nanostructuring, all-scale hierarchical architectures, and the development of new materials with intrinsically low thermal conductivity are reported as effective strategies to reduce thermal conductivity. Further, the power factor can be enhanced by band engineering.

1.3.1 Doping and Alloying

The interaction between atoms in solids leading displacements from their ideal positions creates oscillating waves with various wavelength, which is known as phonons. The phonons carry heat through the lattice vibration and contributes to the lattice thermal conductivity (κ_{lat}). The phonon waves can be scattered at crystal imperfectness (e.g., point defects, dislocations, interfaces, precipitates, etc.), which can act as thermal resistance and reduces the κ_{lat} .

It is well established to introduce of crystal imperfection into the host matrix by doping and/or alloying, which is a commonly used strategy to decrease the κ_{lat} . According to theoretical model on thermal conductivity developed by Callaway^[33, 34], mass contrast and strain field fluctuations generated by lattice imperfection results in the reduction of thermal conductivity. Therefore, to reduce the κ_{lat} , high doping amount, a large mass fluctuation between the host and impurity leading disorder in the lattice, and/or a significant lattice mismatch are required.

Figure 1. 5 display typical doping approaches commonly used. In the single doping case, the dopant can generate lattice disorder and optimize the carrier concentration by aliovalent doping (Figure 1. 5a). However, aliovalent doping is nearly impossible to introduce high amount dopants because of charge imbalance, which inhibits the further reduction of κ_{lat} . To compensate for this drawback, cross substitution is devised that host element is exchange with pairs from other groups but the total valence of charge keeps constant (Figure 1. 5b). The best example is LAST system that the divalent Pb is substituted by both monovalent Ag and trivalent Sb.^[35] Note that the substitution not only prevent the phonon transport but could change electronic band structure,^[36, 37] optimizing the other parameters to enhance the thermoelectric performances.

Third, the maximum mass contrast could be achieved when the dopant atom is a disordered vacancy (Figure 1. 5c). For example, the unexpectedly low lattice thermal conductivity for partially filled skutterudites $F_y\text{Co}_4\text{Sb}_{12}$ was reported. In the compounds, each F and y means filler atom and filling fraction, respectively. The strong phonon scattering between F and the structural vacancy rationally explains the unexpected low thermal conductivity.^[38]

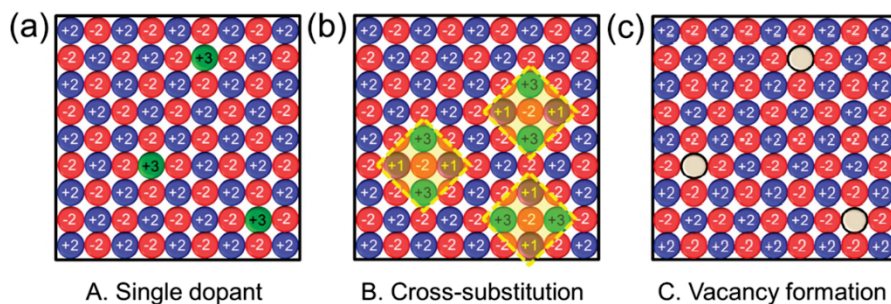


Figure 1. 5. Schematic representation of various types of point defects: (a) single doping, (b) cross-substitution, and (c) lattice vacancy formation. (from Ref. [9], Tan, G.; Zhao, L. D.; Kanatzidis, M. G. *Chem. Rev.* **2016**, 116, 12123).

1.3.2 Nanostructuring

Before discussing the nanostructuring, it is better to define the term. There are two types of nanostructured thermoelectric materials. First, the material consists of a single phase synthesized with nanosized particles or grains, which is defined type-I. The second kind is a system comprising a major bulk phase (matrix) containing a minor second phase embedded in the matrix, typically via precipitation from solid solution (type-II). The following discussion focuses on the type-II systems.

It is demonstrated that a substantial reduction in lattice thermal conductivity is the principal contributor to the enhanced ZT of bulk nanostructured materials. The reduction in lattice thermal conductivity arises from enhanced scattering of heat carrying phonons by interfaces and related effects of nanostructures in such a nanoscale system.

The first experimental observation of high thermoelectric performance resulted from nanostructuring is the LAST ($\text{AgPb}_m\text{SbTe}_{2+m}$) confirmed by transmission electron microscopy (TEM).^[35] The very low lattice thermal conductivity of the LAST system was attributed to the spontaneous and ubiquitous nanoscale precipitations of second phases in the PbTe matrix (Figure 1. 6).

After this first observation, introducing the nanostructure in matrix is commonly used such as the systems of LASTT ($\text{Ag}(\text{Pb}_{1-x}\text{Sn}_x)_m\text{SbTe}_{2+m}$) and

SALT ($\text{NaPb}_m\text{SbTe}_{2+m}$). Generally, the nanocrystals are endotaxially embedded in the matrix, with a good lattice match on all surrounding surfaces. This endotaxy is an important and favorable feature for facile carrier transport throughout the sample. A number of interfaces between nanocrystal and matrix provides for an effective barrier to heat carrying phonon transport in the bulk sample. The nanostructures scatter more phonons of appropriate wavelengths than solid solution alloying alone. Introducing PbS into PbTe is a representative another example that the lattice thermal conductivity can be greatly reduced by nanostructure in the matrix (Figure 1. 7).^[39] The HRTEM image indicates that 16% PbS-PbTe sample shows many strips with < 10 nm sized particles in the matrix. This phase separation is responsible for the very low lattice thermal conductivity, thereby leading to enhance the ZT.

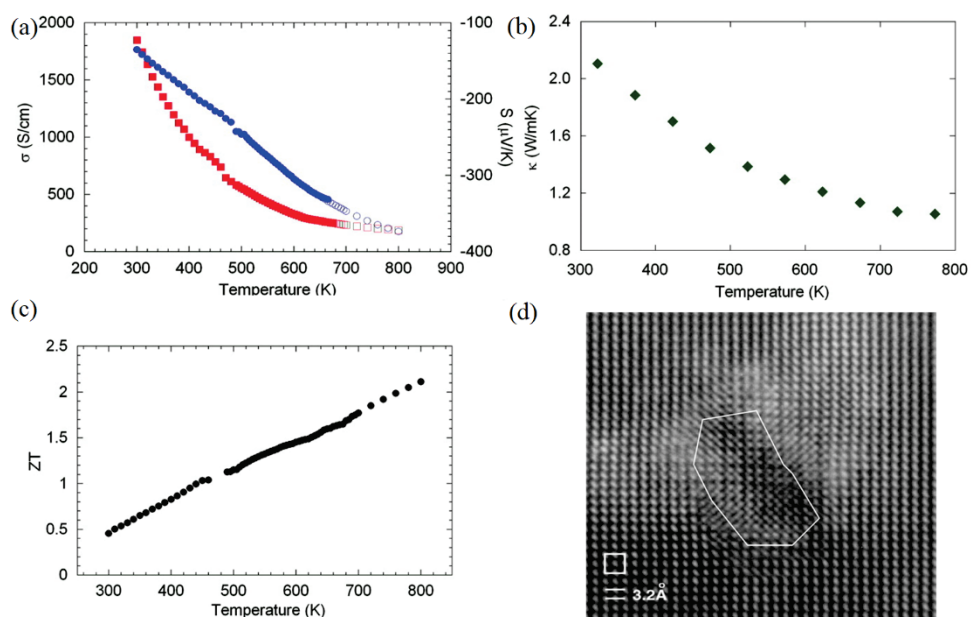


Figure 1. 6. Temperature-dependent (a) charge, (b) thermal transport, and (c) ZT for AgPb₁₈SbTe₂₀. (d) High resolution TEM image of AgPb₁₈SbTe₂₀ sample shows “nanodot”. (from Ref. [35], Hsu, K. F.; Loo, S.; Guo, F.; Chen, W.; Dyck, J. S.; Uher, C.; Hogan, T.; Polychroniadis, E. K.; Kanatzidis, M. G. *Science* **2004**, 303, 818).

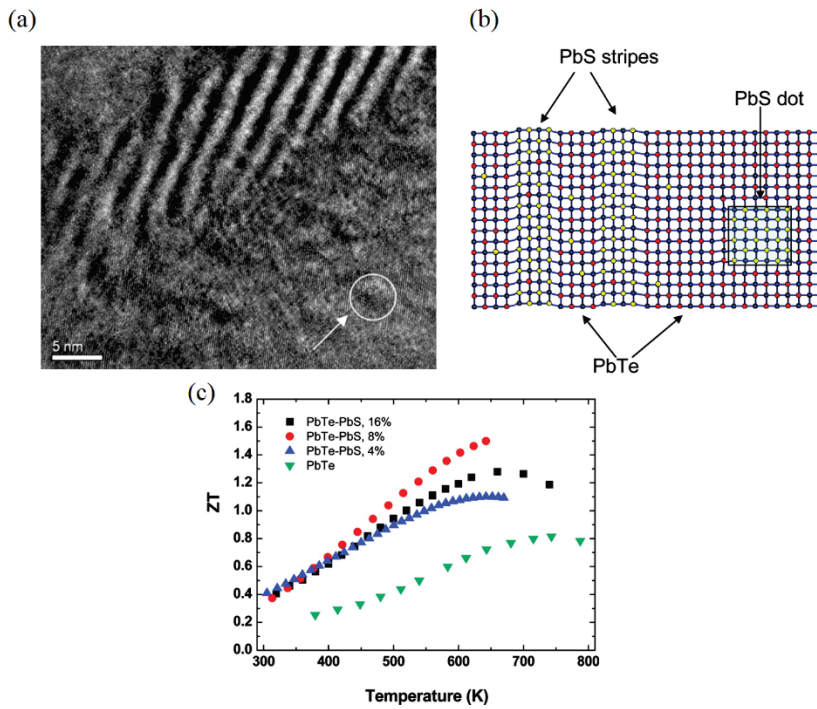


Figure 1. 7. (a) HRTEM image for PbTe-PbS mixed matrix. (b) Schematic illustration for structure of the mixture that shows PbS stripes and dots. (c) Temperature dependent ZT for PbTe-PbS system. (from Ref. [39], Androulakis, J.; Lin, C.; Kong, H.; Uher, C.; Wu, C.; Hogan, T.; Cook, B. A.; Caillat, T.; Paraskevopoulos, K. M.; Kanatzidis, M. G. *J. Am. Chem. Soc.* **2007**, 129, 9780).

1.3.3 All-scale hierarchical architecturing

When a single thermoelectric material includes all points defects, nanostructures, and mesoscale structures, we call this as an all-scale hierarchical architecture. If the thermal conductivity in materials is limited by the Umklapp scattering, acoustic phonons in a material carry most of the heat and they have a spectrum of wavelengths and mean free paths (MFP), which contributes to the total thermal conductivity.

Introduction of impurities on matrix can be effective way to mainly scatter phonons with short wavelength due to either mass contrast or local strain induced by the defects. The scattering of medium MFP phonons is best achieved through nanostructuring. Such scattering is believed to be occurring at the interfaces between the precipitates and the matrix and from the mass contrast between the two phases. While the point defects and nanostructures can strongly scatter the phonon with short and medium wavelengths, long wave length phonons are scarcely affected and still able to transport heat. To scatter the phonons with long MFP, additional mechanisms are required.

To scatter these phonons as well, crystal defects and structure features at the length scale of micrometers or submicrometers is required, which is called as mesoscale. Generally, while the ingot and single crystals have larger grains than 10 μm , polycrystalline sample has smaller grain that has mesoscale (Figure 1. 8).^[9] It can be introduced into materials through careful powder

processing. For instance, mesoscale grains in polycrystalline bulk thermoelectric materials are produced by grinding the material into mesoscopic particles, followed by densifying by either hot pressing or spark plasma sintering. Then, the grain boundary scattering can occur at the inter-grain region. The propagation of phonons with long MFP can be limited by the finite size in a given grain. Thus, meso-scale grain boundaries mostly scatter the long wavelength phonons.

To scatter phonons with entire MFP ranges from nano- to micro-length scales, all-scale hierarchical architectures are required. This means that point defects, nanostructures, and grain boundary interfaces must all be integrated in a single sample, as shown in Figure 1. 9.^[9] All-scale hierarchical architectures have the potential to significantly reduce the thermal conductivity down to the minimum theoretical limit.^[40-43]

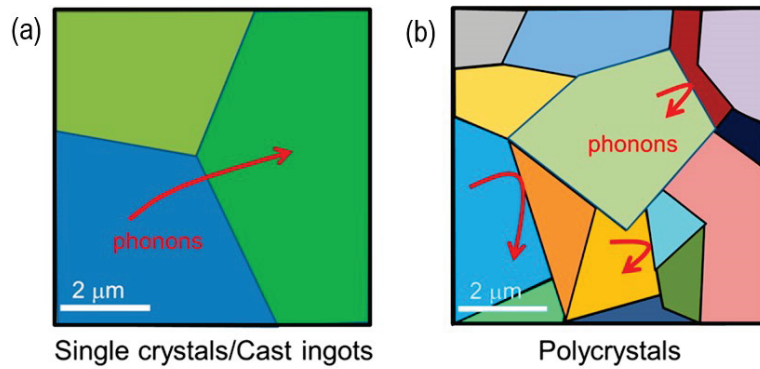


Figure 1. 8. Schematic illustrations of microstructures for (a) single crystals/ingots and (b) polycrystalline samples with mesoscale grains. The grain size of polycrystalline sample is much lower than those of single crystals/cast ingots. (from Ref. [9], Tan, G.; Zhao, L. D.; Kanatzidis, M. G. *Chem. Rev.* **2016**, 116, 12123).

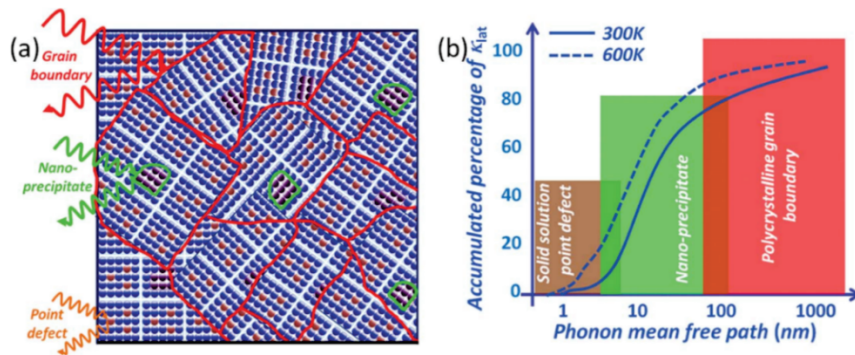


Figure 1. 9. All-scale hierarchical architectures and lattice thermal conductivity: (a) all-scale hierarchical architectures, and (b) cumulatedistribution function of lattice thermal conductivity with respect to the phonon mean free path in Si or PbTe bulk. (from Ref. [10], Zhao, L. D.; Dravid, V.; Kanatzidis, M. G. *Energy Environ. Sci.*, **2014**, 7, 251-268)

1.3.4 Discoveries of promising materials with intrinsically low thermal conductivity

Up to this point, I introduce the diverse approaches to reduce the lattice thermal conductivity maintaining power factor, including doping & alloying, nanostructuring, and all-scale hierarchical architecturing. Recently, as a new alternative, exploring new thermoelectric materials has been in the spotlight.^[31] In particular, there are special pristine compounds with high thermoelectric performances, results from their intrinsically low lattice thermal conductivity. It means that the complex approaches are not required because of the intrinsic low thermal conductivity. I will introduce the example for promising compounds with intrinsically ultralow thermal conductivity, which arise from an anharmonic and anisotropic characters.

The simple binary compound of SnSe is a semiconductor with a band gap of 0.86 eV. It presents a p-type conduction with a relatively low hole concentration and electrical conductivity. Because of poor charge transport properties, it has been historically neglected for thermoelectrics but used for other applications such as optoelectronics, solar cells, and other electronic devices. Recently, SnSe has been reported as a promising thermoelectric material, showing the lowest lattice thermal conductivities ($\sim 0.23 \text{ W m}^{-1} \text{ K}^{-1}$ at 923 K) and even without doping, thereby achieving the highest ZT of 2.6 at 973 K.^[31] The extraordinary properties are originated from its anharmonic

and anisotropic nature.

SnSe adopts an unusual layered orthorhombic structure at room temperature, which is derived from 3 three dimensional distortion of rock-salt structure like NaCl (Figure 1. 10a). SnSe includes two-atom-thick slabs (in the bc plane) with strong Sn-Se bonding along in-plane, which are connected with weaker Sn-Se bonding along the a -direction. The two-atom-thick SnSe slabs are linked making a zig-zag accordion-like projection along the b -axis. The nature of SnSe is also originated from the high anharmonicity of its chemical bonds. The crystal structure of SnSe contains highly distorted SnSe₇ polyhedra due to lone pair of Sn²⁺ atoms (Figure 1. 10b). Sn atom is enclosed by seven Se atoms, which shows four long and three short Sn-Se bonds, which brings unbalanced forces around the Sn in SnSe₇ polyhedra.

The anomalously high Grüneisen parameter of SnSe also supports a high anharmonicity of chemical bonds, calculated by first-principles density-functional theory (DFT).^[31] Both highly distorted polyhedra and zigzag like geometry of slabs synergistically lead to the high value of Grüneisen parameter. Unlike in the b - and c -directions, it is estimated that SnSe can be easily deformed if mechanical force is applied along the a -direction. Further, the weaker bonding between SnSe slabs along a -direction can act as cushion, which prevents phonons from transport laterally. A consequence of “soft” bonding leads to the ultralow thermal conductivity and the unexpected

thermoelectric performance of the SnSe single crystals. Although, single crystals are not appropriate for broad applications because mass production of single crystal is difficult due to high cost as well as mechanical instability and poor machinability. As a result, it has been of prime interest in the TE community to develop polycrystalline SnSe materials with comparable TE performance to the single crystals.

Since the initial report of single crystal SnSe in 2014, a number of studies have been reported on this compound focusing mostly. Although, its polycrystalline form has significantly underperformed than its single crystal form mainly because of the apparently larger κ_{lat} .⁴⁴⁻⁴⁹ It is contrary to general understanding because the former has additional phonon scattering mechanisms. Very recently, the origin of the paradoxically high κ_{lat} in polycrystalline SnSe was revealed due to surface tin oxides on SnSe powder.⁴⁹ Chemical reduction process can effectively remove the oxide, leading to an exceptionally low $\kappa_{\text{lat}} \sim 0.11 \text{ W m}^{-1} \text{ K}^{-1}$ and $ZT \sim 2.5$ for p-type polycrystalline SnSe.

In contrast to the significant advance in p-type polycrystalline SnSe materials, the n-type counterparts remain largely underdeveloped. Only several literatures were reported, which exhibiting much lower performances than that of the p-type cousins.^[50-54] The difficulty in stabilizing an n-type charge carrier at the optimal level is the main reason because of a substantial

amount of inherent Sn vacancies and ubiquitous Sn^{4+} defects, making SnSe intrinsic p-type semiconductor. Just few n-type dopants have been reported to be effective for SnSe. For example, I_2 coupled with S, Br, BiCl_3 , and PbBr_2 improve ZT s of SnSe ranging from ~ 0.5 to ~ 1.3 .^[50-53] Because TE devices should consist of both n- and p-type semiconductors, the underperforming type of the couple limits the overall device efficiency.^[55] Consequently, it is essential to fundamentally understand how to stabilize n-type SnSe and further enhance their TE properties.

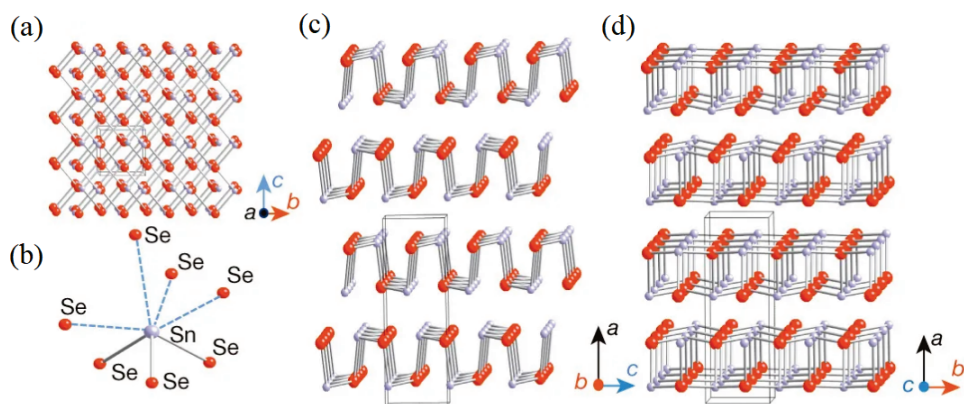


Fig. 1. 10. (a) Crystal structure of SnSe at room temperature along the a -axis (gray atoms are Sn and red atoms are Se). (b) Highly distorted SnSe₇ polyhedra showing three short and four long Sn–Se bonds. (c and d) SnSe crystal structures along the b - and c -axis, respectively, presenting the accordion like character. (from Ref. [31], Zhao, L. D.; Dravid, V.; Kanatzidis, M. G. *Energy Environ. Sci.*, **2014**, 7, 251-268)

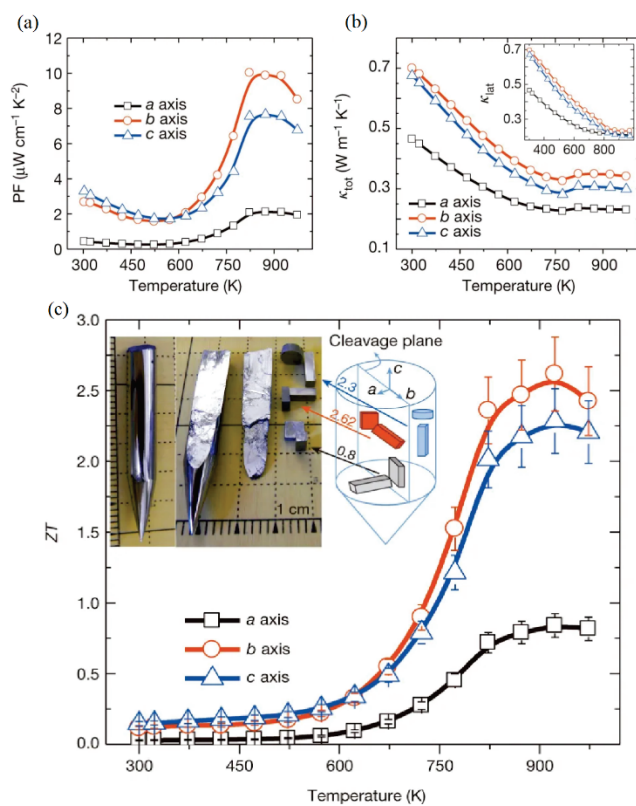


Figure 1. 11. Temperature dependent (a) power factor, (b) total thermal conductivity, and figure of merit ZT for single crystal SnSe along different axial direction. The inset of (b) presents their lattice thermal conductivity. (from Ref. [31], Zhao, L. D.; David, V.; Kanatzidis, M. G. *Energy Environ. Sci.*, **2014**, *7*, 251-268)

1.3.5. Increasing the power factor through band engineering

The above mentioned approaches are focused on strategy to reduce the lattice thermal conductivity. However, the power factor in all these cases can be reduced relative to the single phase pristine material because the imperfection of structure is able to increase the carrier scattering. Therefore, there is obviously room for enhancing thermoelectric performance and the continuing challenge in developing strategies to increase the power factor maintaining low thermal conductivity.

Despite of a number of struggles to enhance the power factor, a few way is proven to increase the power factor while maintaining thermal conductivity. It has been reported that band engineering is representatively effective way to enhance the power factor. This method enlarges the Seebeck coefficient without deterioration of electrical conductivity by the degeneracy of multiple valleys,^[56] electron energy barrier filtering,^[57,58] electronic resonance states,^[59] modulation doping,^[60] and depressing bipolar effect at high temperature.^[9]

The theory of Boltzmann transport describes both thermal and charge transport in the solids. Considering this theory, the thermopower and maximum Z can be defined in the Mott equation:

$$S = \frac{\pi^2 k^2 T}{3e} \left. \frac{d \ln \sigma(E)}{dE} \right|_{E=E_f}$$

$$Z_{max} \propto \gamma \frac{T^{3/2} \tau_z \sqrt{\frac{m_x m_y}{m_z}}}{k_{latt}} e^{(r+1/2)}$$

where γ is the degeneracy of band extrema, m_i is the effective mass of the carriers in the i direction. It indicates that the degeneracy of band extrema (γ) is the number of valleys in the valence or conduction band (relevant to type of materials). Because each band extremum can contribute both thermopower and electrical conductivity, increasing the number of degenerate valleys can enhance the power factor (Figure 1. 12).^[61] This is one of the general strategies to improve the performance of bulk thermoelectric materials. For example, it is reported that Se alloying in PbTe can induce a convergence of multiple valleys (Figure 1. 13), thereby obtaining the ZT of 1.8 at 850 K.^[56]

A remarkable increase in ZT has been reported through introducing impurity energy level, which enhance the Seebeck coefficient.^[62] If the impurities have energy levels in a band of the host material, the resonant energy levels can be introduced, which can distort the density of states near the Fermi level. It enhances the Seebeck coefficient, which is consistent with theoretical expectation (Figure 1.14).^[63] For instance, through the resonant level concept, the thermoelectric property in bulk Tl doped PbTe is

enhanced.^[59] Because introduced Tl creates a resonant level near the valence band edge of PbTe, the Seebeck coefficient is significantly enhanced over that of the bulk.

As mentioned above, strategies to reduce the lattice thermal conductivity are accompanied by a decrease in carrier mobility due to scattering of carriers. However, previously, it was reported that small band offsets between two Bi₂Te₃ and Sb₂Te₃ films can reduce the thermal conductivity with high mobility in superlattice components due to small band offsets that allow carriers to transport without difficulty. To date, similar to the previous report, this strategy to control and minimize of band offsets between different phases can be adopted to bulk systems.^[63] If the energy level of conduction bands for the matrix is similar with those of the second phase, the electron transmission through the materials should be more facile, and vice versa. The schematic graphic of Figure 1. 15 presents the overall operating concept. While there is a large difference in band gap between the matrix and second phase, the carriers can transport in the system because of small energy deviation.

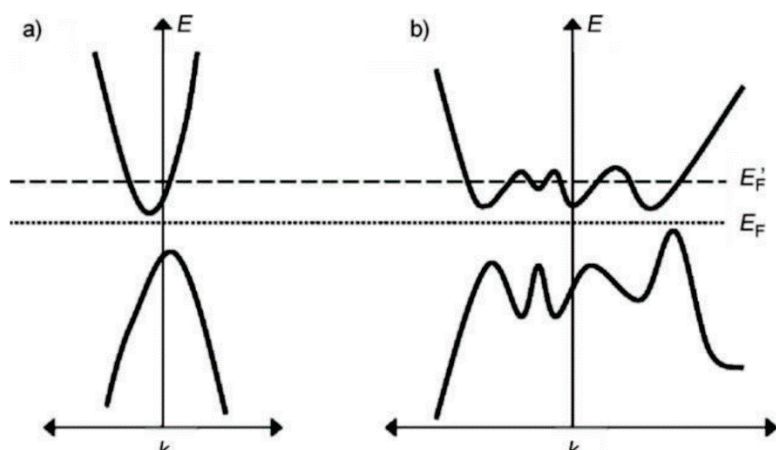


Figure 1. 12. Hypothetical band structure with a) single and b) multiple peaks. Because the power factor is proportional to the number of populated peaks, the system (b) will have a higher power factor. (from Ref. [61], Sootsman, J. R.; Chung, D. Y.; Kanatzidis, M. G. *Angew. Chem., Int. Ed.* **2009**, 48, 8616–8639.)

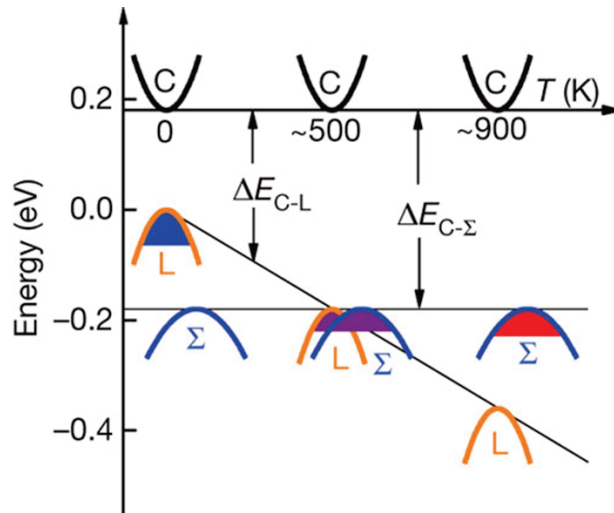


Figure 1. 13. Relative energy of the valence bands for $\text{PbTe}_{1-x}\text{Se}_x$. The two valence bands can converge at around 500 K, leading both the L and Σ bands to contribute transport. (C is a conduction band, L is a low degeneracy hole band, and Σ is a high degeneracy hole band, respectively. (from Ref. [56], Pei, Y.; Shi, X.; LaLonde, A.; Wang, H.; Chen, L.; Snyder, J. Convergence of Electronic Bands for High Performance Bulk Thermoelectrics. *Nature*, **2011**, 473, 66-69).

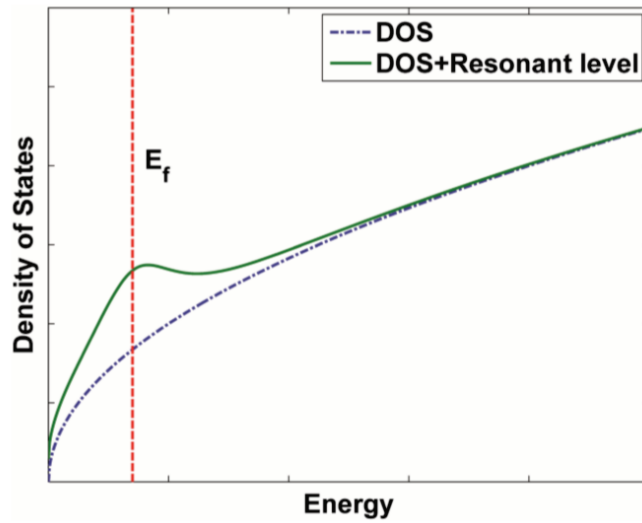


Figure 1. 14. Schematic illustration for the resonant level effect on the electronic density of states (DOS). (from Ref. [63], Minnich, A.; Dresselhaus, M.; Ren, Z.; Chen, G. Bulk Nanostructured Thermoelectric Materials: Current Research and Future Prospects. *Energy Environ. Sci.* **2009**, *2*, 466–479)

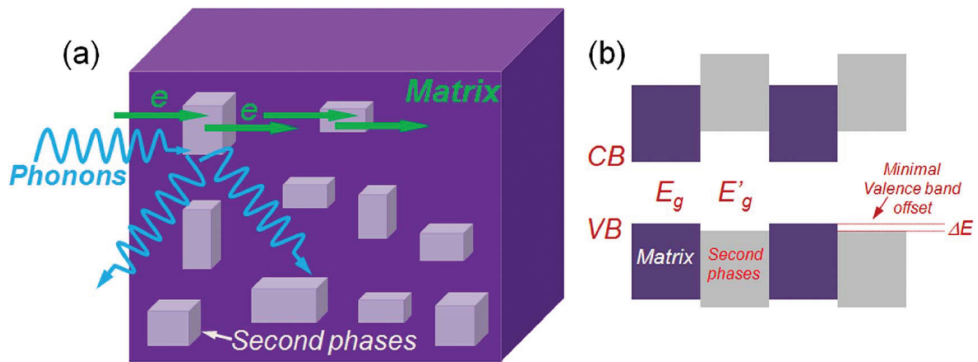


Figure 1. 15. (a) The small valence band offsets between matrix and second phase allow facile carrier transmission, simultaneously scattering heat carrying phonons at the matrix/second phase interface. (b) Schematically illustration for small band offset in valence band between matrix and second phase. (from Ref. [9], Zhao, L. D.; Dravid, V.; Kanatzidis, M. G. *Energy Environ. Sci.*, **2014**, 7, 251-268).

1.4 Dissertation Overview

Thermoelectric materials have drawn great attention as one of the novel renewable energy sources. Note that improving thermoelectric conversion performance should be achieved for practical and broader applications. The efficiency of thermoelectrics can be improved by developing compounds with new compositions and devising new synthetic methods. The current dissertation is focused on discovering the new bulk thermoelectric materials and understanding the origins of their high thermoelectric performance. Through those processes, I can propose new directions to design and explore advanced bulk thermoelectric materials.

The first part (Chapter 2) describes the thermoelectric performance of n-type polycrystalline SnSe, simultaneously incorporated of both Cl and PbSe. Importantly, despite the high anisotropic structure of SnSe, I can attain a comparable $ZT_{\max} \sim 1.2$ for n-type SnSe both parallel and perpendicular to the press direction of spark plasma sintering (SPS) using the dedicated preparation methods. This achievement is highly important in mass production and facile processability of thermoelectric materials. I employed a spherical aberration-corrected scanning transmission electron microscope (Cs-corrected STEM) to understand the crystal structure of $\text{Sn}_{0.90}\text{Pb}_{0.15}\text{Se}_{0.95}\text{Cl}_{0.05}$ at the atomic level and their effect on TE properties.

The second part (Chapter 3) describes a new n-type polycrystalline Bi₂Te₃ system with the nominal composition of Cu_xBi₂Te_{3.17} ($x = 0.02-0.06$) exhibiting ultrahigh power factor and carrier mobility near room temperature. These compounds are uniquely stabilized by the reaction of Bi₂Te₃ with excess Cu and Te and the subsequent consolidation by spark plasma sintering (SPS). The incorporation of high concentration of Cu atoms, enabled by excess Te in the reaction melt, induces unusual charge transport behaviors. The synergistic effect of excess Cu and Te leads to ultrahigh mobility of $\sim 467 \text{ cm}^2 \text{ V}^{-1} \text{ s}^{-1}$ and PF of $\sim 45 \text{ } \mu\text{W cm}^{-1} \text{ K}^{-2}$ for the $x = 0.06$ sample of SPS Cu_xBi₂Te_{3.17}. These are record high values reported to date for the polycrystalline n-type Bi₂Te₃-based materials

The third part (chapter 4) discuss the Fe–Ni metallization layers can bind skutterudite(SKD)-based thermoelectric legs and metallic electrodes with minimal loss of energy transfer across them to form high performance thermoelectric power generators. Its introduction is attributed to the lowest electrical contact resistivity of $\sim 2.3-2.5 \text{ } \mu\Omega \text{ cm}^2$ at the interface to date and resultant ultralow internal resistance of 42 m Ω . In comparison, top SKD-based TE modules exhibit 2–20 times larger values at 5–50 $\mu\Omega \text{ cm}^2$. Accordingly, minimizing it can be a key to achieving high power TE generators. Indeed, our device exhibits the maximum output power of 8.1W

and power density of 2.1 W cm^{-2} , driven by a temperature difference (ΔT) of 570 K.

1.5 References

- [1] Gingerich, D. B.; Mauter, M. S. Quantity, Quality, and Availability of Waste Heat from United States Thermal Power Generation. *Environ. Sci. Technol.* **2015**, *49*, 8297-8306.
- [2] Johnson, I.; Choate, W. T.; Davidson, A. Waste Heat Recovery: Technology and Opportunities in US Industry. *US Department of Energy Industrial Technologies Program* **2008**.
- [3] Banik, A.; Shenoy, U. S.; Saha, S.; Waghmare, U. V.; Biswas, K. High Power Factor and Enhanced Thermoelectric Performance of SnTe-AgInTe₂: Synergistic Effect of Resonance Level and Valence Band Convergence. *J. Am. Chem. Soc.* **2016**, *138*, 13068-13075.
- [4] Zhang, X.; Zhao, L. Thermoelectric materials: Energy conversion between heat and electricity. *J. Materiomics* **2015**, *1*, 92e105
- [5] Li J.; Liu W.; Zhao L.; Zhou M. High-performance Nanostructured Thermoelectric Materials. *Npg Asia Mater.* **2010**, *2*, 152e8.
- [6] Yang J. Special Section Papers on Thermoelectric Materials and Applications Foreword. *J Electron Mater.* **2007**, *36*, 703.
- [7] Yang J.; Caillat T. Thermoelectric Materials for Space and Automotive Power Generation. *Mrs Bull.* **2006**, *31*, 224e9.
- [8] Bubnova, O.; Crispin, X. Towards polymer-based organic thermoelectric generators. *Energy Environ. Sci.*, **2012**, *5*, 9345

- [9] Tan G.; Zhao L.; Kanatzidis M.G. Rationally Designing High-Performance Bulk Thermoelectric Materials. *Chem. Rev.* **2016**, 116, 12123–12149
- [10] Zhao, L. D.; Dravid, V.; Kanatzidis, M. G. The Panoscopic Approach to High Performance Thermoelectrics *Energy Environ. Sci.*, **2014**, 7, 251-268
- [11] Poudel, B.; Hao, Q.; Ma, Y.; Lan, Y.; Minnich, A.; Yu, B.; Yan, X.; Wang, D.; Muto, A.; Vashaee, D.; et al. High-Thermoelectric Performance of Nanostructured Bismuth Antimony Telluride Bulk Alloys. *Science* **2008**, 320, 634–638.
- [12] Biswas, K.; He, J.; Zhang, Q.; Wang, G.; Uher, C.; Dravid, V. P.; Kanatzidis, M. G. Strained Endotaxial Nanostructures with High Thermoelectric Figure of Merit. *Nat. Chem.* **2011**, 3, 160–166.
- [13] Biswas, K.; He, J.; Blum, I. D.; Wu, C.-I.; Hogan, T. P.; Seidman, D. N.; Dravid, V. P.; Kanatzidis, M. G. High-Performance Bulk Thermoelectrics with All-Scale Hierarchical Architectures. *Nature* **2012**, 489, 414–418.
- [14] Vineis, C. J.; Shakouri, A.; Majumdar, A.; Kanatzidis, M. G. Nanostructured Thermoelectrics: Big Efficiency Gains from Small Features. *Adv. Mater.* **2010**, 22, 3970–3980.
- [15] Joshi, G.; Lee, H.; Lan, Y.; Wang, X.; Zhu, G.; Wang, D.; Gould, R. W.; Cuff, D. C.; Tang, M. Y.; Dresselhaus, M. S.; et al. Enhanced Thermoelectric Figure-of-Merit in Nanostructured P-Type Silicon Germanium Bulk Alloys. *Nano Lett.* **2008**, 8, 4670–4674.

- [16] Bux, S. K.; Blair, R. G.; Gogna, P. K.; Lee, H.; Chen, G.; Dresselhaus, M. S.; Kaner, R. B.; Fleurial, J. P. Nanostructured Bulk Silicon as an Effective Thermoelectric Material. *Adv. Funct. Mater.* **2009**, 19, 2445–2452.
- [17] Dresselhaus M. Overview of thermoelectrics for thermal to electrical energy conversion. In: Linke H, Borgstrom M, Pullerits T, Samuelson L, Sundstrom V, Inganas O, editors. Nobel symposium 153: nanoscale energy converters; 2013. p. 36e9.
- [18] Snyder J.; Toberer E. Complex Thermoelectric Materials. *Nat. Mater.* **2008**, 7, 105e14.
- [19] Boydston, R. W. Thermo-Electric Effect in Single-Crystal Bismuth. *Phys. Rev.* **1927**, 30, 911–921.
- [20] Henkels, H. W. Thermoelectric Power and Mobility of Carriers in Selenium. *Phys. Rev.* **1950**, 77, 734–736.
- [21] Soroos, A. Thermoelectric Power of Single Crystal Bismuth near the Melting Point. *Phys. Rev.* **1932**, 41, 516–522.
- [22] Bidwell, C. C. Electrical Resistance and Thermo-Electric Power of the Alkali Metals. *Phys. Rev.* **1924**, 23, 357–376.
- [23] Greenwood, N.; Anderson, J. Conductivity and Thermoelectric Effect in Cuprous Oxide. *Nature* **1949**, 164, 346–347.
- [24] Andrews, J. Thermoelectric Power of Cadmium Oxide. *Proc. Phys. Soc.* **1947**,

59, 990–998.

[25] Bidwell, C. C. Electrical and Thermal Properties of Iron Oxide. *Phys. Rev.* **1917**, 10, 756–766.

[26] Goldsmid, H.; Douglas, R. The Use of Semiconductors in Thermoelectric Refrigeration. *Br. J. Appl. Phys.* **1954**, 5, 386–390.

[27] Herring, C. Theory of the Thermoelectric Power of Semiconductors. *Phys. Rev.* **1954**, 96, 1163–1187.

[28] Price, P. Theory of Transport Effects in Semiconductors: Thermoelectricity. *Phys. Rev.* **1956**, 104, 1223–1239.

[29] Korkosz, R. J.; Chasapis, T. C.; Lo, S.-h.; Doak, J. W.; Kim, Y. J.; Wu, C.-I.; Hatzikraniotis, E.; Hogan, T. P.; Seidman, D. N.; Wolverton, C.; et al. High ZT in P-Type $(\text{PbTe})_{1-2x}(\text{PbSe})_x(\text{PbS})_x$ Thermoelectric Materials. *J. Am. Chem. Soc.* **2014**, 136, 3225–3237.

[30] Wu, D.; Zhao, L.-D.; Tong, X.; Li, W.; Wu, L.; Tan, Q.; Pei, Y.; Huang, L.; Li, J.-F.; Zhu, Y.; Kanatzidis, M. G.; He, J. Superior Thermoelectric Performance in PbTe-PbS Pseudo-Binary: Extremely Low Thermal Conductivity and Modulated Carrier Concentration. *Energy Environ. Sci.* **2015**, 8, 2056–2068.

[31] Zhao, L.-D.; Lo, S.-H.; Zhang, Y.; Sun, H.; Tan, G.; Uher, C.; Wolverton, C.; Dravid, V. P.; Kanatzidis, M. G. Ultralow Thermal Conductivity and High Thermoelectric Figure of Merit in SnSe Crystals. *Nature* **2014**, 508, 373–377.

- [32] Shi, X.; Yang, J.; Salvador, J. R.; Chi, M.; Cho, J. Y.; Wang, H.; Bai, S.; Yang, J.; Zhang, W.; Chen, L. Multiple-Filled Skutterudites: High Thermoelectric Figure of Merit through Separately Optimizing Electrical and Thermal Transports. *J. Am. Chem. Soc.* **2011**, 133, 7837–7846.
- [33] Callaway, J. Model for Lattice Thermal Conductivity at Low Temperatures. *Phys. Rev.* 1959, 113, 1046–1051.
- [34] Callaway, J.; von Baeyer, H. C. Effect of Point Imperfections on Lattice Thermal Conductivity. *Phys. Rev.* 1960, 120, 1149–1154.
- [35] Hsu, K. F.; Loo, S.; Guo, F.; Chen, W.; Dyck, J. S.; Uher, C.; Hogan, T.; Polychroniadis, E. K.; Kanatzidis, M. G. Cubic $\text{AgPb}_m\text{SbTe}_{2+m}$: Bulk Thermoelectric Materials with High Figure of Merit. *Science* **2004**, 303, 818
- [36] Tan, G.; Liu, W.; Chi, H.; Su, X.; Wang, S.; Yan, Y.; Tang, X.; Wong-Ng, W.; Uher, C. Realization of High Thermoelectric Performance in P-Type Unfilled Ternary Skutterudites $\text{FeSb}_{2+x}\text{Te}_{1-x}$ via Band Structure Modification and Significant Point Defect Scattering. *Acta Mater.* **2013**, 61, 7693–7704.
- [37] Tan, G.; Wang, S.; Tang, X. High Thermoelectric Figure of Merit of P-Type Ternary Unfilled Skutterudite FeSb_2Te Via Ge Doping. *Sci. Adv. Mater.* **2013**, 5, 1974–1982.
- [38] Meisner, G.; Morelli, D.; Hu, S.; Yang, J.; Uher, C. Structure and Lattice Thermal Conductivity of Fractionally Filled Skutterudites: Solid Solutions of Fully Filled and Unfilled End Members. *Phys. Rev. Lett.* **1998**, 80, 3551–3554.

- [39] Androulakis, J.; Lin, C.-H.; Kong, H.-J.; Uher, C.; Wu, C.-I.; Hogan, T.; Cook, B. A.; Caillat, T.; Paraskevopoulos, K. M.; Kanatzidis, M. G. Spinodal Decomposition and Nucleation and Growth as a Means to Bulk Nanostructured Thermoelectrics: Enhanced Performance in $\text{Pb}_{1-x}\text{Sn}_x\text{Te-PbS}$. *J. Am. Chem. Soc.* **2007**, 129, 9780–9788.
- [40] Zhao, L.; Wu, H.; Hao, S.; Wu, C.-I.; Zhou, X.; Biswas, K.; He, J.; Hogan, T. P.; Uher, C.; Wolverton, C.; et al. All-Scale Hierarchical Thermoelectrics: MgTe in PbTe Facilitates Valence Band Convergence and Suppresses Bipolar Thermal Transport for High Performance. *Energy Environ. Sci.* **2013**, 6, 3346–3355.
- [41] Biswas, K.; He, J.; Wang, G.; Lo, S.-H.; Uher, C.; Dravid, V. P.; Kanatzidis, M. G. High Thermoelectric Figure of Merit in Nanostructured P-Type PbTe-MTe ($\text{M}=\text{Ca, Ba}$). *Energy Environ. Sci.* **2011**, 4, 4675–4684.
- [42] Tan, G.; Wang, S.; Li, H.; Yan, Y.; Tang, X. Enhanced Thermoelectric Performance in Zinc Substituted P-Type Filled Skutterudites $\text{CeFe}_{4-x}\text{Zn}_x\text{Sb}_{12}$. *J. Solid State Chem.* **2012**, 187, 316–322.
- [43] Zheng, Y.; Zhang, Q.; Su, X.; Xie, H.; Shu, S.; Chen, T.; Tan, G.; Yan, Y.; Tang, X.; Uher, C.; Snyder, G. J. Mechanically Robust BiSbTe Alloys with Superior Thermoelectric Performance: A Case Study of Stable Hierarchical Nanostructured Thermoelectric Materials. *Adv. Energy Mater.* **2015**, 5, 1401391.
- [44] Lee, Y. K.; Ahn, K.; Cha, J.; Zhou, C.; Kim, H. S.; Choi, G.; Chae, S. I.; Park, J.-H.; Cho, S.-P.; Park, S. H.; Sung, Y.-E.; Lee, W. B.; Hyeon, T.; Chung, I.

Enhancing p-Type Thermoelectric Performances of Polycrystalline SnSe via Tuning Phase Transition Temperature. *J. Am. Chem. Soc.* **2017**, 139, 10887–10896.

[45] Ge, Z. H.; Song, D.; Chong, X.; Zheng, F.; Jin, L.; Qian, X.; Zheng, L.; Dunin-Borkowski, R. E.; Qin, P.; Feng, J.; Zhao, L. D. Boosting the Thermoelectric Performance of (Na,K)-Codoped Polycrystalline SnSe by Synergistic Tailoring of the Band Structure and Atomic-Scale Defect Phonon Scattering. *J. Am. Chem. Soc.* **2017**, 139, 9714–9720.

[46] Pei, Y.; Shi, X.; LaLonde, A.; Wang, H.; Chen, L.; Snyder, J. Convergence of Electronic Bands for High Performance Bulk Thermoelectrics. *Nature*, **2011**, 473, 66-69

[46] Zhao, L. D.; Tan, G.; Hao, S.; He, J.; Pei, Y.; Chi, H.; Wang, H.; Gong, S.; Xu, H.; Dravid, V. P.; Uher, C.; Snyder, G. J.; Wolverton, C.; Kanatzidis, M. G. Ultrahigh Power Factor and Thermoelectric Performance in Hole-Doped Single-Crystal SnSe. *Science* **2016**, 351, 141–144.

[47] Wei, T. R.; Tan, G.; Zhang, X.; Wu, C. F.; Li, J. F.; Dravid, V. P.; Snyder, G. J.; Kanatzidis, M. G. Distinct Impact of Alkali-Ion Doping on Electrical Transport Properties of Thermoelectric p-Type Polycrystalline SnSe. *J. Am. Chem. Soc.* **2016**, 138, 8875–8882.

[48] Wei, T.-R.; Tan, G.; Wu, C.-F.; Chang, C.; Zhao, L.-D.; Li, J.-F.; Snyder, G. J.; Kanatzidis, M. G. Thermoelectric Transport Properties of Polycrystalline SnSe Alloyed with PbSe. *Appl. Phys. Lett.* **2017**, 110, No. 053901.

- [49] Lee, Y. K.; Luo, Z.; Cho, S.-P.; Kanatzidis, M. G.; Chung, I. Surface Oxide Removal for Polycrystalline SnSe Reveals Near-Single-Crystal Thermoelectric Performance. *Joule* **2019**, *3*, 719–731.
- [50] Zhang, Q.; Chere, E. K.; Sun, J.; Cao, F.; Dahal, K.; Chen, S.; Chen, G.; Ren, Z. Studies on Thermoelectric Properties of n-Type Polycrystalline SnSe_{1-x}S_x by Iodine Doping. *Adv. Energy Mater.* **2015**, *5*, 1500360.
- [51] Wang, X.; Xu, J.; Liu, G.; Fu, Y.; Liu, Z.; Tan, X.; Shao, H.; Jiang, H.; Tan, T.; Jiang, J. Optimization of Thermoelectric Properties in n-Type SnSe Doped with BiCl₃. *Appl. Phys. Lett.* **2016**, *108*, 083902.
- [52] Li, S.; Wang, Y.; Chen, C.; Li, X.; Xue, W.; Wang, X.; Zhang, Z.; Cao, F.; Sui, J.; Liu, X.; Zhang, Q. Heavy Doping by Bromine to Improve the Thermoelectric Properties of n-type Polycrystalline SnSe. *Adv. Sci.* **2018**, *5*, 1800598.
- [53] Li, D.; Tan, X.; Xu, J.; Liu, G.; Jin, M.; Shao, H.; Huang, H.; Zhang, J.; Jiang, J. Enhanced Thermoelectric Performance in n-Type Polycrystalline SnSe by PbBr₂ Doping. *RSC Adv.* **2017**, *7*, 17906-17912.
- [54] Chang, C.; Tan, Q.; Pei, Y.; Xiao, Y.; Zhang, X.; Chen, Y.-X.; Zheng, L.; Gong, S.; Li, J.-F.; He, J.; Zhao, L.-D. Raising Thermoelectric Performance of n-Type SnSe via Br Doping and Pb Alloying. *RSC Adv.* **2016**, *6*, 98216-98220.
- [55] Park, S. H.; Jin, Y.; Cha, J.; Hong, K.; Kim, Y.; Yoon, H.; Yoo, C.-Y.; Chung, I. High-Power-Density Skutterudite-Based Thermoelectric Modules with Ultralow Contact Resistivity Using Fe–Ni Metallization Layers. *ACS Appl. Energy Mater.* **2018**, *1*, 1603-1611.

- [56] Pei, Y.; Shi, X.; LaLonde, A.; Wang, H.; Chen, L.; Snyder, J. Convergence of Electronic Bands for High Performance Bulk Thermoelectrics. *Nature*, **2011**, 473, 66-69
- [57] Heremans, J. P.; Thrusch, C. M.; Morelli, D. T. Theory of Enhancement of Thermoelectric Properties of Materials with Nanoinclusions. *Phys. Rev. B*, **2004**, 70, 115334
- [58] Faleev, S. V.; Léonard, F. Thermopower Enhancement in Lead Telluride Nanostructures. *Phys. Rev. B*, **2004**, 70, 115334
- [59] Heremans, J. P.; Jovovic, V.; Toberer, E. S.; Saramat, A.; Kurosaki, K.; Charoenphakdee, A.; Yamanaka, S.; Snyder, G. J. Enhancement of Thermoelectric Efficiency in PbTe by Distortion of the Electronic Density of States. *Science* **2008**, 321, 554-557.
- [60] Zebarjadi, M.; Joshi, G.; Zhu, G.; Yu, B.; Minnich, A.; Lan, Y.; Wang, X.; Dresselhaus, M.; Ren, Z.; Chen, G. Power Factor Enhancement by Modulation Doping in Bulk Nanocomposites. *Nano Lett.* **2011**, 11, 2225–2230.
- [61] Sootsman, J. R.; Chung, D. Y.; Kanatzidis, M. G. New and Old Concepts in Thermoelectric Materials. *Angew. Chem., Int. Ed.* **2009**, 48, 8616–8639.
- [62] Poudeu, P. F. R.; D'Angelo, J.; Downey, A. D.; Short, J. L.; Hogan, T. P.; Kanatzidis, M. G. High Thermoelectric Figure of Merit and Nanostructuring in Bulk P-Type $\text{Na}_{1-x}\text{Pb}_m\text{Sb}_y\text{Te}_{m+2}$. *Angew. Chem., Int. Ed.* **2006**, 45, 3835–3839.

- [63] Minnich, A.; Dresselhaus, M.; Ren, Z.; Chen, G. Bulk Nanostructured Thermoelectric Materials: Current Research and Future Prospects. *Energy Environ. Sci.* **2009**, 2, 466–479.)
- [64] Venkatasubramanian, R.; Siivola, E.; Colpitts, T.; O’Quinn, B. Thin-film Thermoelectric Devices with High Room-Temperature Figures of Merit. *Nature*, **2001**, 413, 597–602.

Chapter 2. High Thermoelectric Performance in n-Type Polycrystalline SnSe via Dual Incorporation of Cl and PbSe and Dense Nanostructures

2.1 Introduction

The rapid growth of the global population causes the dramatic escalation in energy demand. Meanwhile, environmental problems ask to reduce the use of traditional fossil fuels and to develop sustainable and environmentally friendly alternative energy resources. In fact, fossil fuels are a major resource to obtain electricity and approximately two-third of them is being discarded as waste heat. Hence, recovery of this huge energy loss can concurrently contribute to solving global energy crisis and environmental problems by enhancing energy efficiency and reducing the evolution of green-house gases.^{1,2} Thermoelectric (TE) technology is a good candidate for these purposes because it directly converts heat into electric energy without releasing undesirable gaseous chemical residues such as CO₂ and NO_x. TE power generators are mechanically reliable and environmentally stable electronic devices, operating without mechanical vibration and noise. The main interest in this technology is improving TE conversion performance for

broader applications.³⁻¹⁶ The capability of TE materials is typically evaluated by a dimensionless figure of merit $ZT = \sigma S^2 T / (\kappa_{\text{ele}} + \kappa_{\text{lat}})$, where σ is the electrical conductivity, S is the Seebeck coefficient, the product σS^2 is the power factor (PF), κ_{ele} and κ_{lat} are the electrical and lattice thermal conductivity, and T is the absolute temperature.¹⁷⁻¹⁹

PbTe has served as a representative TE material operating in the intermediate temperature range (600 – 900 K) over past sixty years.²⁰⁻²⁵ For example, 2% Na-doped PbTe-8% SrTe system exhibits a ZT of ~ 2.5 at 923 K.²⁶ The prototype PbTe-based TE modules exhibit high power conversion efficiency of $\sim 12\%$.²⁷ However, because an abundance of Te in the Earth's crust is similar to Pt, the focus of thermoelectric research has shifted toward discovery of alternative materials consisting of earth abundant elements while performing comparably. Although Se is fifty-fold more abundant than Te and Sn is a nontoxic congener of Pb, their simple binary compound SnSe has been historically neglected for TE applications because of its apparent high electrical resistivity. In recent years, record high ZT values larger than 2.6 at 773 – 923 K have been discovered for single crystal samples of pristine and doped SnSe.^{28, 29} This extraordinarily high TE performance is mainly attributed to unique anisotropic crystal chemistry of SnSe. However, SnSe single crystals are arguably inappropriate for mass production and broad-based applications of TE technology because of high cost as well as

mechanical instability and poor machinability by its layered structure. As a result, it has been of prime interest in the TE community to develop polycrystalline SnSe materials with comparable TE performance to the single crystals.

Polycrystalline SnSe has significantly underperformed single crystal samples mainly due to the apparently larger κ_{lat} than latter.³⁰⁻³⁵ It is highly unusual in that the former has additional phonon scattering mechanisms. Recently, the origin of the paradoxically high κ_{lat} in polycrystalline SnSe was uncovered to be surface tin oxides on SnSe powder.³⁵ It can be effectively removed by the oxide removing strategy employing chemical reduction process, leading to an exceptionally low $\kappa_{\text{lat}} \sim 0.11 \text{ W m}^{-1} \text{ K}^{-1}$ and $ZT \sim 2.5$ for p-type polycrystalline SnSe.

In contrast to the advance in p-type polycrystalline SnSe materials, the n-type counterparts have been largely underdeveloped. Only several literatures were published and they exhibit much inferior performances to the p-type cousins.³⁶⁻⁴⁰ The main reason is difficulty in stabilizing an n-type charge carrier at the optimal level because of a substantial amount of inherent Sn vacancies and ubiquitous Sn^{4+} defects, making SnSe intrinsic p-type semiconductor. Just few n-type dopants have been reported to be effective for SnSe. For example, I_2 coupled with S, Br, BiCl_3 , and PbBr_2 improve ZT s of SnSe ranging from ~ 0.5 to ~ 1.3 .³⁶⁻³⁹ Because TE devices should consist

of both n- and p-type semiconductors, the underperforming type of the couple limits the overall device efficiency.^{27, 41, 42} Consequently, it is essential to fundamentally understand how to stabilize n-type SnSe and further enhance their TE properties.

Here I report new highly efficient polycrystalline n-type SnSe materials by dually incorporating the high extent of PbSe and Cl. They synergistically contribute to improving charge transport and reducing thermal conductivity concurrently. I address a strong preference to the p-type conduction of SnSe-based materials employing the multiple processes as follows. We first synthesized a series of $\text{SnSe}_{1-y}\text{Cl}_y$ ($y = 0 - 0.08$). An apparent n-type dopant Cl stabilizes the n-type conduction for samples with y larger than 0.02. Despite maximum ZT (ZT_{max}) of ~ 0.8 obtained for the sample with $y = 0.05$, electron concentration (n_{H}) is still low at $\sim 4.5 \times 10^{18} \text{ cm}^{-3}$ for TE power generation and resultantly electrical conductivity (σ) is too poor. Then, I introduced excess Sn to fill ubiquitous Sn vacancies in SnSe structure, obtaining a series of $\text{Sn}_{1+z}\text{Se}_{0.95}\text{Cl}_{0.05}$ ($z = 0 - 0.10$). As a result, n_{H} increases moderately to $\sim 1.0 \times 10^{19} \text{ cm}^{-3}$ and ZT_{max} of ~ 0.9 is achieved with the optimal excess Sn level of 0.05. Finally, we alloyed PbSe to further optimize n_{H} for n-type SnSe. Replacing Sn by Pb can suppress the generation of intrinsic Sn vacancies because Pb almost exclusively adopts the formal charge of 2+.

PbSe alloying concurrently enhances charge transport and reduces lattice thermal conductivity, leading to high ZT values for n-type SnSe.

Importantly, despite highly anisotropic structure of SnSe, I can attain a comparable $ZT_{\max} \sim 1.2$ for n-type SnSe both parallel and perpendicular to the press direction of spark plasma sintering (SPS) using the dedicated preparation methods. Namely, $ZT_{\max} \sim 1.1$ is achieved along the parallel direction of SPS for samples synthesized by high temperature solid-state reaction. When the samples are further processed by ball-mill and post-annealing, their thermoelectric properties become much more isotropic, exhibiting a $ZT_{\max} \sim 1.2$ along both the directions of SPS. This achievement is highly important in mass production and facile processibility of TE materials. In fact, both p- and n-type polycrystalline SnSe materials have been reported to show highly anisotropic TE properties due to the characteristic layered structure and thereby highly ordered texture in specimens. For example, p-type $\text{Sn}_{1-x}\text{Pb}_x\text{Se}$ doped with 1% Na shows a ZT_{\max} of ~ 1.2 and 0.8 at 773 K perpendicular and parallel to the consolidating press direction, respectively.³⁰ N-type $\text{Sn}_{1-x}\text{Pb}_x\text{Se}$ incorporated with Br exhibits the reversed trend of ZT_{\max} of ~ 0.7 and 1.2 at 823 K along the same directions as the former, respectively.⁴⁰

Nanostructures in n-type polycrystalline SnSe materials have been scarcely studied despite their substantial influence on TE properties. I

employed a spherical aberration-corrected scanning transmission electron microscope (Cs-corrected STEM) to understand crystal structure of $\text{Sn}_{0.90}\text{Pb}_{0.15}\text{Se}_{0.95}\text{Cl}_{0.05}$ at the atomic level and their effect on TE properties. In contrast to the p-type counterparts,^{30, 31} it contains highly dense edge dislocations and strain fields that can significantly reduce lattice thermal conductivity.

2.2 Experimental section.

2.2.1 Reagents. The reagents employed in this work were used as obtained unless noted otherwise: Sn chunk (99.999%, American Elements, US), Se shot (99.999%, 5N Plus, Canada), anhydrous SnCl₂ powder (99.99%, Sigma-Aldrich, US), and Pb wire (99.99%, 5N Plus, Canada).

2.2.2 Synthesis. The synthesis of cation-excess “Sn_{1.05-x}Pb_xSe_{0.95}Cl_{0.05}” ($x = 0, 0.05, 0.10, 0.15, 0.20$) ingots was achieved by reacting an appropriate ratio of starting reagents in 13 mm carbon-coated, evacuated fused-silica tubes ($\sim 10^{-4}$ Torr) at 1223 K for 6 h, followed by quenching to water. Afterward, we will use the nominal composition for specimens. The obtained ingots were ground into powder, sieved to $< 45 \mu\text{m}$, and loaded into a 13 mm diameter graphite die in an Ar-filled glovebox. All samples were densified by spark plasma sintering (SPS) (SPS-211Lx, Fuji Electronic Industrial Co., Japan) in 783 K for 5 min under an axial pressure of 50 MPa. The resulting samples are denoted as melt-synthesized (MS) sample. To reduce undesirable anisotropy in TE properties, we developed a two-step process. The melt-synthesized ingot was ball-milled at 250 rpm for 24 h, followed by annealing at 473 K for 4 h under an Ar atmosphere. The obtained powder was similarly densified as described above. The resulting sample is denoted as ball-milled and annealed (BA) sample. Figure 2. 1 shows typical images of SPS-processed pellets.

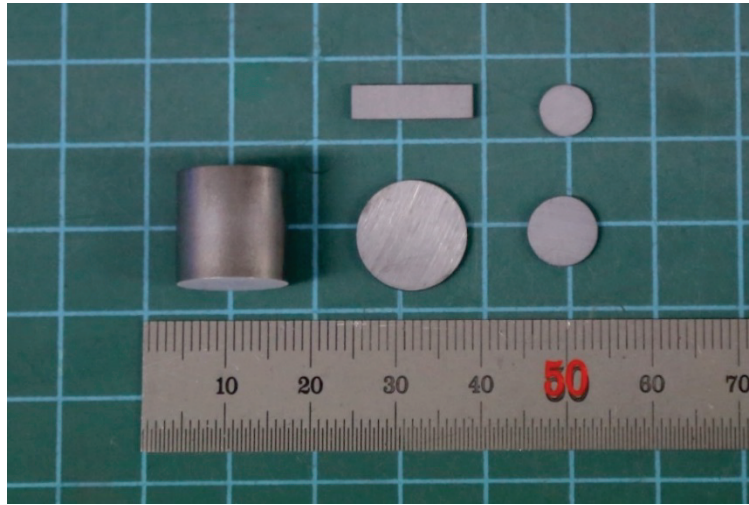


Figure 2. 1. Typical dense pellets prepared by an SPS process with a typical diameter of 13 mm and a height of ~14 mm. The obtained specimens were cut and polished for measuring electrical (a disk for measurements perpendicular to the SPS press direction and a bar for measurements parallel to the SPS press direction) and thermal transport properties (a small disk).

2.2.3 Powder X-ray diffraction (XRD). Powder XRD patterns were obtained using a calibrated SmartLab Rigaku powder X-ray diffractometer with Cu K α ($\lambda = 1.5418 \text{ \AA}$) graphite monochromatized radiation operating at 40 kV and 30 mA at room temperature.

2.2.4 Electrical transport properties. The pressed samples were cut and polished into parallelepipeds with dimensions approximately $13 \times 2 \times 2 \text{ mm}^3$ and disks with a diameter of 13mm and a thickness of 2 mm. The electrical conductivity and Seebeck coefficient were recorded simultaneously from room temperature to 823 K under an Ar atmosphere with a Netzsch SBA 458 Nemesis instrument.

2.2.5 Thermal transport properties. The pressed samples were cut and polished into disks with a radius of $\sim 6 \text{ mm}$ and a thickness of $\sim 1 \text{ mm}$ under a N $_2$ atmosphere. Disks were coated with graphite before measurement. The thermal diffusivity (D) was directly taken by the laser flash diffusivity method in a Netzsch LFA 457 MicroFlash system. The thermal conductivity was calculated from $\kappa_{\text{tot}} = D \cdot C_p \cdot \rho$, where C_p is the specific heat capacity and ρ is the mass density of the specimens. The C_p was derived indirectly employing a standard sample of Pyroceram. The ρ was determined based on geometrical dimensions and masses of the specimens. The total thermal conductivity (κ_{tot}) is a sum of the electrical (κ_{ele}) and lattice thermal (κ_{lat}) conductivity. The κ_{ele}

was evaluated by the Wiedemann-Franz relation $\kappa_{\text{ele}} = L \cdot \sigma \cdot T$, where L is the temperature-dependent Lorenz number. The κ_{lat} was obtained by subtracting the κ_{ele} from the κ_{tot} .

2.2.6 Hall coefficient measurement. The temperature-dependent Hall effect measurement in a 1.5 T magnetic field was conducted on a Lake Shore HMS8407 system. The carrier concentration (n_H) and mobility (μ_H) were obtained by the formula $n_H = I / (e \cdot R_H)$ and $\mu_H = \sigma \cdot R_H$, respectively.

2.2.7 Differential thermal analysis (DTA). Differential thermal analysis was performed on a Shimadzu DTA-50 instrument. A ground sample (~50 mg) was sealed in a silica ampule under vacuum ($\sim 10^{-4}$ Torr). A similar ampule with equal mass of Al_2O_3 was prepared for reference. The sample was heated to 650 °C at a rate of 10 °C min^{-1} , and after 3 min it was cooled at a rate of -10 °C min^{-1} to 80 °C.

2.2.8 Transmission electron microscope (TEM) and scanning TEM (STEM) measurements.

For cross-sectional STEM investigations, specimens were carbon-sputtered for surface protection, followed by applying focused ion beams (FIB, Helios 650, FEI) with a dual beam microscope using gallium ion milling and further polishing with a low-voltage and low-angle argon ion beam milling apparatus (NANO MILL, Model 1040, FISCHIONE). STEM analyses were performed

in a JEM ARM-200F microscope (Cold FEG Type, JEOL) equipped with a probe aberration CEOS corrector at 80 kV and a Silicon Drift Detector (SDD) type energy dispersive X-ray spectroscopy (EDS) detector (Solid Angle 0.9 sr, X-MaxN 100TLE, OXFORD), installed at the National Center for Inter-university Research Facilities (NCIRF) at Seoul National University. High angle annular dark-field STEM images were taken using a JEOL annular field detector with a fine imaging probe at a current of approximately 14 pA and the angular range of the annular detector from 68 mrad to 280 mrad. For STEM-EDS analyses. The probe size used was 80 pA and the CL aperture size was 40 μm . Geometric phase analysis (GPA) was performed using the plugin GPA Phase 4.1 (HREM Research) for the software package DigitalMicrograph GMS 3.1 (Gatan), based on the original algorithm by Hytch.⁴³

2.3 Results and Discussion

2.3.1 Structural characterization

Because all thermoelectric (TE) data for $\text{Sn}_{1.05-x}\text{Pb}_x\text{Se}_{0.95}\text{Cl}_{0.05}$ system ($x = 0 - 0.20$) discussed in this work were measured for dense pellet samples prepared by spark plasma sintering (SPS), we reground SPS-processed pellets to take powder X-ray diffraction (PXRD) patterns. The cation-rich $\text{Sn}_{1.05-x}\text{Pb}_x\text{Se}_{0.95}\text{Cl}_{0.05}$ crystallizes in GeS-type, *Pnma* orthorhombic structure (PDF# 48-1224) with the extra Bragg peaks at 32° and 45° indexed for elemental Sn (PDF# 86-2264) (Figure 2. 2). Similarly, $\text{SnSe}_{0.95}$ that contains the same level of excess Sn also gives Sn precipitates.³⁷ When the mole fraction of PbSe alloying is larger than ~ 0.20 , elemental Pb starts to be isolated. The cell dimension expands along the *a*- and *b*- axes and contracts through the *c*- direction, demonstrating the anisotropic expansion of the cell volume upon replacing Sn by larger Pb atom (Figure 2. 3). This trend is consistent with the behavior of $\text{Sn}_{1-x}\text{Pb}_x\text{Se}$ compounds.³⁰ The refined lattice parameters for $\text{Sn}_{0.90}\text{Pb}_{0.15}\text{Se}_{0.95}\text{Cl}_{0.05}$ are $a = 11.558(9) \text{ \AA}$, $b = 4.183(9) \text{ \AA}$, $c = 4.424(5) \text{ \AA}$, and $V = 213.979(6) \text{ \AA}^3$ in comparison with $a = 11.500(2) \text{ \AA}$, $b = 4.158(2) \text{ \AA}$, $c = 4.447(1) \text{ \AA}$, and $V = 212.642(8) \text{ \AA}^3$ for SnSe and $a = 11.476(7) \text{ \AA}$, $b = 4.144(0) \text{ \AA}$, $c = 4.437(1) \text{ \AA}$, and $V = 211.053(7) \text{ \AA}^3$ for $\text{SnSe}_{0.95}\text{Cl}_{0.05}$.

Figure 2. 4 displays plain view and the corresponding elemental maps on the polished surface of the SPS-processed $\text{Sn}_{0.90}\text{Pb}_{0.15}\text{Se}_{0.95}\text{Cl}_{0.05}$ sample by scanning electron microscope (SEM) equipped with an energy dispersive X-ray spectroscopy (EDS). The presence of segregated elemental Sn in the size of $\sim 20\ \mu\text{m}$ is observed, which is consistent with the results of PXRD. The other elements appear to be distributed homogeneously within the detection limit of SEM-EDS.

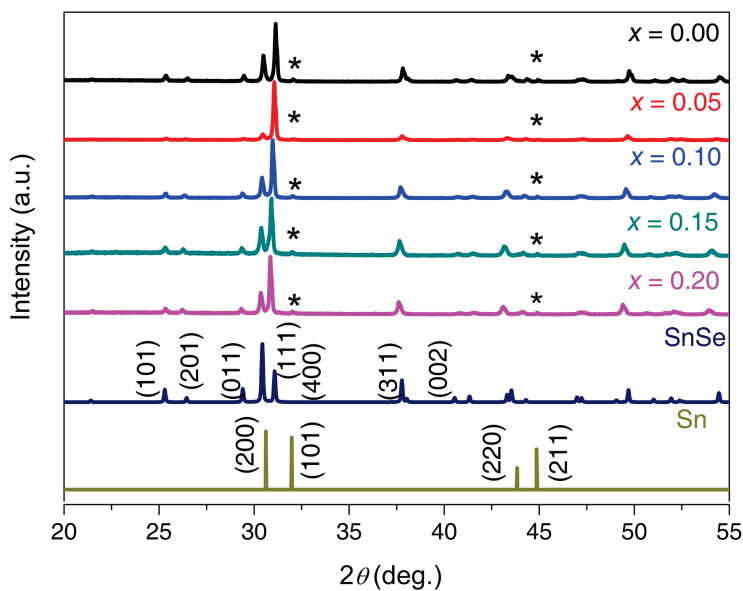


Figure 2. 2. Powder X-ray diffraction data for the melt-synthesized $\text{Sn}_{1.05-x}\text{Pb}_x\text{Se}_{0.95}\text{Cl}_{0.05}$ ($x = 0-0.2$) samples compared with the simulated patterns of SnSe (the International Center for Diffraction Data PDF 48-1224) and Sn (PDF 86-2264). Sn Bragg peaks are marked by asterisks.

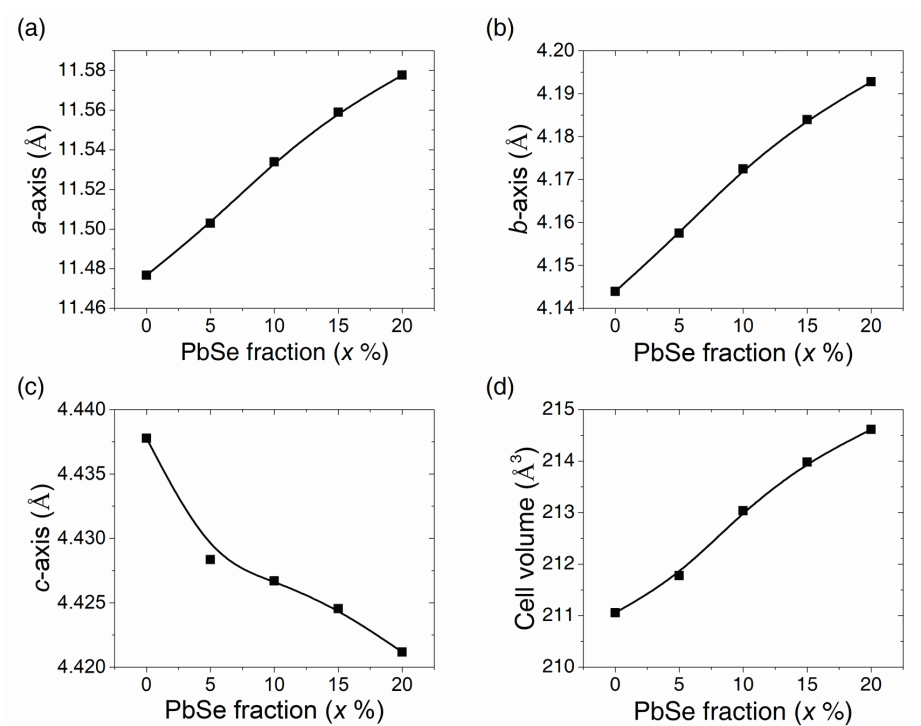


Figure 2. 3. (a-c) The cell dimensions and (d) volume as a function of the fraction of PbSe alloying (x) for the $\text{Sn}_{1.05-x}\text{Pb}_x\text{Sb}_{0.95}\text{Cl}_{0.05}$ sample ($x = 0, 0.05, 0.10, 0.15, 0.20$).

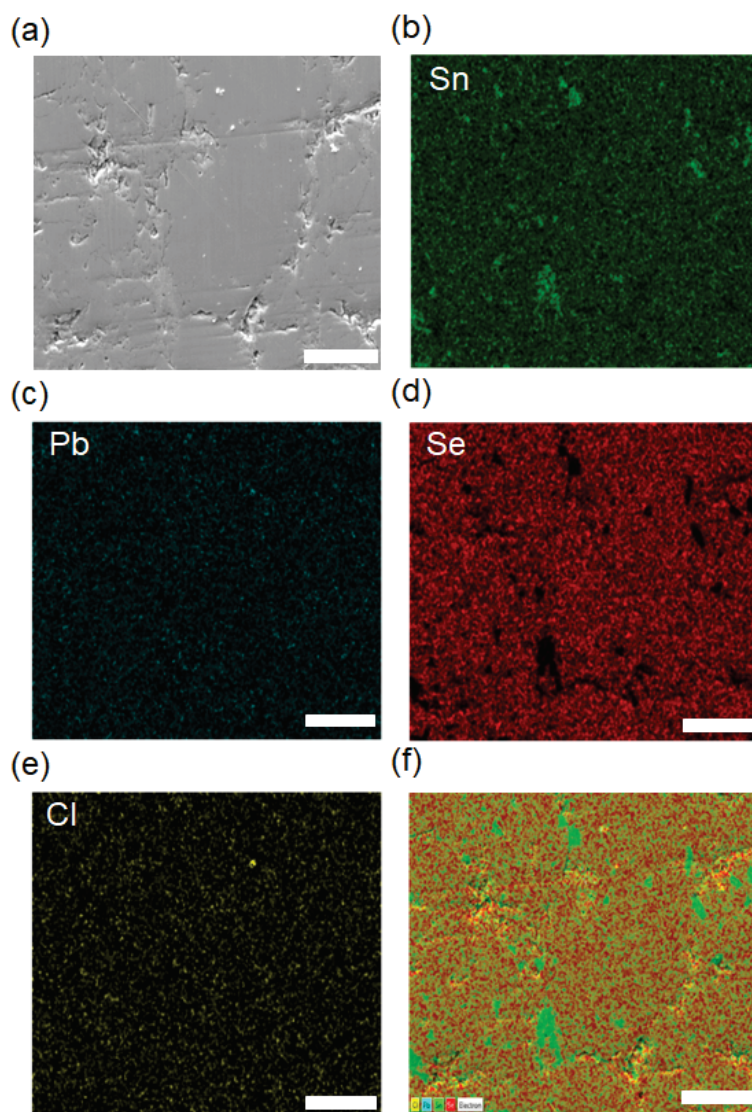


Figure 2. 4. (a) SEM image and (b–e) respective elemental maps of Sn, Pb, Se, and Cl atoms depicted in green, cyan, red, and yellow color by EDS for the melt-synthesized $\text{Sn}_{0.90}\text{Pb}_{0.15}\text{Se}_{0.95}\text{Cl}_{0.05}$ sample. These four elemental maps jointly create the image in (f) showing elemental distribution. Sn precipitate is clearly seen. Scale bar: 10 μm .

2.3.2 TE properties of melt-synthesized $\text{Sn}_{1.05-x}\text{Pb}_x\text{Se}_{0.95}\text{Cl}_{0.05}$

Because of two-dimensional structure of SnSe, TE properties of densified SnSe pellets tend to be highly anisotropic according to the preferred orientation of crystallites. Indeed, n-type SnSe materials are mostly reported to exhibit higher ZT parallel to the press direction,^{36, 40} while the p-type counterparts perpendicular to the press direction.^{30, 31, 34} Hence, we characterize and discuss about TE properties both perpendicular and parallel to the press direction of SPS.

For developing high TE performance n-type SnSe materials, we sequentially synthesized and optimized each family of $\text{SnSe}_{1-y}\text{Cl}_y$ ($y = 0 - 0.08$; the optimal y for ZT_{\max} ($y_{\text{opt}} = 0.05$), $\text{Sn}_{1+z}\text{Se}_{0.95}\text{Cl}_{0.05}$ ($z = 0 - 0.10$; $z_{\text{opt}} = 0.05$), and $\text{Sn}_{1.05-x}\text{Pb}_x\text{Se}_{0.95}\text{Cl}_{0.05}$ ($x = 0 - 0.20$; $x_{\text{opt}} = 0.15$) as noted above. We will focus on TE properties of the optimized compositions of $\text{Sn}_{1.05-x}\text{Pb}_x\text{Se}_{0.95}\text{Cl}_{0.05}$. TE data for the first two systems are given in Supporting Information (Figures 2. 5 and 2. 6).

Figures 2. 7–8 and 2. 9–10 show temperature-dependent TE properties parallel and perpendicular to the SPS direction, respectively, for melt-synthesized and SPS-processed samples. Note that the trends of TE properties along both the directions are similar. The electrical conductivity (σ) increases with the higher fraction of PbSe alloying over the full temperature range (Figure 2. 7a). For example, the σ at room temperature increases from

14 ($x = 0$) to 39 S cm⁻¹ ($x = 0.20$). The effect of PbSe alloying is more obvious for data measured perpendicular to the SPS direction (Figure 2. 9a). Importantly, the Hall effect measurement data confirm that the improved σ by PbSe alloying arises from the simultaneously enhanced carrier concentration (n_H) and mobility (μ_H) by comparison with the results of SnSe_{1-y}Cl_y and Sn_{1+z}Se_{0.95}Cl_{0.05} systems (Figure 2. 11). The n_H at room temperature monotonously rises with the higher amount of PbSe alloying (Table 2. 1) because replacing Sn by Pb suppresses spontaneously evolving Sn vacancies and consequently increases electron concentration. A slight decrease in the σ around 500 K might be related with the presence of Sn precipitate, consistent with the previous report for n-type SnSe doped with BiCl₃.³⁷

The temperature-dependent Seebeck coefficients (S) steadily grow and keep negative values throughout the temperature range of measurements, confirming n-type conduction (Figure 2. 7b). The magnitude of S decreases with the larger amount of PbSe alloying from 373 K to 673 K, as predicted by the trend of the σ and n_H . To investigate the effect of PbSe alloying and Cl doping on S , the theoretical Pisarenko relation between the S and n_H at room temperature for melt-synthesized Sn_{1.05-x}Pb_xSe_{0.95}Cl_{0.05} samples is plotted (Figure 2. 12). It is calculated based on a single parabolic band (SPB) model with an effective mass of $\sim 0.45 m_e$. Acoustic phonon scattering is assumed as the main carrier scattering mechanism (see Supporting Information for the

details). The experimental S for $\text{Sn}_{1.05-x}\text{Pb}_x\text{Se}_{0.95}\text{Cl}_{0.05}$ samples falls well on the Pisarenko line, indicating neither PbSe alloying nor Cl doping changes the electronic structure of SnSe. The sample with $x = 0.20$ shows the highest power factor (PF) of ~ 6.38 and $\sim 6.84 \mu\text{W cm}^{-1} \text{K}^{-2}$ parallel (Figure 2.7c) and perpendicular (Figure 2.9c) to the SPS direction, respectively, which is more than 40% improvement from that of $\text{Sn}_{1.05}\text{Se}_{0.95}\text{Cl}_{0.05}$ with no PbSe alloying.

PbSe alloying substantially reduces the total (κ_{tot}) and lattice thermal conductivities (κ_{lat}) especially near ambient temperature possibly due to the induced point defects (Figures 2.8a and b). For example, the κ_{tot} at room temperature significantly reduces from $\sim 1.06 \text{ W m}^{-1} \text{K}^{-1}$ for $\text{Sn}_{1.05}\text{Se}_{0.95}\text{Cl}_{0.05}$ to $\sim 0.64 \text{ W m}^{-1} \text{K}^{-1}$ for $\text{Sn}_{0.90}\text{Pb}_{0.15}\text{Se}_{0.95}\text{Cl}_{0.05}$. Though the κ_{tot} for PbSe-alloyed samples generally decreases with rising temperature, there are two slight upturn points at ~ 473 and 773 K . The first upturn is plausibly related with the presence of elemental Sn precipitate as observed in the σ . The second one may result from bipolar diffusion.³⁰ Comparison of the κ_{tot} and κ_{lat} reveals that heat-carrying phonon transport mainly contributes to the κ_{tot} for all samples. The κ_{tot} and κ_{lat} decrease with PbSe alloying up to $x = 0.15$ because of better phonon scattering by point defects at the atomic level. However, this trend is unobvious above $\sim 623 \text{ K}$, and is not observed in κ_{tot} and κ_{lat} taken perpendicular to the SPS direction (Figures 2.10a – b). They slightly increase

for the sample with $x = 0.20$ probably due to isolated elemental Pb with high thermal conductivity as shown in the PXRD result. Both the κ_{tot} and κ_{lat} are lower along the parallel direction of SPS. For example, the κ_{lat} value of $\text{Sn}_{0.90}\text{Pb}_{0.15}\text{Se}_{0.95}\text{Cl}_{0.05}$ is ~ 0.38 and $\sim 0.63 \text{ W m}^{-1} \text{ K}^{-1}$ at 823 K parallel and perpendicular to the SPS direction, respectively.

It is unusual that PbSe alloying concurrently improves n_{H} and μ_{H} , leading to the increased σ for n-type $\text{Sn}_{1.05-x}\text{Pb}_x\text{Se}_{0.95}\text{Cl}_{0.05}$ samples. Note that, on the contrary, PbSe alloying on p-type SnSe systems reduces n_{H} and μ_{H} simultaneously, ultimately degrading electrical transport properties.³⁰ Resultantly enhanced PF and reduced κ_{lat} synergistically contribute to a considerably improved $ZT \sim 1.1$ parallel to the SPS direction for the samples with $x = 0.15$ and 0.20 in comparison with ~ 0.8 for $\text{SnSe}_{0.95}\text{Cl}_{0.05}$ with no PbSe alloying (Figures 2. 8c and 2. 10c). The melt-synthesized sample exhibits larger ZT parallel to the SPS direction because of the greater decrease in κ_{lat} (Figures 2. 8 and 2. 10).

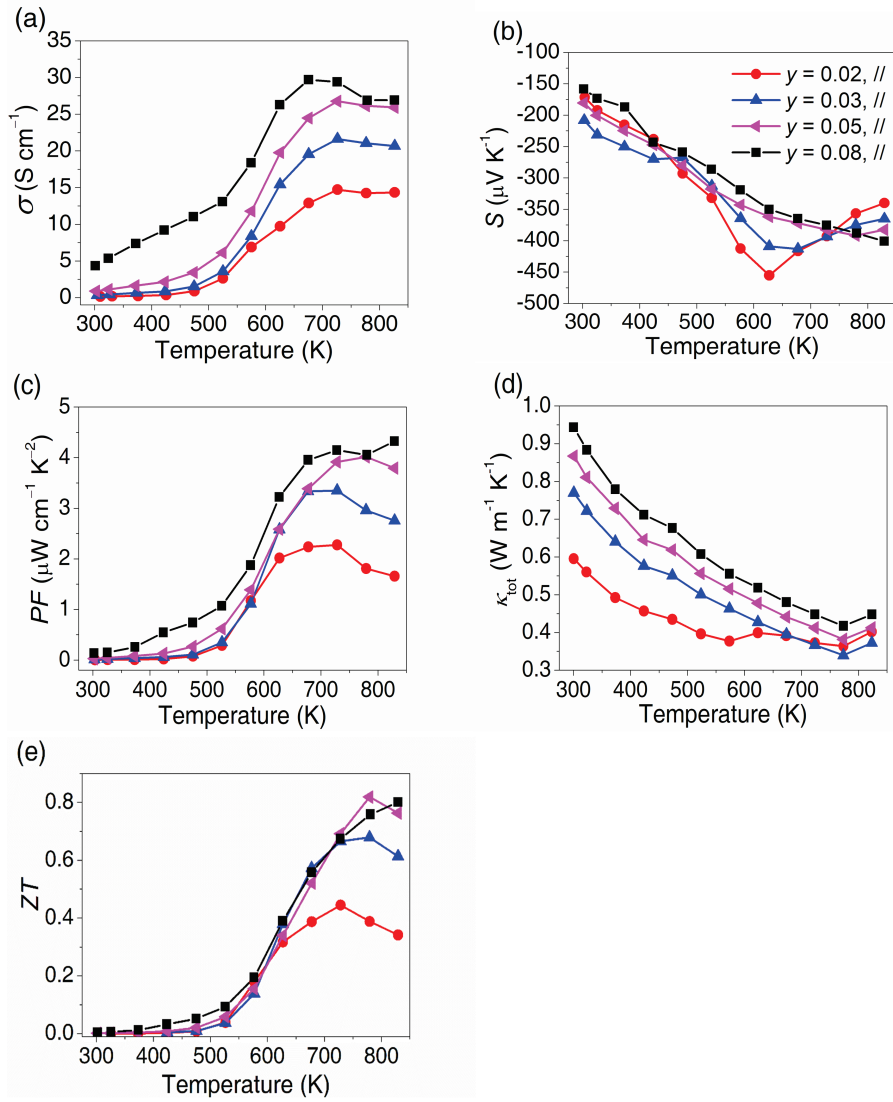


Figure 2. 5. Temperature dependence of (a) electrical conductivity, (b) Seebeck coefficient, (c) power factor, (d) total thermal conductivity, and (e) ZT for the melt-synthesized $\text{SnSe}_{1-y}\text{Cl}_y$ ($y = 0.02, 0.03, 0.05, \text{ and } 0.08$) samples measured parallel to the SPS direction.

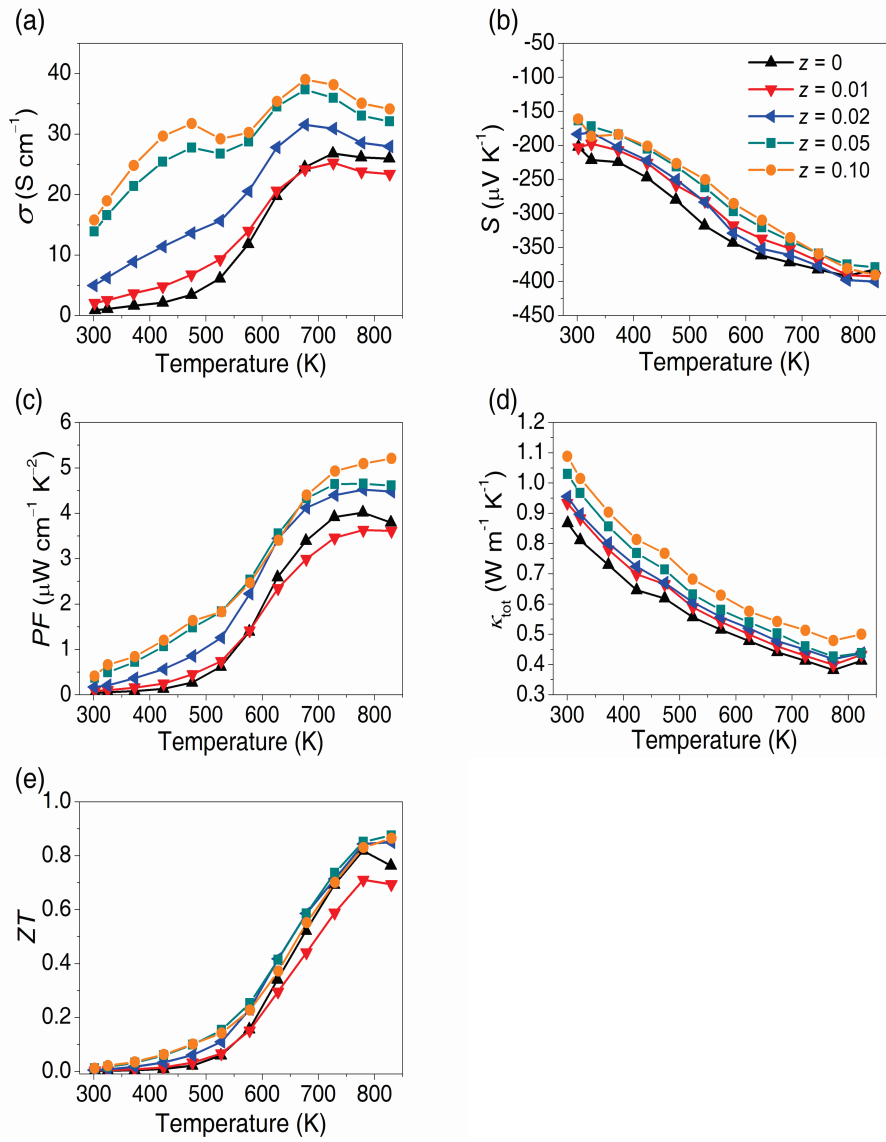


Figure 2. 6. Temperature dependence of (a) electrical conductivity, (b) Seebeck coefficient, (c) power factor, (d) total thermal conductivity, and (e) ZT for the melt-synthesized $\text{Sn}_{1+z}\text{Se}_{0.95}\text{Cl}_{0.05}$ ($z = 0, 0.01, 0.02, 0.05, \text{ and } 0.10$) samples measured parallel to the SPS direction.

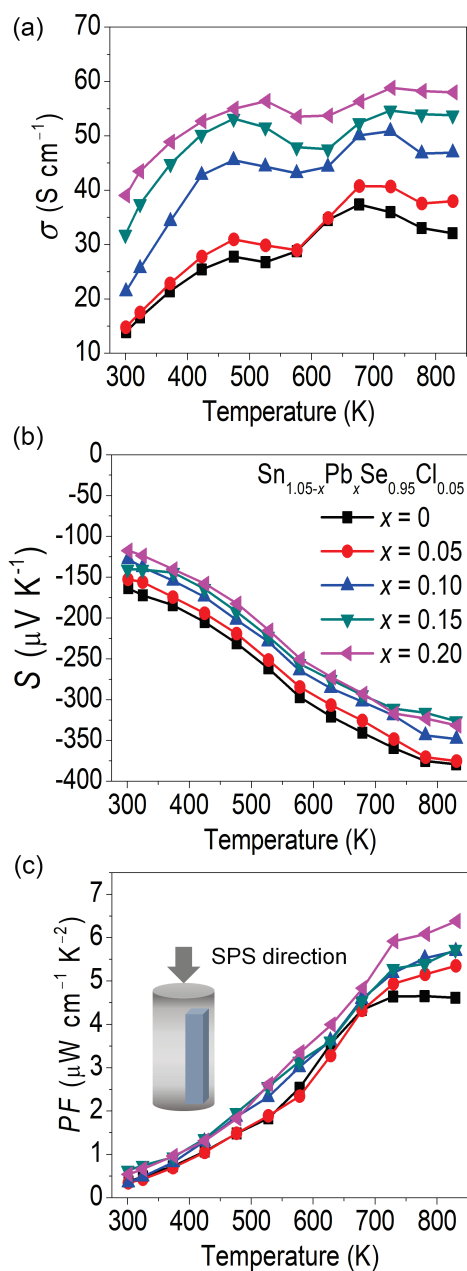


Figure 2. 7. Temperature dependence of (a) electrical conductivity, (b) Seebeck coefficient, and (c) power factor for the melt-synthesized $\text{Sn}_{1.05-x}\text{Pb}_x\text{Se}_{0.95}\text{Cl}_{0.05}$ samples measured parallel to the SPS direction.

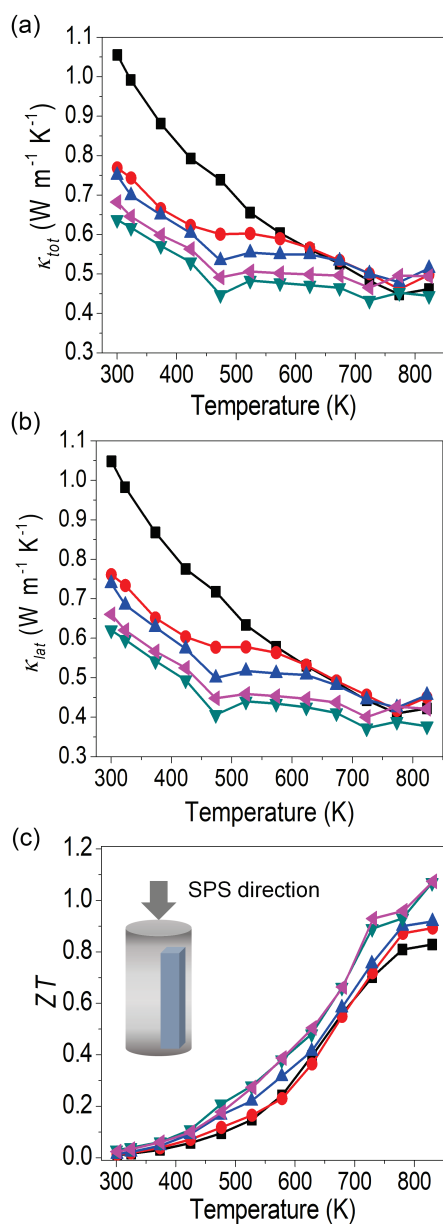


Figure 2. 8. Temperature dependence of (a) total and (b) lattice thermal conductivity, and (c) thermoelectric figure of merit ZT for the melt-synthesized $\text{Sn}_{1.05-x}\text{Pb}_x\text{Se}_{0.95}\text{Cl}_{0.05}$ samples measured parallel to the SPS direction.

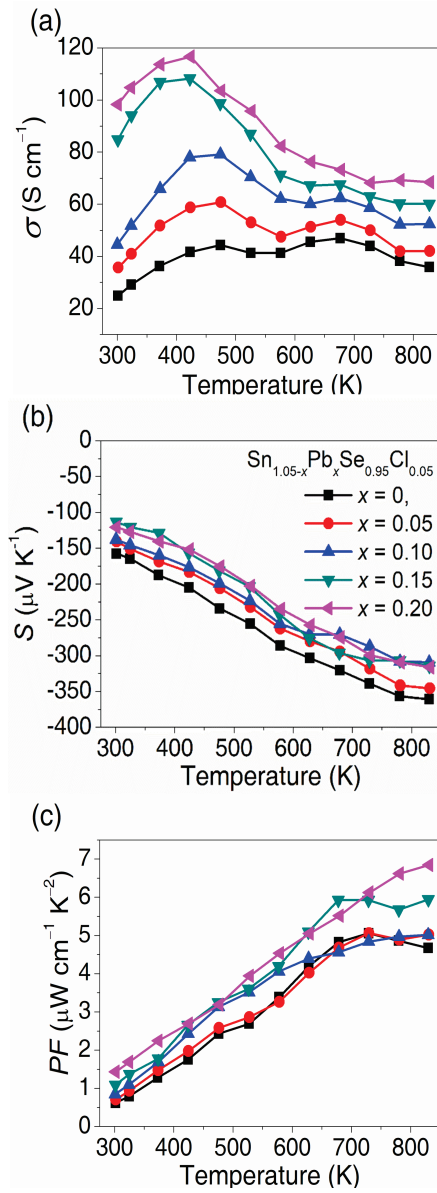


Figure 2. 9. Temperature dependence of (a) electrical conductivity, (b) Seebeck coefficient, and (c) power factor for the melt-synthesized $\text{Sn}_{1.05-x}\text{Pb}_x\text{Se}_{0.95}\text{Cl}_{0.05}$ ($x = 0, 0.05, 0.10, 0.15,$ and 0.20) samples measured perpendicular to the SPS direction.

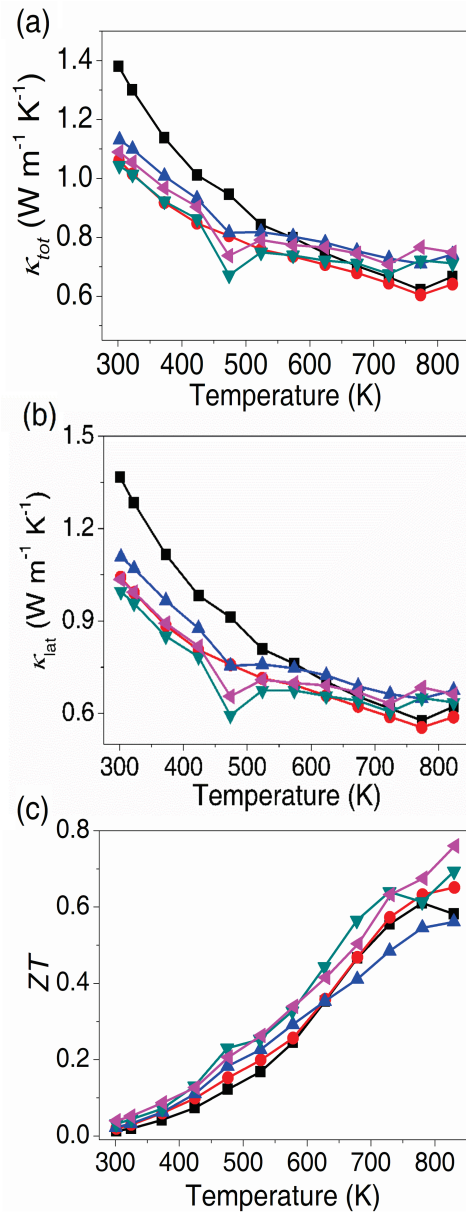


Figure 2. 10. Temperature dependence of (a) total and (b) lattice thermal conductivity, and (c) ZT for the melt-synthesized $\text{Sn}_{1.05-x}\text{Pb}_x\text{Se}_{0.95}\text{Cl}_{0.05}$ ($x=0, 0.05, 0.10, 0.15,$ and 0.20) samples measured perpendicular to the SPS direction.

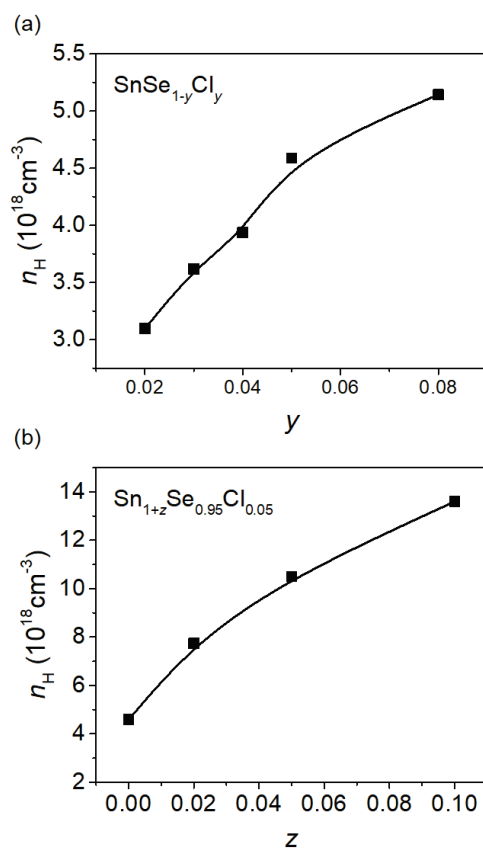


Figure 2. 11. Carrier concentration at room temperature as a function of the extent of (a) Cl doping (y) for $\text{SnSe}_{1-y}\text{Se}_y$ ($y = 0 - 0.08$) and (b) excess Sn (z) for $\text{Sn}_{1+z}\text{Se}_{0.95}\text{Cl}_{0.05}$ ($z = 0 - 0.10$).

PbSe alloying fraction	n_H (10^{19} cm^{-3})	μ_H ($\text{cm}^2 \text{ V}^{-1} \text{ S}^{-1}$)	Density (g cm^{-3})
$x = 0.00$	1.05	8.26	5.93
$x = 0.05$	1.18	7.82	6.09
$x = 0.10$	1.23	10.85	6.16
$x = 0.15$	1.84	10.81	6.24
$x = 0.20$	1.96	12.45	6.37

Table 2. 1. Variation in carrier concentration (n_H), mobility (μ_H), and apparent density at room temperature according to the fraction of PbSe alloying (x) for the melt-synthesized (MS) $\text{Sn}_{1.05-x}\text{Pb}_x\text{Se}_{0.95}\text{Cl}_{0.05}$ sample, measured parallel to the press direction of spark plasma sintering (SPS). The n_H and μ_H values were obtained by the Hall effect measurement.

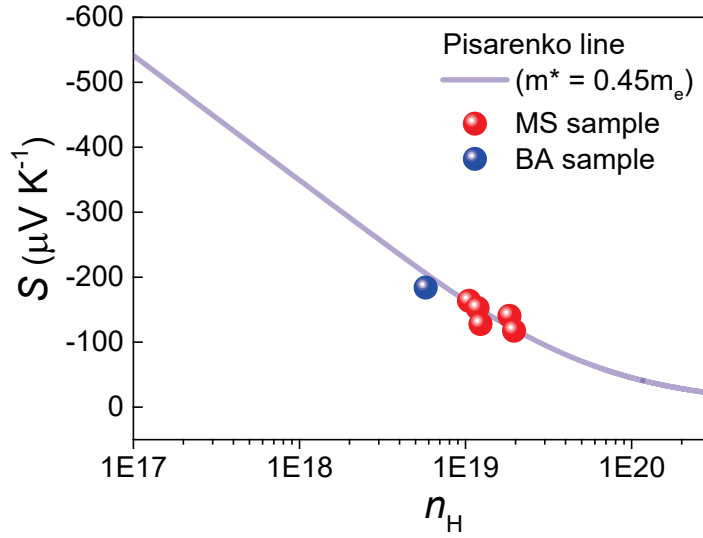


Figure 2. 12. Experimental Seebeck coefficient (S) as a function of carrier concentration (n_H) with the theoretical Pisarenko line based on a single parabolic band model at room temperature. The experimental S of the MS and BA samples falls well on the Pisarenko line, indicating electronic structure of SnSe is not changed by PbSe alloying, Cl doping, and ball-mill and annealing process.

2.3.3 Reducing intrinsic structural anisotropy and enhancing TE properties

We observed strong anisotropy in TE properties of melt-synthesized (MS) SPS samples. This feature is undesirable for facile processibility in producing TE legs for module fabrication. We devised a two-step process to address such an intrinsic problem of low-dimensional materials. MS bulk powder of $\text{Sn}_{0.90}\text{Pb}_{0.15}\text{Se}_{0.95}\text{Cl}_{0.05}$ is ball-milled and subsequently annealed under an Ar atmosphere. The former step can reduce the size and structural anisotropy of powders. The latter step can recover crystallinity and heal surface defects possibly brought by the former process.

Figure 2. 13 represents the PXRD pattern of the ball-milled and annealed (BA) sample of $\text{Sn}_{0.90}\text{Pb}_{0.15}\text{Se}_{0.95}\text{Cl}_{0.05}$ in comparison with those of the MS sample and theoretical simulation. While both samples contain a trace of elemental Sn, they show the considerably different preferred orientation with each other. To better understand the correlation between the degree of structural anisotropy and TE properties, the dense pellets used for TE property measurements were reground to a fine powder for the PXRD. Because SnSe layers propagate along the yz plane, the (400) Bragg reflection peak tends to be more intense than the (111) due to the preferred orientation as observed in the MS sample (Figures 2. 2 and 2. 13). In striking contrast, the BA sample demonstrates the stronger (111) than the (400) reflection peak, similar to the

theoretical simulation. This observation indicates the reduced structural anisotropy in the BA sample.

The degree of preferred orientation is commonly quantified using the Lotgering factor⁴⁴ defined by equations 1 – 3:

$$LF = \frac{P - P_0}{1 - P_0} \quad (1)$$

$$P = \frac{\sum I(h00)}{\sum I(hkl)} \quad (2)$$

$$P_0 = \frac{\sum I_0(h00)}{\sum I_0(hkl)} \quad (3)$$

where P and P_0 are the proportion of orientation for a preferred and a random orientation, respectively, and $\sum I(h00)$ and $\sum I(hkl)$ are the integration of peak intensities for the $(h00)$ and (hkl) diffractions in the 2θ range from 10° to 60° , respectively. The theoretical diffraction pattern of SnSe (JCPDS # 48-1224) is used as a reference. The BA powder sample shows the lower LF of 0.24 than 0.36 of the MS powder sample, indicating the reduced preferred orientation along the $(h00)$ direction for their roughly packed crystallites. To confirm this, we cut and polished the pellets perpendicular and parallel to the SPS direction and took their XRD patterns (Figure 2. 14). The SPS BA sample shows the almost same $LF \sim 0.31$ along both the directions. In contrast, the SPS MS sample gives a LF of 0.42 and 0.16 perpendicular and parallel to the

SPS direction, respectively, consistent with the previous reports for pristine, Ag and Ge doped SnSe.⁴⁵⁻⁴⁷ The reduced structural anisotropy of the SPS BA sample is clearly reflected on its TE properties as discussed below.

According to typical SEM image and the corresponding elemental maps by EDS taken on the polished surface of the SPS-processed BA sample, Sn precipitate is apparently invisible within the detection limit of SEM-EDS (Figure 2. 15) in contrast to the result for the MS sample (Figure 2. 4). Note that it is detected for both the MS and BA samples by the PXRD. These observations suggest that isolated Sn would be better pulverized and distributed homogeneously by a ball mill process.

Afterward, we characterized TE properties of the BA sample of $\text{Sn}_{0.90}\text{Pb}_{0.15}\text{Se}_{0.95}\text{Cl}_{0.05}$ perpendicular and parallel to the SPS direction (Figure 2. 16–17). The σ monotonously increases over the entire range of temperature, showing typical semiconducting behavior in contrast to that of the corresponding MS sample (Figure 2. 16a). Note that the σ values are considerably decreased by the BA process. For example, the σ is merely 3.5 S cm^{-1} at room temperature in comparison with 85 S cm^{-1} of the MS sample. This huge difference can be explained by simultaneous deterioration in the n_{H} and μ_{H} by a ball mill process (Table 2. 2). The magnitude of temperature-dependent Seebeck coefficient (S) increases with temperature from room temperature to 723 K and slightly decreases afterward (Figure 2. 16b). The S

value of BA sample at room temperature fits well on the theoretical Pisarenko line based on a SPB model with an effective mass of $\sim 0.45 m_e$, similar to the case of the MS sample (Figure 2. 12). It indicates that BA process does not change the main scattering mechanism and the electronic structure of SnSe. The trend of the S as a function of temperature is similar for the MS and BA samples, and the values are larger for the latter. The maximum value (S_{\max}) is $-373 \mu\text{V K}^{-1}$ at 723 K, larger than $-314 \mu\text{V K}^{-1}$ at 823 K of the MS sample. This enhancement results in the improved PF of the BA sample above 723 K over the MS sample and a maximum value reaches $\sim 6.74 \mu\text{W cm}^{-1} \text{K}^{-2}$ at 823 K (Figure 2. 16c). To elucidate the improvement by the BA process, we conducted the temperature-dependent Hall effect measurement for both the MS and BA samples along the perpendicular to the SPS direction (Figure 2. 18). Their n_H and μ_H show a significantly different trend as observed in their σ . The n_H of the BA sample increases with rising temperature in contrast to that of the MA sample, consequently exceeding the values of the latter above 473 K. This observation is plausibly related with homogeneously distributed Sn precipitates embedded in the BA sample as observed in the SEM studies. On the other hand, the BA process substantially reduces μ_H over the entire range of temperature. This probably results from considerably reduced grain sizes by ball milling. Resultant grain boundaries can increase carrier scattering at the interfaces.

Figures 2. 17a and b clearly demonstrate that the thermal conductivity (κ) is markedly reduced by the BA process. For example, the total κ (κ_{tot}) perpendicular to the SPS direction is $\sim 0.71 \text{ W m}^{-1} \text{ K}^{-1}$ at room temperature, 32% lower than that of the MS sample. Remarkably, both κ_{tot} and lattice κ (κ_{lat}) of the BA sample perpendicular to the SPS direction are comparable to those of the MS sample parallel to the SPS direction. It is surprising in that layered structure of SnSe should give much lower κ along the out-of-plane direction and an SPS process typically provides highly ordered pellets. Importantly, the difference in κ 's between each direction for the BA sample is marginal, indicating surprisingly weakened anisotropy in TE properties, in sharp contrast to the large difference in the MS sample. This observation is consistent with their calculated LF s. The marked reduction in the κ_{lat} coupled with the enhanced PF above 673 K enables a $ZT_{\text{max}} \sim 1.2$ at 823 K perpendicular to the SPS direction (Figure 2. 17c). It is important to note that the BA sample exhibits $ZT_{\text{max}} \sim 1.2$ along both the directions in contrast to the substantially anisotropic ZT in single crystal and typical polycrystalline SnSe samples.

The reproducibility and reversibility of charge and thermal transport properties are of pivotal importance in practical applications of TE materials. We prepared and characterized the BA samples of $\text{Sn}_{0.90}\text{Pb}_{0.15}\text{Se}_{0.95}\text{Cl}_{0.05}$ from

the three independent synthesis batches. Their essential TE parameters of σ , S , κ_{tot} , and consequent ZT are highly reproducible (Figure 2. 19). Those parameters are also excellently reproducible during multiple heating cycles with the negligible deviation upon heating and cooling cycles within the range of instrumental errors (Figure 2. 20). Differential thermal analysis (DTA) and PXRD studies before and after DTA demonstrate that no undesirable chemical decomposition occurs during the thermal cycles (Figure 2. 21). These results verify the high reversibility and reproducibility of TE performances as well as the thermal and chemical robustness of this material.

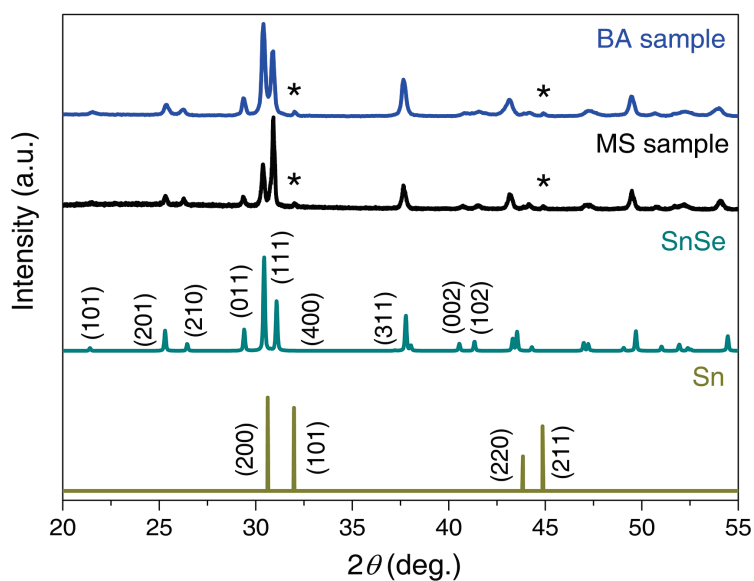


Figure 2. 13. XRD patterns of the melt-synthesized (MS) and further ball-milled and annealed (BA) powder samples of $\text{Sn}_{0.90}\text{Pb}_{0.15}\text{Se}_{0.95}\text{Cl}_{0.05}$ in comparison with the simulated patterns of SnSe (PDF 48-1224) and Sn (PDF 86-2264). Sn Bragg peaks are denoted by asterisks.

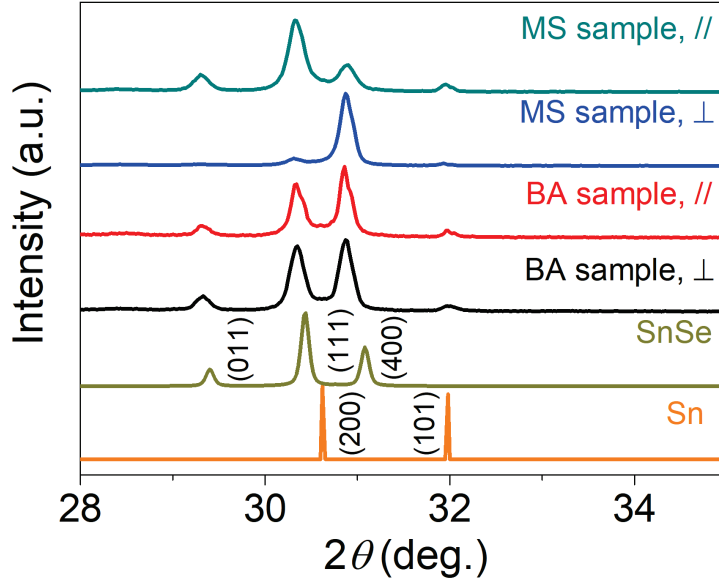


Figure 2. 14. XRD patterns of the SPS processed BA and the MS samples with the composition $\text{Sn}_{0.90}\text{Pb}_{0.15}\text{Se}_{0.95}\text{Cl}_{0.05}$ measured perpendicular (\perp) and parallel (\parallel) to the press direction in comparison with the theoretically simulated patterns of SnSe (PDF 48-1224) and Sn (PDF 86-2264). Major Bragg peaks are indexed.

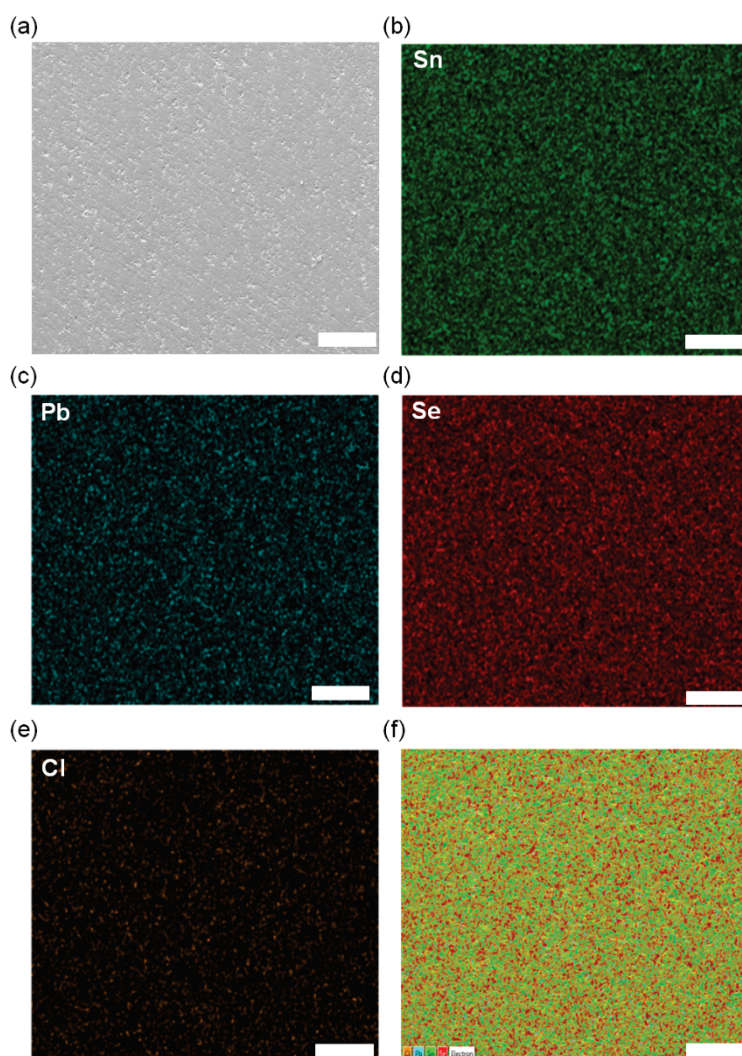


Figure 2. 15. (a) SEM image and (b–e) respective elemental maps of Sn, Pb, Se, and Cl atoms displayed in green, cyan, red, and orange color by EDS for the BA $\text{Sn}_{0.90}\text{Pb}_{0.15}\text{Se}_{0.95}\text{Cl}_{0.05}$ sample. These four panels jointly create the image in (f) showing elemental distribution. Scale bar: 50 μm.

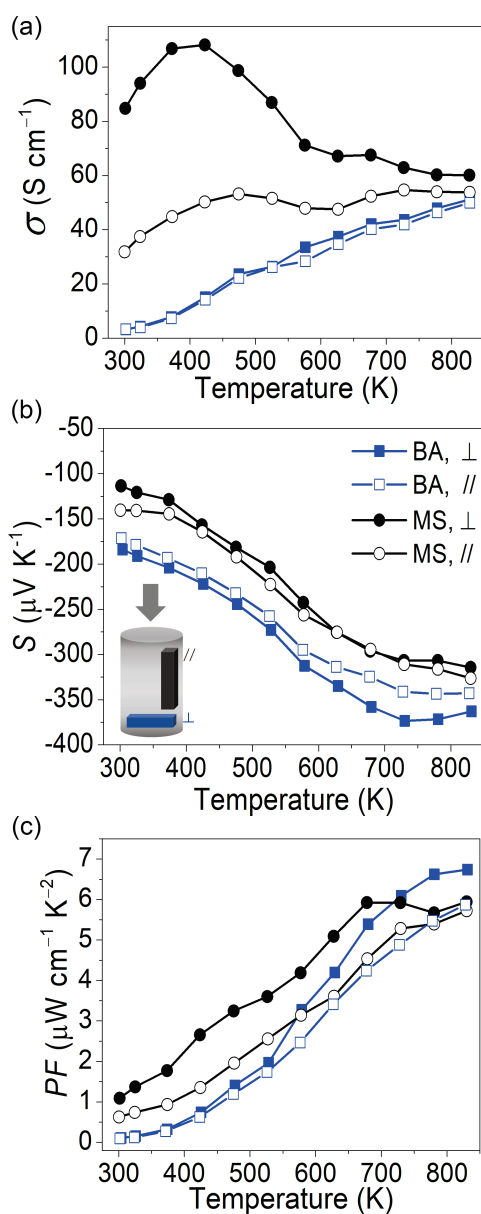


Figure 2. 16. Temperature dependence of (a) electrical conductivity, (b) Seebeck coefficient, and (c) power factor for the BA and MS $\text{Sn}_{0.90}\text{Pb}_{0.15}\text{Se}_{0.95}\text{Cl}_{0.05}$ samples measured perpendicular (\perp) and parallel (\parallel) to the press direction of SPS. Note that the BA sample exhibits a comparable ZT along both the directions.

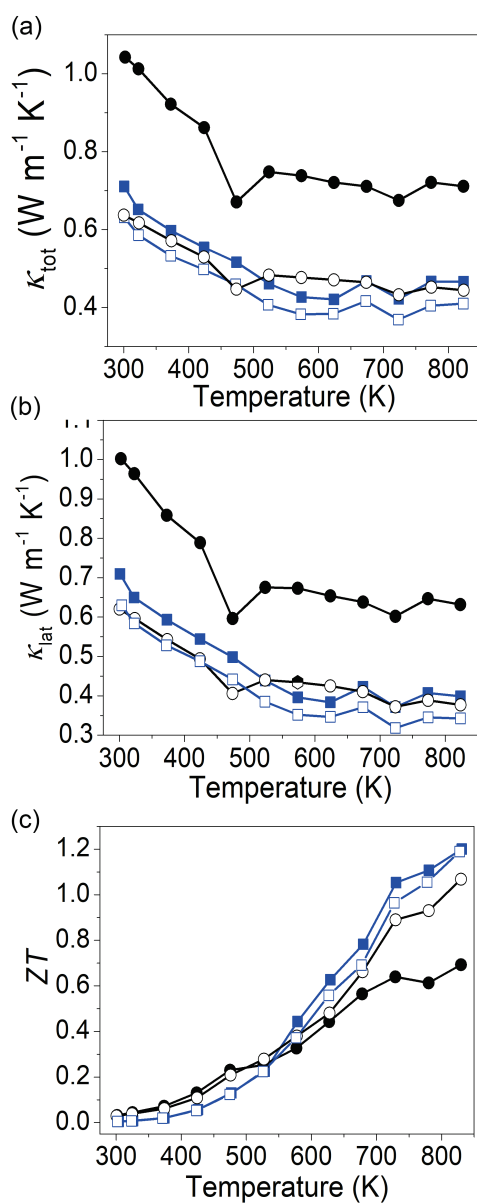


Figure 2. 17. Temperature dependence of (a) total thermal conductivity, (b) lattice thermal conductivity, and (c) ZT for the BA and MS $\text{Sn}_{0.90}\text{Pb}_{0.15}\text{Se}_{0.95}\text{Cl}_{0.05}$ samples measured perpendicular (\perp) and parallel (\parallel) to the press direction of SPS. Note that the BA sample exhibits a comparable ZT along both the directions.

	Carrier concentration (10^{18} cm^{-3})	Mobility ($\text{cm}^2 \text{ V}^{-1} \text{ S}^{-1}$)	Density (g cm^{-3})
MS sample (parallel)	18.4	10.81	6.24
MS sample (perpendicular)	1.72	30.80	
BA sample (parallel)	5.76	3.02	6.07
BA sample (perpendicular)	0.61	3.26	

Table 2. 2. Comparison of carrier concentration (n_H), mobility (μ_H), and apparent density at room temperature between the ball milled and annealed (BA) and the MS samples. The n_H and μ_H values were obtained by the Hall effect measurement. The measurement direction with respect to the SPS press direction is noted.

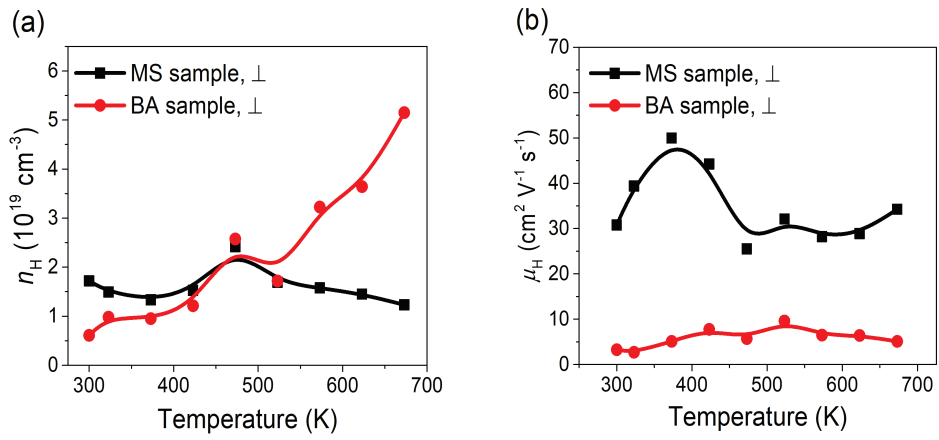


Figure 2. 18. Hall effect measurements for (a) Carrier concentration (n_H) and (b) mobility (μ_H) of the MS and BA samples with the composition $\text{Sn}_{0.90}\text{Pb}_{0.15}\text{Se}_{0.95}\text{Cl}_{0.05}$ perpendicular to the SPS press direction as a function of temperature.

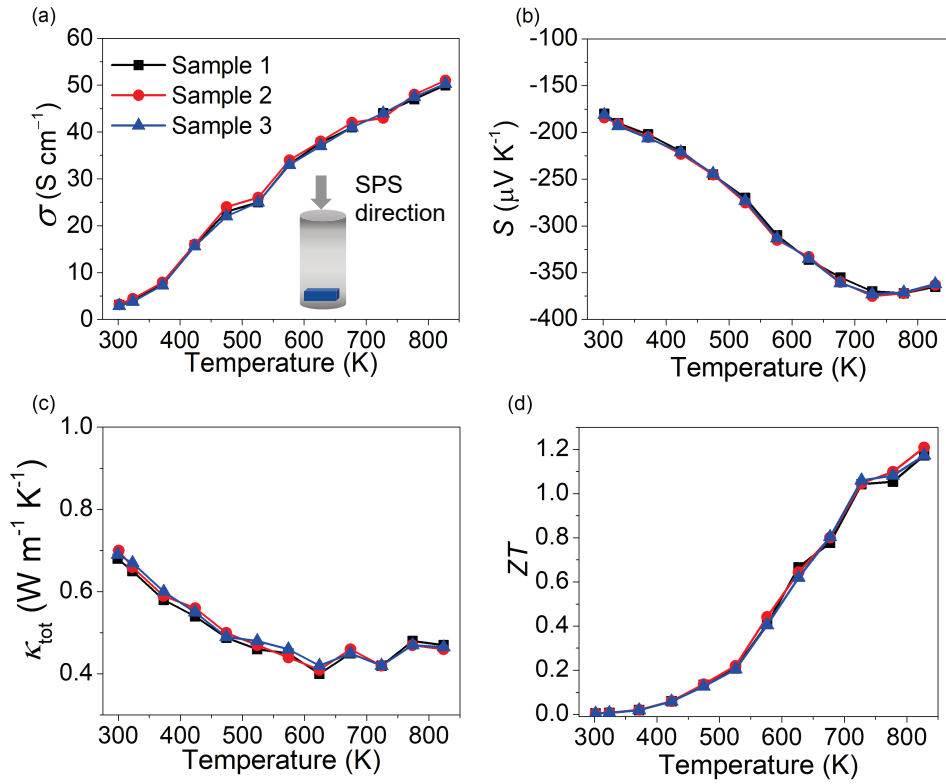


Figure 2. 19. Temperature-dependent (a) electrical conductivity, (b) Seebeck coefficient, (c) total thermal conductivity, and (d) ZT for the BA $\text{Sn}_{0.90}\text{Pb}_{0.15}\text{Se}_{0.95}\text{Cl}_{0.05}$ samples. Three samples were independently prepared and characterized. These results indicate the excellent reproducibility of thermoelectric properties of BA samples.

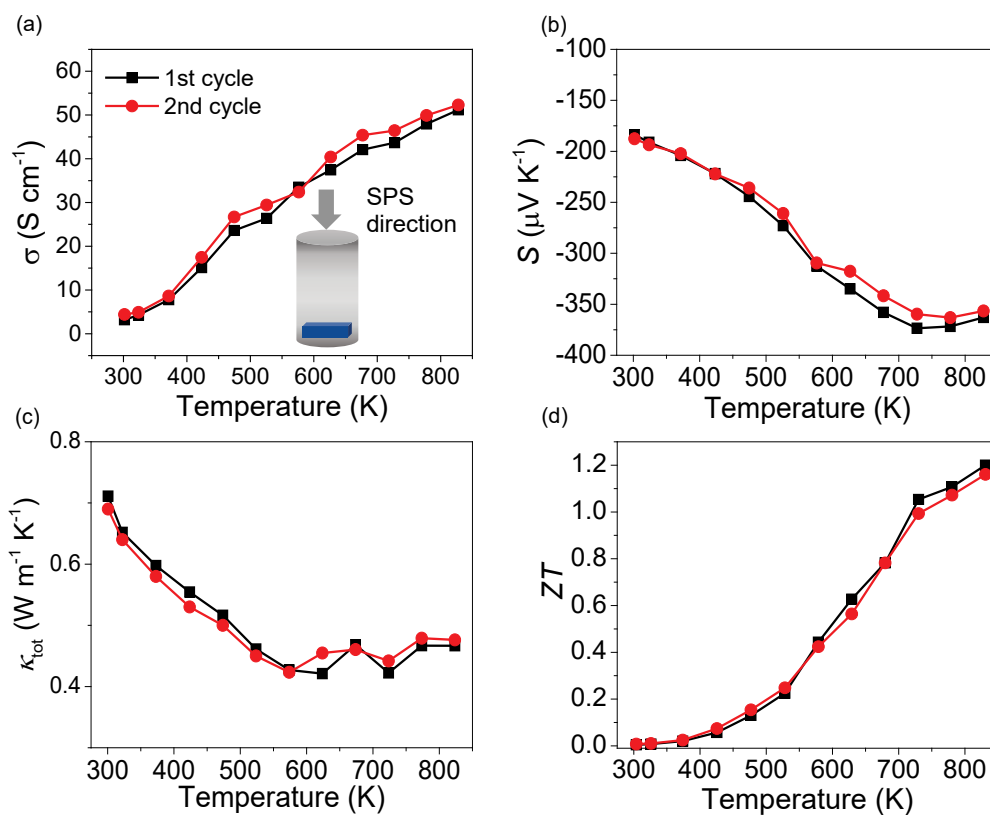


Figure 2. 20. Temperature-dependent (a) electrical conductivity, (b) Seebeck coefficient, (c) thermal conductivity and (d) ZT for the BA $\text{Sn}_{0.90}\text{Pb}_{0.15}\text{Se}_{0.95}\text{Cl}_{0.05}$ sample during multiple heating cycles, demonstrating the high repeatability of TE properties as well as the thermal and chemical stability of this material.

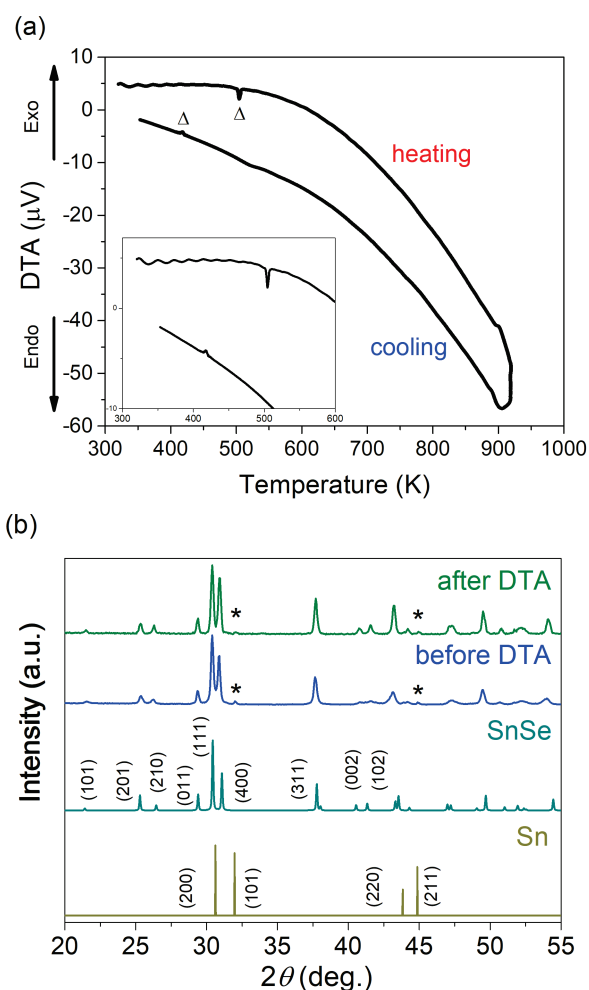


Figure 2. 21. (a) Differential thermal analysis (DTA) diagram of the BA $\text{Sn}_{0.90}\text{Pb}_{0.15}\text{Se}_{0.95}\text{Cl}_{0.05}$ sample at a rate of 10 K min^{-1} . Exo- and endothermic peaks (Δ) can be assigned to melting and recrystallization of Sn considering the melting point of Sn at $\sim 505 \text{ K}$.⁽¹⁾ The region for such thermal events is enlarged in the inset. (b) X-ray powder diffraction patterns for the $\text{Sn}_{0.90}\text{Pb}_{0.15}\text{Se}_{0.95}\text{Cl}_{0.05}$ BM sample before and after the DTA cycle. No discernible change is observed after DTA. The Bragg peaks from elemental Sn are indicated by the asterisk mark (*), which is due to excess Sn in the composition. The theoretically simulated patterns of SnSe (PDF 48-1224) and elemental Sn (PDF 86-2264) are given for comparison. Major peaks are indexed.

2.3.4 Nanostructures

Electrical and thermal transport properties are highly sensitive to nanostructures such as disorders, dislocations, and defects embedded in bulk TE materials.^{19, 24} Recently, we reported the unusual TE properties of $K_{0.06}Bi_2T_{3.18}$ and 1% Na doped $Sn_{1-x}Pb_xSe$ materials employing atomic resolution spherical aberration-corrected scanning transmission electron microscope (Cs-corrected STEM).^{16, 30} For the former, we were able to locate the exact positions of excess potassium and tellurium atoms in crystal structure and accordingly elucidate their unusual role as an electron donor and the highest n-type TE performance for Bi_2Te_3 -based materials operating near ambient temperature. For the latter, we found that $Sn_{1-x}Pb_xSe$ alloys spontaneously form a substantial amount of nanostructures with compositional fluctuations rather than solid solutions as mistakenly reported in the published phase diagram⁴⁸ and literatures.^{49, 50} Such nanostructures are embedded in the matrix with highly coherent interfaces, thereby suppressing lattice thermal conductivity with a minimal damage in electrical conductivity.³⁰

On those accounts, we investigated nanostructures for the SPS-processed sample of MS $Sn_{0.90}Pb_{0.15}Se_{0.95}Cl_{0.05}$ using a Cs-STEM equipped with an EDS detector. Typical cross-sectional bright-field (BF) STEM images demonstrate the presence of a substantial degree of dislocations and wrinkled

regions with an alternating contrast (Figures 2. 22a and 23). These morphologies are widely distributed throughout the specimens. They are related with an artificial moiré contrast that results from the interference between the scanning grating and crystalline periodicity in the specimens.⁵¹ We also performed elemental analysis across the regions showing the moiré contrasts by STEM-EDS to probe compositional fluctuation. We did not observe isolated precipitates of specific elements and chemical species, validating artificial moiré contrasts (Figure 2. 24).

Typical medium-magnification cross-sectional high-angle annular dark-field (HAADF) STEM image viewed down the [201] zone axis is shown in Figure 2. 22b. The corresponding fast Fourier transform (FFT) image is indexed as SnSe structure and does not show the evidence of second phase precipitates (inset, Figure 2. 22b). The inverse FFT (IFFT) image of the $(12\bar{2})$ atomic planes, taken at the red rectangular area in Figure 2. 22b, clearly reveals heavily dense edge dislocations marked by the red symbols in Figure 2. 22c. Their average density is statistically calculated to be $\sim 6 \times 10^{13} \text{ cm}^{-2}$ (Figure 2. 25), which is an order of magnitude higher than those of other TE materials containing dense dislocations such as Mg_2Si , PbTe , and PbSe -based materials.⁵²⁻⁵⁵ It is highly probable that the formation of dense dislocations is driven by the introduction of highly ionic Cl^- anion into SnSe

covalent networks, as similarly observed in n-type SnSe doped with halogens.³⁸ Na doped SnSe single crystals also show such dislocations.³² In addition, off-stoichiometric cation-rich composition of $\text{Sn}_{1.05-x}\text{Pb}_x\text{Se}_{0.95}\text{Cl}_{0.05}$ and high PbSe alloying content can also contribute to the evolution of dense dislocations.

Despite intact SnSe structure, typical high-magnification cross-sectional HAADF-STEM image down the [201] direction clearly displays a discernible brightness contrast outlined by the dotted lines (Figure 2. 26a and inset). The IFFT image of the (010) atomic planes shows tortuous lines with a sharp contrast in brightness and edge dislocations inside them (Figure 2. 26b), which is consistent with the observation in Figure 2. 26a.

Because structural imperfectness is frequently accompanied by lattice strains, high quality HAADF-STEM images were processed by geometric phase analysis (GPA) to examine strain variations at and near dislocations. Note that GPA is a semi-quantitative process of TEM images to give spatially distributed strain fields.^{56, 57} Figures 2. 26c and d provide the results of GPA along the x - (ϵ_{xx}) and y -axis (ϵ_{yy}), respectively, for the lattice image shown in Figure 2. 26a. The sharp change in a contrast observed in the strain maps indicates high strain concentrations near the dislocation core. The profile of both the ϵ_{xx} and ϵ_{yy} strain maps shows several plastic strain lines, which is consistent with HAADF-STEM and IFFT images in Figures 2. 26a and b.

Atomic-scale defects and randomly distributed dislocations combined with local strains can be effective scattering centers for high- and mid-frequency phonons, which can reduce κ_{lat} significantly. To affirm our discussion on the structural defects mentioned above, we also analyzed the same area but down the different zone axis of the [123] by HAADF-STEM, and observed the similar results (Figure 2. 27).

The magnified cross-sectional HAADF-STEM image taken along the [123] zone axis clearly demonstrates crystal structure of $\text{Sn}_{0.90}\text{Pb}_{0.15}\text{Se}_{0.95}\text{Cl}_{0.05}$ (Figure 2. 27). To directly identify the constituent elements in the structure, we performed atomic resolution elemental mapping on the selected area marked by the red rectangle in Figure 2. 28a employing STEM-EDS. The respective EDS signal from Sn, Pb, Se, and Cl atoms is depicted in green, cyan, red, and orange colors, respectively, in Figures 2. 28b – e, subsequently assembled to create the image in Figure 2. 28f. It reveals Sn and Pb atoms occupy the same atomic sites with a totally disordered fashion while Se atom is confirmed to take their unique crystallographic positions. However, the location of Cl atom is relatively less resolved plausibly because of its intrinsic sensitivity to prolonged exposure to strong and focused electron irradiation.

The HAADF-STEM and EDS analyses coupled with GPA in this work

disclose that introducing Pb and Cl atoms to SnSe structure induces a distinctive defective structural feature, namely, a considerable degree of point defects, dislocations, and lattice strains. Their incorporation effectively suppresses heat-carrying phonon transfer and contributes to a high ZT value of n-type $\text{Sn}_{0.90}\text{Pb}_{0.15}\text{Se}_{0.95}\text{Cl}_{0.05}$.

After observing various types of high density nanostructures in $\text{Sn}_{0.90}\text{Pb}_{0.15}\text{Se}_{0.95}\text{Cl}_{0.05}$, we theoretically calculated κ_{lat} for the MS sample (Figure 2. 29). We considered intrinsic Umklapp process, point defects, lattice strains, and dislocations detected by our Cs-STEM analysis as major phonon scattering mechanisms for the $\text{Sn}_{0.90}\text{Pb}_{0.15}\text{Se}_{0.95}\text{Cl}_{0.05}$ sample (See Supporting Information for the details). The calculated κ_{lat} using a Callaway-Debye model⁵⁸ matches well with the experimental values up to ~ 450 K, indicating observed nanostructures play an important role in scattering phonons in the corresponding range of temperature. Afterward, it is progressively deviated from them possibly due to a gradual disappearance of dislocations and strain fields at high temperature. To address this, we assumed that dislocation density can be linearly reduced above 550 K.⁵⁹ The modified model based on the hypothesis improves the agreement between experimental and theoretical κ_{lat} . As a consequence, the synergistic effect of point defects and dislocations with lattice strain fields could be the main reason for the reduced κ_{lat} for $\text{Sn}_{0.90}\text{Pb}_{0.15}\text{Se}_{0.95}\text{Cl}_{0.05}$. However, a reduction in the κ_{lat} is not as dramatic as

shown in representative nanostructured bulk TE materials.^{52, 54, 55}

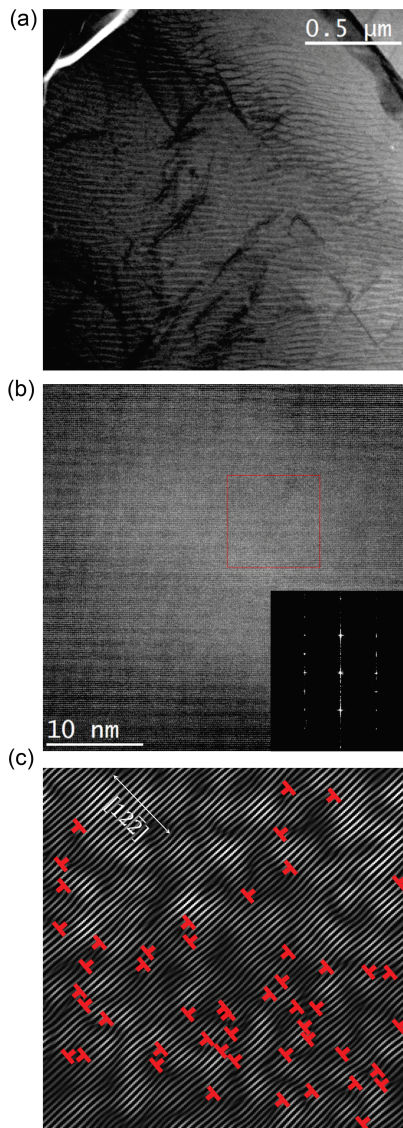


Figure 2. 22. Typical cross-sectional STEM images of $\text{Sn}_{0.90}\text{Pb}_{0.15}\text{Se}_{0.95}\text{Cl}_{0.05}$. (a) Low magnification annular bright field (ABF) and (b) medium-magnification high-angle annular dark-field (HAADF) STEM images. Inset in (b) shows the fast Fourier transform (FFT) image along the [201] axis. (c) Inverse FFT (IFFT) image taken at the red rectangle in (b). Red symbols indicate edge dislocations.

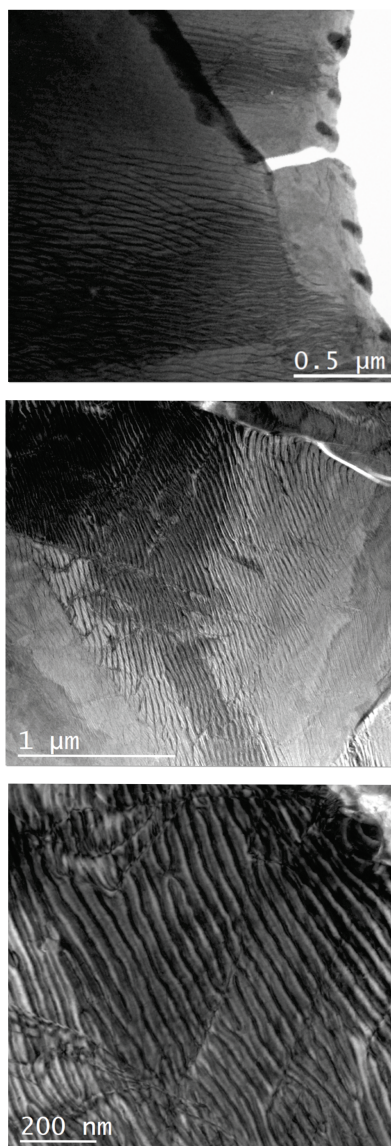


Figure 2. 23. Typical cross-sectional low magnification annular bright-field (ABF) scanning transmission electron microscope (STEM) images of the SPS-processed MS sample with the composition $\text{Sn}_{0.90}\text{Pb}_{0.15}\text{Se}_{0.95}\text{Cl}_{0.05}$ showing a substantial degree of moiré structures and edge dislocations.

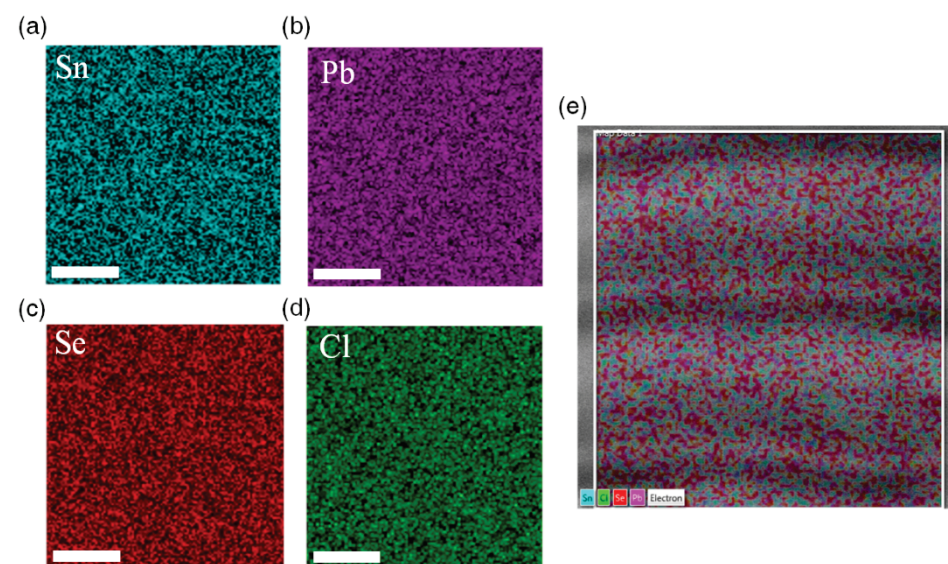
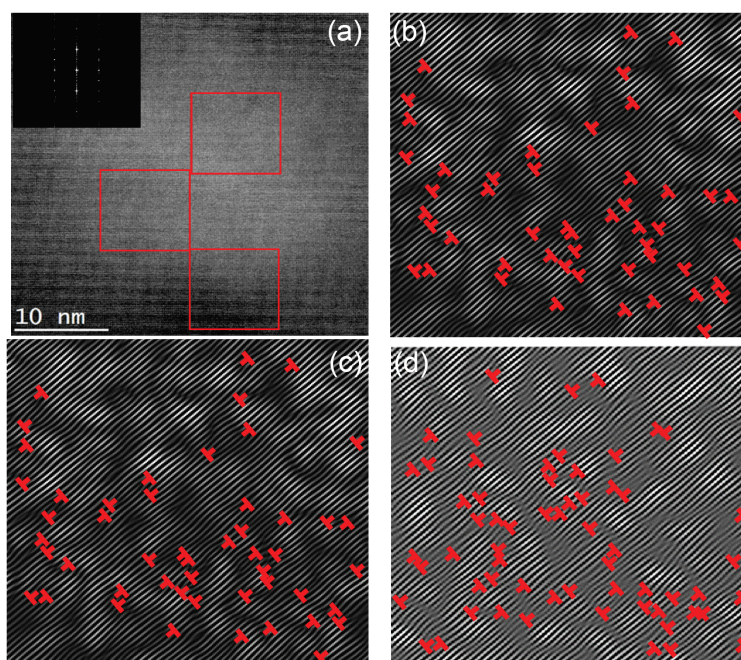


Figure 2. 24. Elemental maps scanned on the region with moiré structures by STEM-EDS. EDS signals for (a) Sn, (b) Pb, (c) Se, and (d) Cl atoms are depicted in cyan, magenta, red, and green color, respectively. These four panels jointly create the image in (e). Scale bar: 25 nm.



Density of dislocation

Area	Average	Standard deviation
100 nm ²	54	5.57

Figure 2. 25. (a) Typical medium-magnification ABF-STEM images of the MS sample of Sn_{0.90}Pb_{0.15}Se_{0.95}Cl_{0.05}. Inset: fast Fourier transform (FFT) image along the [201] axis. (b-d) are inverse FFT images for the red rectangles of 1, 2, and 3 in (a), respectively. Red symbols indicate edge dislocations. Average density of dislocations is given with standard deviation.

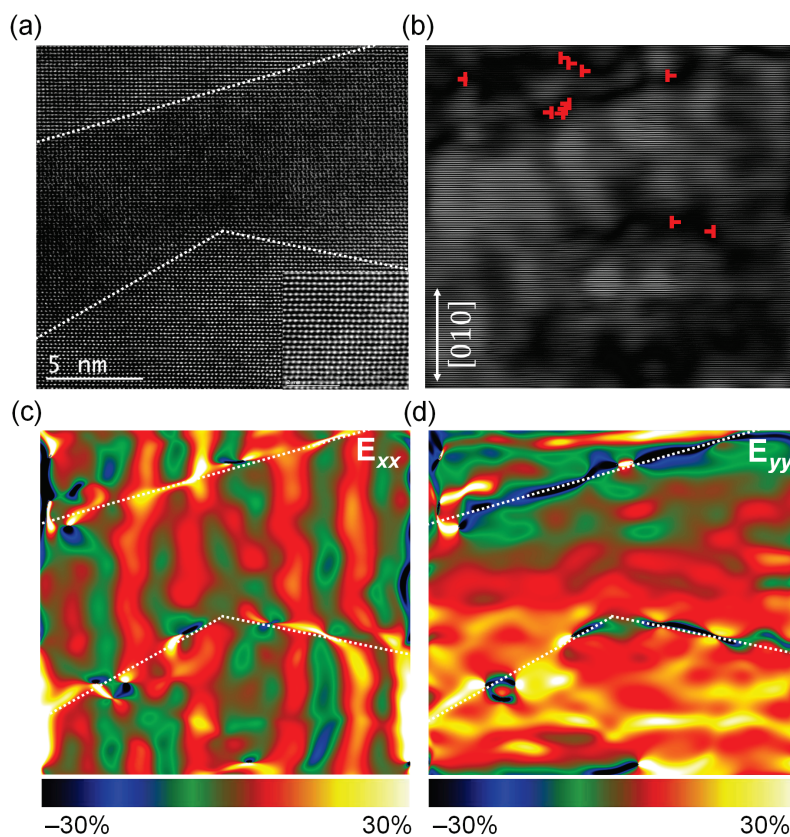


Figure 2. 26. (a) Representative HAADF-STEM image of $\text{Sn}_{0.90}\text{Pb}_{0.15}\text{Se}_{0.95}\text{Cl}_{0.05}$ viewed down the $[201]$ direction. Dotted lines outline the regions with a discernible contrast. Inset: the magnified atomic-resolution HAADF-STEM image showing the SnSe structure at the atomic scale. (b) IFFT image of (a). Red symbols indicate edge dislocations. (c) and (d) are lattice strain maps of the HAADF-STEM image in (a) demonstrating strain distributions around dislocations. The color bar displays the lattice strains from +30 to -30%.

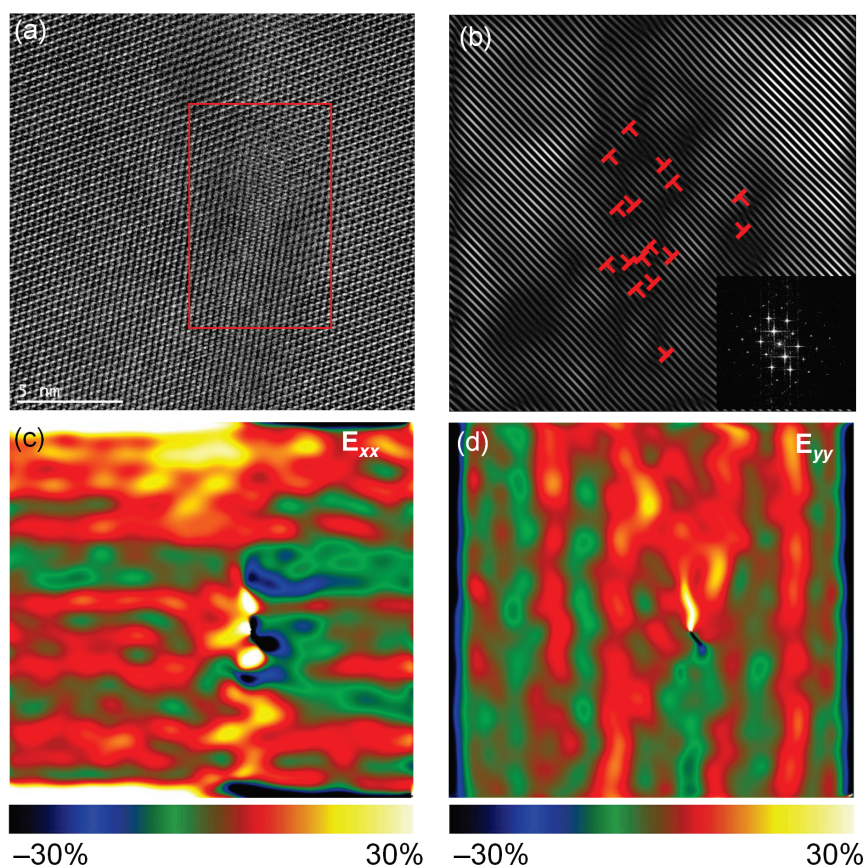


Figure 2. 27. (a) Representative high angle annular dark-field (HAADF) STEM image of $\text{Sn}_{0.90}\text{Pb}_{0.15}\text{Se}_{0.95}\text{Cl}_{0.05}$ viewed down the $[123]$ direction. Irregular atomic arrangements are observed in the red rectangle. (b) IFFT image of (a). Red symbols indicate edge dislocations. Inset: fast Fourier transform (FFT) image along the $[123]$ axis. (c) and (d) are lattice strain maps of HAADF-STEM image in (a) showing severe strain distributions around dislocations. The color bar indicates the lattice strain ranging from +30 to -30%.

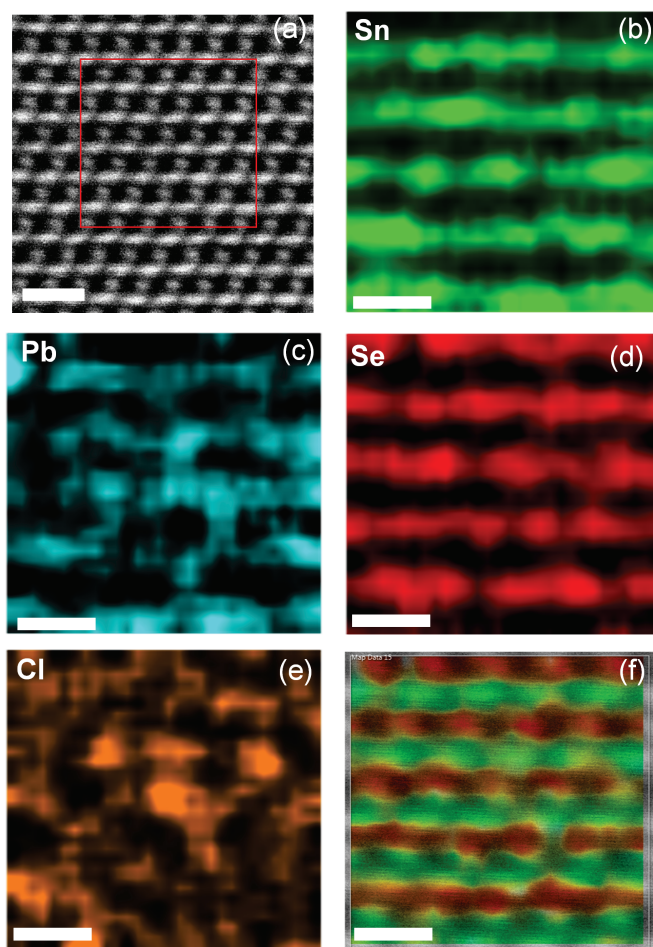


Figure 2. 28. (a) Magnified atomic-resolution HAADF-STEM image taken through the [123] zone axis. Atomic-resolution elemental mapping of (b) Sn, (c) Pb, (d) Se, and (e) Cl atoms depicted in green, cyan, red, and orange color, respectively, by STEM-EDS scanned on the red rectangle in (a). These four panels jointly create the image in (f), demonstrating direct observation of the crystal structure of $\text{Sn}_{0.90}\text{Pb}_{0.15}\text{Se}_{0.95}\text{Cl}_{0.05}$ at the atomic level and verifying the arrangement of constituent atoms. Scale bar: 0.5 nm.

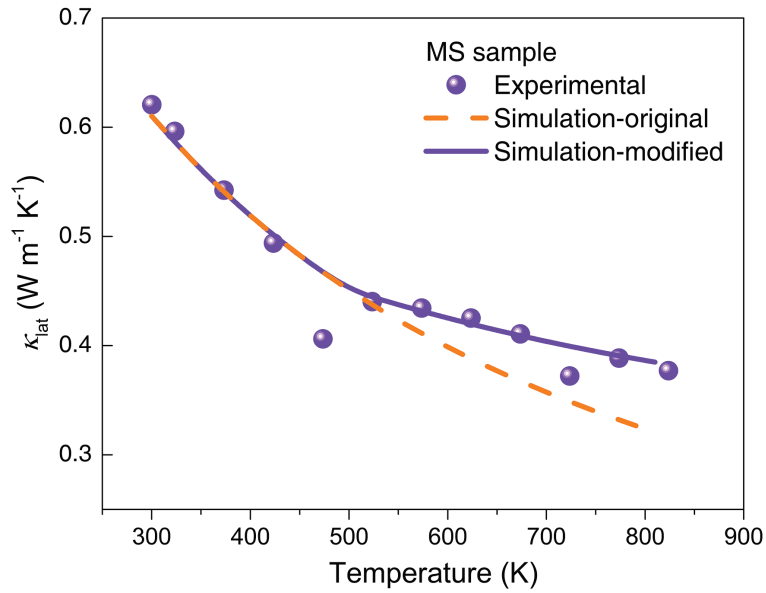


Figure 2. 29. Comparison of experimental (circles) and calculated κ_{lat} based on Umklapp, point defect, lattice strain, and dislocation scattering processes using a Callaway–Debye model (dotted line) for the MS sample of $\text{Sn}_{0.90}\text{Pb}_{0.15}\text{Se}_{0.95}\text{Cl}_{0.05}$ parallel to the press direction. The calculated κ_{lat} is further modified by the hypothesis that dislocation density can be linearly reduced above 550 K (solid line).

2.4 Conclusion

Because of strong intrinsic p-type conduction nature of SnSe, it is hard to achieve the optimal level of electron concentration by halogen doping for high n-type thermoelectric performance. Our strategy is minimizing p-type charge carriers by excess Sn, subsequently converting conduction behavior into n-type by doping electron donor Cl, and optimizing electron concentration by PbSe alloying. The role of PbSe alloying is unique in the $\text{Sn}_{1.05-x}\text{Pb}_x\text{Se}_{0.95}\text{Cl}_{0.05}$ system: unusually increasing electron concentration and mobility at the same time and thereby resulting in the highly improved electrical conductivity and power factor, in opposition to the general findings in p-type $\text{Sn}_{1-x}\text{Pb}_x\text{Se}$. This observation affirms the importance in developing specialized strategies for the respective n- and p-type thermoelectric materials. Dually incorporating PbSe and Cl induces heavily dense nanostructures, thereby dropping lattice thermal conductivity. The resultantly achieved ZT of 1.2, one of the highest among n-type polycrystalline SnSe-based materials, displays high potential of polycrystalline SnSe thermoelectrics for further improvement by new inventive strategies. We also demonstrated that intrinsic anisotropy in thermoelectric properties of SnSe can be significantly remedied by ball mill and post annealing processes, giving a comparable $ZT_{\text{max}} \sim 1.2$ parallel and perpendicular to the press directions of spark plasma sintering. This achievement can greatly enhance the prospect of low-cost and facile

processability and better machinability for SnSe thermoelectric legs used in module structure.

2.4 References

- [1] Gingerich, D. B.; Mauter, M. S. Quantity, Quality, and Availability of Waste Heat from United States Thermal Power Generation. *Environ. Sci. Technol.* **2015**, *49*, 8297-8306.
- [2] Johnson, I.; Choate, W. T.; Davidson, A. Waste Heat Recovery: Technology and Opportunities in US Industry. *US Department of Energy Industrial Technologies Program* **2008**.
- [3] Banik, A.; Shenoy, U. S.; Saha, S.; Waghmare, U. V.; Biswas, K. High Power Factor and Enhanced Thermoelectric Performance of SnTe-AgInTe₂: Synergistic Effect of Resonance Level and Valence Band Convergence. *J. Am. Chem. Soc.* **2016**, *138*, 13068-13075.
- [4] Tan, G.; Zhao, L.-D.; Kanatzidis, M. G. Rationally Designing High-Performance Bulk Thermoelectric Materials. *Chem. Rev.* **2016**, *116*, 12123-12149.
- [5] Kleinke, H. New bulk Materials for Thermoelectric Power Generation: Clathrates and Complex Antimonides. *Chem. Mater.* **2010**, *22*, 604-611.
- [6] Guo, Q.; Chan, M.; Kuropatwa, B. A.; Kleinke, H. Enhanced Thermoelectric Properties of Variants of Tl₉SbTe₆ and Tl₉BiTe₆. *Chem. Mater.* **2013**, *25*, 4097-4104.
- [7] Rogl, G.; Grytsiv, A.; Rogl, P.; Peranio, N.; Bauer, E.; Zehetbauer, M.; Eibl, O. n-Type Skutterudites (R,Ba,Yb)_yCo₄Sb₁₂ (R=Sr, La, Mm, DD, SrMm,

SrDD) Approaching $ZT \approx 2.0$. *Acta Mater.* **2014**, *63*, 30-43.

[8] Choi, G.; Kim, H. S.; Lee, K.; Park, S. H.; Cha, J.; Chung, I.; Lee, W. B. Study on Thermal Conductivity and Electrical Resistivity of Al-Cu Alloys Obtained by Boltzmann Transport Equation and first-principles simulation: Semi-empirical approach. *J. Alloys. Compd.* **2017**, *727*, 1237-1242.

[9] Shuai, J.; Ge, B.; Mao, J.; Song, S.; Wang, Y.; Ren, Z. Significant Role of Mg Stoichiometry in Designing High Thermoelectric Performance for $Mg_3(Sb,Bi)_2$ -Based n-Type Zintl. *J. Am. Chem. Soc.* **2018**, *140*, 1910-1915.

[10] Jana, M. K.; Pal, K.; Warankar, A.; Mandal, P.; Waghmare, U. V.; Biswas, K. Intrinsic Rattler-Induced Low Thermal Conductivity in Zintl Type $TlInTe_2$. *J. Am. Chem. Soc.* **2017**, *139*, 4350-4353.

[11] Hu, Y.; Chen, C.-W.; Cao, H.; Makhmudov, F.; Grebenkemper, J. H.; Abdusalyamova, M. N.; Morosan, E.; Kauzlarich, S. M. Tuning Magnetism of $[MnSb_4]^{9-}$ Cluster in $Yb_{14}MnSb_{11}$ through Chemical Substitutions on Yb Sites: Appearance and Disappearance of Spin Reorientation. *J. Am. Chem. Soc.* **2016**, *138*, 12422-12431.

[12] Liu, Y.; Sahoo, P.; Makongo, J. P. A.; Zhou, X.; Kim, S.-J.; Chi, H.; Uher, C.; Pan, X.; Poudeu, P. F. P. Large Enhancements of Thermopower and Carrier Mobility in Quantum Dot Engineered Bulk Semiconductors. *J. Am. Chem. Soc.* **2013**, *135*, 7486-7495.

[13] Kim, H.; Kaviany, M.; Thomas, J. C.; Van der Ven, A.; Uher, C.; Huang,

- B. Structural Order-Disorder Transitions and Phonon Conductivity of Partially Filled Skutterudites. *Phys. Rev. Lett.* **2010**, *105*, 265901.
- [14] Zhou, C.; Lee, Y. K.; Cha, J.; Yoo, B.; Cho, S.-P.; Hyeon, T.; Chung, I. Defect Engineering for High-Performance n-Type PbSe Thermoelectrics. *J. Am. Chem. Soc.* **2018**, *140*, 9282-9290.
- [15] Zhou, C.; Yu, Y.; Lee, Y. K.; Cojocaru-Mirédin, O.; Yoo, B.; Cho, S.-P.; Im, J.; Wuttig, M.; Hyeon, T.; Chung, I. High-Performance n-Type PbSe–Cu₂Se Thermoelectrics through Conduction Band Engineering and Phonon Softening. *J. Am. Chem. Soc.* **2018**, *140*, 15535-15545.
- [16] Park, K.; Ahn, K.; Cha, J.; Lee, S.; Chae, S. I.; Cho, S.-P.; Ryee, S.; Im, J.; Lee, J.; Park, S.-D.; Han, M. J.; Chung, I.; Hyeon, T. Extraordinary Off-Stoichiometric Bismuth Telluride for Enhanced n-Type Thermoelectric Power Factor. *J. Am. Chem. Soc.* **2016**, *138*, 14458-14468.
- [17] Sootsman, J. R.; Chung, D. Y.; Kanatzidis, M. G. New and Old Concepts in Thermoelectric Materials. *Angew. Chem., Int. Ed.* **2009**, *48*, 8616-8639.
- [18] Kanatzidis, M. G. Discovery-Synthesis, Design, and Prediction of Chalcogenide Phases. *Inorg. Chem.* **2017**, *56*, 3158-3173.
- [19] Kanatzidis, M. G. Nanostructured Thermoelectrics: The New Paradigm? *Chem. Mater.* **2010**, *22*, 648-659.
- [20] Biswas, K.; He, J.; Blum, I. D.; Wu, C. I.; Hogan, T. P.; Seidman, D. N.; Dravid, V. P.; Kanatzidis, M. G. High-Performance Bulk Thermoelectrics

- with All-Scale Hierarchical Architectures. *Nature* **2012**, *489*, 414-418.
- [21] Wu, H. J.; Zhao, L. D.; Zheng, F. S.; Wu, D.; Pei, Y. L.; Tong, X.; Kanatzidis, M. G.; He, J. Q. Broad Temperature Plateau for Thermoelectric Figure of Merit $ZT > 2$ in phase-separated $\text{PbTe}_{0.7}\text{S}_{0.3}$. *Nat. Commun.* **2014**, *5*, 4515.
- [22] He, J.; Zhao, L.-D.; Zheng, J.-C.; Doak, J. W.; Wu, H.; Wang, H.-Q.; Lee, Y.; Wolverton, C.; Kanatzidis, M. G.; Dravid, V. P. Role of Sodium Doping in Lead Chalcogenide Thermoelectrics. *J. Am. Chem. Soc.* **2013**, *135*, 4624-4627.
- [23] Biswas, K.; He, J.; Zhang, Q.; Wang, G.; Uher, C.; Dravid, V. P.; Kanatzidis, M. G. Strained Endotaxial Nanostructures with High Thermoelectric Figure of Merit. *Nat. Chem.* **2011**, *3*, 160-166.
- [24] Hsu, K. F.; Loo, S.; Guo, F.; Chen, W.; Dyck, J. S.; Uher, C.; Hogan, T.; Polychroniadis, E. K.; Kanatzidis, M. G. Cubic $\text{AgPb}_m\text{SbTe}_{2+m}$: Bulk Thermoelectric Materials with High Figure of Merit. *Science* **2004**, *303*, 818-821.
- [25] Pei, Y.; Shi, X.; LaLonde, A.; Wang, H.; Chen, L.; Snyder, G. J. Convergence of Electronic Bands for High Performance Bulk Thermoelectrics. *Nature* **2011**, *473*, 66-69.
- [26] Tan, G. J.; Shi, F. Y.; Hao, S. Q.; Zhao, L. D.; Chi, H.; Zhang, X. M.; Uher, C.; Wolverton, C.; Dravid, V. P.; Kanatzidis, M. G. Non-equilibrium

Processing Leads to Record High Thermoelectric Figure of Merit in PbTe-SrTe. *Nat. Commun.* **2016**, *7*, 12167.

[27] Jood, P.; Ohta, M.; Yamamoto, A.; Kanatzidis, M. G. Excessively Doped PbTe with Ge-Induced Nanostructures Enables High-Efficiency Thermoelectric Modules. *Joule* **2018**, *2*, 1339-1355.

[28] Zhao, L. D.; Lo, S. H.; Zhang, Y. S.; Sun, H.; Tan, G. J.; Uher, C.; Wolverton, C.; Dravid, V. P.; Kanatzidis, M. G. Ultralow Thermal Conductivity and High Thermoelectric Figure of Merit in SnSe Crystals. *Nature* **2014**, *508*, 373.

[29] Chang, C.; Wu, M.; He, D.; Pei, Y.; Wu, C.-F.; Wu, X.; Yu, H.; Zhu, F.; Wang, K.; Chen, Y.; Huang, L.; Li, J.-F.; He, J.; Zhao, L.-D. 3D Charge and 2D Phonon Transports Leading to High Out-of-plane ZT in n-Type SnSe Crystals. *Science* **2018**, *360*, 778-783.

[30] Lee, Y. K.; Ahn, K.; Cha, J.; Zhou, C.; Kim, H. S.; Choi, G.; Chae, S. I.; Park, J.-H.; Cho, S.-P.; Park, S. H.; Sung, Y.-E.; Lee, W. B.; Hyeon, T.; Chung, I. Enhancing p-Type Thermoelectric Performances of Polycrystalline SnSe via Tuning Phase Transition Temperature. *J. Am. Chem. Soc.* **2017**, *139*, 10887-10896.

[31] Ge, Z. H.; Song, D.; Chong, X.; Zheng, F.; Jin, L.; Qian, X.; Zheng, L.; Dunin-Borkowski, R. E.; Qin, P.; Feng, J.; Zhao, L. D. Boosting the Thermoelectric Performance of (Na,K)-Codoped Polycrystalline SnSe by

Synergistic Tailoring of the Band Structure and Atomic-Scale Defect Phonon Scattering. *J. Am. Chem. Soc.* **2017**, *139*, 9714-9720.

[32] Zhao, L. D.; Tan, G.; Hao, S.; He, J.; Pei, Y.; Chi, H.; Wang, H.; Gong, S.; Xu, H.; Dravid, V. P.; Uher, C.; Snyder, G. J.; Wolverton, C.; Kanatzidis, M. G. Ultrahigh Power Factor and Thermoelectric Performance in Hole-Doped Single-Crystal SnSe. *Science* **2016**, *351*, 141-144.

[33] Wei, T. R.; Tan, G.; Zhang, X.; Wu, C. F.; Li, J. F.; Dravid, V. P.; Snyder, G. J.; Kanatzidis, M. G. Distinct Impact of Alkali-Ion Doping on Electrical Transport Properties of Thermoelectric p-Type Polycrystalline SnSe. *J. Am. Chem. Soc.* **2016**, *138*, 8875-8882.

[34] Wei, T.-R.; Tan, G.; Wu, C.-F.; Chang, C.; Zhao, L.-D.; Li, J.-F.; Snyder, G. J.; Kanatzidis, M. G. Thermoelectric Transport Properties of Polycrystalline SnSe Alloyed with PbSe. *Appl. Phys. Lett.* **2017**, *110*, 053901.

[35] Lee, Y. K.; Luo, Z.; Cho, S.-P.; Kanatzidis, M. G.; Chung, I. Surface Oxide Removal for Polycrystalline SnSe Reveals Near-Single-Crystal Thermoelectric Performance. *Joule* **2019**, *3*, 719-731.

[36] Zhang, Q.; Chere, E. K.; Sun, J.; Cao, F.; Dahal, K.; Chen, S.; Chen, G.; Ren, Z. Studies on Thermoelectric Properties of n-Type Polycrystalline SnSe_{1-x}S_x by Iodine Doping. *Adv. Energy Mater.* **2015**, *5*, 1500360.

[37] Wang, X.; Xu, J.; Liu, G.; Fu, Y.; Liu, Z.; Tan, X.; Shao, H.; Jiang, H.;

Tan, T.; Jiang, J. Optimization of Thermoelectric Properties in n-Type SnSe Doped with BiCl₃. *Appl. Phys. Lett.* **2016**, *108*, 083902.

[38] Li, S.; Wang, Y.; Chen, C.; Li, X.; Xue, W.; Wang, X.; Zhang, Z.; Cao, F.; Sui, J.; Liu, X.; Zhang, Q. Heavy Doping by Bromine to Improve the Thermoelectric Properties of n-type Polycrystalline SnSe. *Adv. Sci.* **2018**, *5*, 1800598.

[39] Li, D.; Tan, X.; Xu, J.; Liu, G.; Jin, M.; Shao, H.; Huang, H.; Zhang, J.; Jiang, J. Enhanced Thermoelectric Performance in n-Type Polycrystalline SnSe by PbBr₂ Doping. *RSC Adv.* **2017**, *7*, 17906-17912.

[40] Chang, C.; Tan, Q.; Pei, Y.; Xiao, Y.; Zhang, X.; Chen, Y.-X.; Zheng, L.; Gong, S.; Li, J.-F.; He, J.; Zhao, L.-D. Raising Thermoelectric Performance of n-Type SnSe via Br Doping and Pb Alloying. *RSC Adv.* **2016**, *6*, 98216-98220.

[41] Park, S. H.; Jin, Y.; Cha, J.; Hong, K.; Kim, Y.; Yoon, H.; Yoo, C.-Y.; Chung, I. High-Power-Density Skutterudite-Based Thermoelectric Modules with Ultralow Contact Resistivity Using Fe–Ni Metallization Layers. *ACS Appl. Energy Mater.* **2018**, *1*, 1603-1611.

[42] Salvador, J. R.; Cho, J. Y.; Ye, Z.; Moczygemba, J. E.; Thompson, A. J.; Sharp, J. W.; Koenig, J. D.; Maloney, R.; Thompson, T.; Sakamoto, J.; Wang, H.; Wereszczak, A. A. Conversion Efficiency of Skutterudite-Based Thermoelectric Modules. *Phys. Chem. Chem. Phys.* **2014**, *16*, 12510-12520.

- [43] Hýtch, M. J.; Snoeck, E.; Kilaas, R. Quantitative Measurement of Displacement and Strain Fields from HREM Micrographs. *Ultramicroscopy* **1998**, *74*, 131-146.
- [44] Lotgering, F. K. Topotactical Reactions with Ferrimagnetic Oxides Having Hexagonal Crystal Structures—I. *J. Inorg. Nucl. Chem.* **1959**, *9*, 113-123.
- [45] Wang, X.; Xu, J.; Liu, G.-Q.; Tan, X.; Li, D.; Shao, H.; Tan, T.; Jiang, J. Texturing Degree Boosts Thermoelectric Performance of Silver-Doped Polycrystalline SnSe. *Npg Asia Materials* **2017**, *9*, e426.
- [46] Fu, Y.; Xu, J.; Liu, G.-Q.; Tan, X.; Liu, Z.; Wang, X.; Shao, H.; Jiang, H.; Liang, B.; Jiang, J. Study on Thermoelectric Properties of Polycrystalline SnSe by Ge Doping. *J. Electron. Mater.* **2017**, *46*, 3182-3186.
- [47] Li, Y.; Shi, X.; Ren, D.; Chen, J.; Chen, L. Investigation of the Anisotropic Thermoelectric Properties of Oriented Polycrystalline SnSe. *Energies* **2015**, *8*, 6275.
- [48] Villars, P.; Prince, A.; Okamoto, H. *Handbook of Ternary Alloy Phase Diagrams*, Asm Intl: USA, 1995.
- [49] Woolley, J. C.; Berolo, O. Phase Studies of the $Pb_{1-x}Sn_xSe$ Alloys. *Mater. Res. Bull.* **1968**, *3*, 445-450.
- [50] Volykhov, A. A.; Shtanov, V. I.; Yashina, L. V. Phase Relations between Germanium, Tin, and Lead Chalcogenides in Pseudobinary Systems

- Containing Orthorhombic Phases. *Inorg. Mater.* **2008**, *44*, 345-356.
- [51] Su, D.; Zhu, Y. Scanning Moiré Fringe Imaging by Scanning Transmission Electron Microscopy. *Ultramicroscopy* **2010**, *110*, 229-233.
- [52] Xin, J.; Wu, H.; Liu, X.; Zhu, T.; Yu, G.; Zhao, X. Mg Vacancy and Dislocation Strains as Strong Phonon Scatterers in $\text{Mg}_2\text{Si}_{1-x}\text{Sb}_x$ Thermoelectric Materials. *Nat. Energy* **2017**, *34*, 428-436.
- [53] Yang, L.; Chen, Z.-G.; Hong, M.; Wang, L.; Kong, D.; Huang, L.; Han, G.; Zou, Y.; Dargusch, M.; Zou, J. n-Type Bi-doped PbTe Nanocubes with Enhanced Thermoelectric Performance. *Nat. Energy* **2017**, *31*, 105-112.
- [54] Chen, Z.; Ge, B.; Li, W.; Lin, S.; Shen, J.; Chang, Y.; Hanus, R.; Snyder, G. J.; Pei, Y. Vacancy-Induced Dislocations within Grains for High-Performance PbSe Thermoelectrics. *Nat. Commun.* **2017**, *8*, 13828.
- [55] Zhou, C.; Lee, Y. K.; Cha, J.; Yoo, B.; Cho, S.-P.; Hyeon, T.; Chung, I. Defect Engineering for High-Performance n-Type PbSe Thermoelectrics. *J. Am. Chem. Soc.* **2018**, *140*, 9282-9290.
- [56] Hÿtch, M. J.; Snoeck, E.; Kilaas, R. Quantitative Measurement of Displacement and Strain Fields from HREM Micrographs. *Ultramicroscopy* **1998**, *74*, 131-146.
- [57] Wang, Z.; Saito, M.; McKenna, K. P.; Ikuhara, Y. Polymorphism of Dislocation Core Structures at the Atomic Scale. *Nat. Commun.* **2014**, *5*, 3239.
- [58] Callaway, J.; von Baeyer, H. C. Effect of Point Imperfections on Lattice

Thermal Conductivity. *Phys. Rev.* **1960**, *120*, 1149-1154.

[59] Pumphrey, P. H.; Gleiter, H. The Annealing of Dislocations in High-Angle Grain Boundaries. *Phil. Mag.* **1974**, *30*, 593-602.

Chapter 3. Ultrahigh Power Factor and Electron Mobility in n-Type Bi₂Te_{3-x%}Cu Stabilized under Excess Te Condition

3.1 Introduction

The global population growth and economic development require the 50% increased use of fossil fuels by 2040, which are being depleted rapidly.¹ Their consumption is inevitably accompanied by a large amount of CO₂ emission, causing serious environmental problems. In addition, they are main sources for generating electric energy, more than a half of which is lost as waste heat upon consumption.² Thermoelectric (TE) technology is a promising candidate to address these multiple issues because it can convert heat into electrical energy directly without releasing undesirable gaseous residues. TE devices also operate with no noise and vibration, giving high mechanical reliability. The performance of TE materials is typically expressed by a dimensionless figure of merit $ZT = \sigma S^2 T / \kappa_{\text{tot}}$, where σ is the electrical conductivity, S is the Seebeck coefficient, the product σS^2 is the power factor (PF), κ_{tot} is the total thermal conductivity, and T is absolute temperature.³ The κ_{tot} comprises electrical (κ_{ele}), lattice (κ_{lat}), and bipolar

thermal conductivities (κ_{bip}).

At present, TE materials exhibiting high ZT and PF simultaneously are scarce. Historically, improving ZT has been the main interest in this technology.⁴⁻¹⁶ Indeed, ZT has been greatly enhanced for last two decades mainly due to the discovery of new materials and many innovative strategies that can reduce κ_{tot} . However, κ_{tot} of representative TE systems is rapidly reaching a lower bound of the amorphous limit. In contrast, PF does not have a theoretical upper bound, but just a few strategies have been developed to improve PF .

With recent progress in ZT of TE materials, fabricating TE devices and enhancing their performance emerge as a primary task to commercialize this technology. Average ZT of TE materials determines the efficiency of TE devices. This is important when heat supply is unstable and limited so that TE devices have to generate power from a limited amount of heat. In contrast, PF directly determines output power density (ω) of TE devices at given working boundary conditions, which include the temperature gradient $(T_{\text{h}} - T_{\text{c}})/L$ and temperature difference $(T_{\text{h}} - T_{\text{c}})$. It is expressed by the equation (1):¹⁷⁻¹⁸

$$\omega = \frac{1}{4} \frac{(T_{\text{h}} - T_{\text{c}})^2}{L} PF \quad (1)$$

where T_{h} and T_{c} are the temperature at hot and cold side of the TE materials,

respectively, and L is the dimension of the TE legs, along which the temperature gradient is applied. Output power density is a pivotal specification of TE devices to advertise their capability of generating power from heat on commercial markets.¹⁹⁻²¹ PF is of paramount importance when heat source is either unlimited or given consistently at low or free cost.²²⁻²⁴ It is important to note that κ_{tot} does not affect output power density under steady-state heat conduction.²⁵ Based on these accounts, it is essential to develop strategies of enhancing PF of TE materials.

Bi_2Te_3 -based compounds serve as representative TE materials for near ambient temperature power generation. There are still major challenges that should be addressed for this important class of TE materials. First, few performance-enhancing strategies have been established for Bi_2Te_3 -based materials. Proven dopants and substituents for both the n- and p-type materials are also limited. These result in the sluggish improvement in their TE performance. This is in striking contrast to the recent advance in PbTe -based compounds operating in the intermediate temperature range. Their performance has been greatly improved by numerous innovative strategies. For example, κ_{lat} can be reduced substantially with minimal damage in electrical transport properties by nanostructuring^{10, 26-27} and hierarchical architecture.²⁸ A few strategies have been introduced to improve their PF , for instance, energy-filtering effect^{14,29} and band engineering such as band

convergence,³⁰⁻³² resonant states,³³⁻³⁴ and band flattening³⁵ although it is still challenging.

Second, n-type Bi₂Te₃-based materials underperform the p-type counterparts in terms of PF and ZT , resulting in serious performance imbalance between the n- and p-type materials. ZT of the latter has been raised mainly by reducing κ_{lat} through defect engineering³⁶⁻³⁷ and mechanical processes to obtain nanoscale grains such as ball-milling,³⁸ hot deformation,^{37, 39} and melt-spinning.⁴⁰ However, such strategies proven for the p-type Bi₂Te₃-based materials are mostly ineffective for the n-type materials, making it highly challenging to enhance their TE performance. Electrical transport properties of the latter tend to be heavily damaged by mechanical nanostructuring in contrast to the cases of the former. Furthermore, most high performance n-type Bi₂Te₃-based materials are alloyed with Se to form Bi₂Te_{3-x}Se_x, leading to the sacrificed PF for reducing κ_{lat} .⁴¹⁻⁴² As a result, they typically exhibit much lower PF than the p-type cousins. The commercially available n-type materials are highly oriented ingots of Bi₂Te_{3-x}Se_x prepared by a relatively tedious process of zone melting (ZM), showing remarkably high PF of 43 $\mu\text{W cm}^{-1} \text{K}^{-2}$ at 300 K.³⁶ However, ZM ingots suffer from intrinsically poor mechanical stability because of the cleavage along the basal plane, making them unreliable for device fabrication.⁴³

Enhancing TE properties of n-type Bi₂Te₃-based materials has been relatively undeveloped. Among a few of examples, incorporating Cu atoms into Bi₂Te_{3-x}Se_x has been extensively studied. Cu is amphoteric dopant to Bi₂Te_{3-x}Se_x. It is reported to either substitute for Bi atom to induce p-type conduction⁴⁴⁻⁴⁶ or be inserted into interlayer and/or interstitial sites to give n-type conduction.^{41, 47} For the latter case, high *PF* of $\sim 31.5 \mu\text{W cm}^{-1} \text{K}^{-2}$ and *ZT* of 0.99 was achieved in ball-milled and hot pressed Cu_{0.01}Bi₂Te_{2.7}Se_{0.3} samples.⁴¹ Recently, extraordinary off-stoichiometric bulk K_{0.06}Bi₂Te_{3.18} was stabilized by a combined process of kinetically-controlled nanosynthesis and subsequent SPS, exhibiting very high *PF* of $\sim 43 \mu\text{W cm}^{-1} \text{K}^{-2}$ and *ZT* > 1.1 at 323 K. Highly excess K and Te atoms in K_{0.06}Bi₂Te_{3.18} occupy interlayer and interstitial voids in the Bi₂Te₃ structure.⁴⁸

Here we report a new n-type polycrystalline Bi₂Te₃ system with the nominal composition Cu_xBi₂Te_{3.17} ($x = 0.02 - 0.06$) exhibiting ultrahigh power factor and carrier mobility near room temperature. These compounds are uniquely stabilized by the reaction of Bi₂Te₃ with excess Cu and Te and the subsequent consolidation by spark plasma sintering (SPS). Excess Te serves as “catalysis” for enhancing charge transport and suppressing thermal transport properties simultaneously. It only exists in the reaction melts and plays several highly favourable roles, and is expelled out by SPS under high pressure. First, excess Te present in the reaction melt suppresses the intrinsic

generation of adverse Te vacancies in Bi_2Te_3 and optimizes a carrier concentration. In fact, high carrier concentration is unfavorable for charge transport properties because it reduces carrier mobility and Seebeck coefficient. Second, excess Te helps stabilize the high content of Cu up to 6 mol% into Bi_2Te_3 structure, leading to ultrahigh carrier mobility. The Cu doping level is far above the solubility limit allowed by the phase diagram.⁴⁹ Third, it induces high-density edge dislocations, thereby considerably reducing κ_{lat} .

The incorporation of high concentration Cu atoms, enabled by excess Te in the reaction melt, induces unusual charge transport behaviors. The carrier concentration and mobility of SPS $\text{Cu}_x\text{Bi}_2\text{Te}_{3.17}$ samples increase simultaneously with the higher extent of Cu doping, contrary to the general trend of their mutual inverse proportionality. As a result, the electrical conductivity of $\text{Cu}_x\text{Bi}_2\text{Te}_{3.17}$ also increases with the larger amount of Cu. The synergistic effect of excess Cu and Te leads to ultrahigh mobility $\sim 467 \text{ cm}^2 \text{ V}^{-1} \text{ s}^{-1}$ and $PF \sim 45 \mu\text{W cm}^{-1} \text{ K}^{-2}$ for the $x = 0.06$ sample of SPS $\text{Cu}_x\text{Bi}_2\text{Te}_{3.17}$. These are record high values reported to date for polycrystalline n-type Bi_2Te_3 -based materials. In fact, poorer PF of the n-type Bi_2Te_3 -based materials has been a major challenge in improving the output power of TE power generators operating near ambient temperature. The novelty of this

work can be highlighted by TE properties of control samples. As-prepared $\text{Cu}_x\text{Bi}_2\text{Te}_{3.17}$ ingots exhibit p-type conduction. SPS processed samples with the nominal composition $\text{Cu}_x\text{Bi}_2\text{Te}_3$ without excess Te show the decreasing electrical conductivity with the higher mole fraction of Cu doping, and underperform the SPS $\text{Cu}_x\text{Bi}_2\text{Te}_{3.17}$.

3.2 Experimental section.

3.2.1 Reagents

The reagents in this work were used as received unless noted otherwise: Bi shot (99.999%, 5N Plus, Canada), Te shot (99.999%, 5N Plus, Canada), and Cu wire (99.99%, 5N Plus, Canada)

3.2.2 Synthesis

Ingots with the nominal compositions “ $\text{Cu}_x\text{Bi}_2\text{Te}_{3.17}$ ” ($x = 0, 0.02, 0.04, 0.06, 0.08,$ and 0.10) were synthesized by reacting an appropriate molar ratio of starting reagents in evacuated fused silica tubes at 973 K for 12h, followed by quenching to water. Afterward, the nominal composition will be used for specimens. The synthesized ingots were ground into fine powders, loaded into a 13mm diameter graphite die in an Ar-filled glove box, and densified by spark plasma sintering (SPS) (SPS-211Lx, Fuji Electronic Industrial Co., Japan) in 823 K for 20 min under an axial pressure of 50 MPa. Although all these SPS-processed “ $\text{Cu}_x\text{Bi}_2\text{Te}_{3.17}$ ” samples are phase pure, our discussion will concentrate on the samples with $x = 0 - 0.06$. Data for the other samples are given in Supporting Information. Control SPS samples with the nominal composition “ $\text{Cu}_x\text{Bi}_2\text{Te}_3$ ” ($x = 0.02$ and 0.04) were prepared similarly. For control ingot samples with the nominal composition “ $\text{Cu}_x\text{Bi}_2\text{Te}_{3.17}$ ”, the reaction mixtures of appropriate ratios of starting reagents were melted at

973 K for 12h, followed by slow cooling to room temperature at a rate of 5 K h⁻¹. The as-obtained control ingot sample has a diameter of 11 mm, height of ~50 mm, and mass density of 7.78 g cm⁻³. It is not single crystalline, but shows a highly ordered lamellar morphology.

3.2.3 Powder X-ray Diffraction (XRD)

Powder XRD patterns were taken using a calibrated SmartLab Rigaku powder X-ray diffractometer with Cu K α ($\lambda = 1.5418 \text{ \AA}$) graphite monochromatized radiation operating at 40 kV and 30 mA at room temperature. Lattice parameters were refined by a least squares minimization procedure using PDXL ver. 2, which is an integrated powder XRD analysis software suite.

3.2.4 Morphology and Elemental Analysis

Morphology images and semiquantitative elemental analyses were obtained with a JSM-6701F field emission scanning electron microscope equipped with an energy dispersive X-ray spectrometer (EDS). EDS analysis for samples with the nominal composition Cu_xBi₂Te_{3.17} ($x = 0.02, 0.04,$ and 0.06) gives average compositions “Cu_{0.01}Bi₂Te_{3.20}”, “Cu_{0.05}Bi₂Te_{3.18}”, and “Cu_{0.07}Bi₂Te_{3.14}” before SPS and “Cu_{0.01}Bi₂Te_{3.02}”, “Cu_{0.04}Bi₂Te_{3.04}”, and “Cu_{0.05}Bi₂Te_{3.03}” after SPS. The analyzed average compositions for control samples with the nominal composition Cu_xBi₂Te₃ ($x = 0.02$ and 0.04) are “Cu_{0.02}Bi₂Te_{3.07}” and “Cu_{0.04}Bi₂Te_{3.02}”, respectively.

3.2.5 Thermal Analysis

Thermogravimetric analysis (TGA) was performed using a Netzsch TG 209 F1 thermogravimetric analyser. Samples in an alumina container were heated to 823 K at a rate of 10 K min⁻¹ under an Ar atmosphere.

3.2.6 Charge Transport Properties

Samples were cut and polished into parallelepipeds with dimensions $\sim 3 \times 3 \times 11$ mm³. Electrical conductivity and Seebeck coefficient were measured simultaneously from room temperature to 473 K under a He atmosphere on an ULVAC-RIKO ZEM-3 instrument.

3.2.7 Thermal Transport Properties

Samples were cut and polished into disks with a radius of ~ 8 mm and a thickness of ~ 1.5 mm under a N₂ atmosphere. The prepared disks were coated with graphite before characterization. Thermal diffusivity (D) was directly obtained by the laser flash diffusivity method using a Netzsch LFA 457 MicroFlash instrument. Thermal conductivity was calculated from the relation $\kappa_{\text{tot}} = DC_p\rho$, where C_p is the specific heat capacity and ρ is the mass density of the materials. The C_p can be derived indirectly employing a standard sample of Pyroceram. ρ was calculated from geometrical dimensions and masses of specimens (Table S1).

3.2.8 Hall Coefficient Measurement

The Hall effect measurement with respect to temperature in a 1.5 T magnetic field was performed on a Lake Shore HMS8407 system. Carrier concentration (n_H) and mobility (μ_H) were calculated by the formula $n_H = 1 / (eR_H)$ and $\mu_H = \sigma R_H$, respectively.

3.2.9 Transmission Electron Microscope (TEM) measurements

Specimen for TEM investigations was prepared using gallium ion milling with focused ion beams (FIB, Helios 650, FEI) with a dual beam microscope. TEM analyses were performed on a JEM ARM-200F microscope (Cold FEG Type, JEOL), installed at the National Center for Inter-university Research Facilities (NCIRF) at Seoul National University.

Nominal composition	Density (g cm ⁻³)
Control SPS Cu _{0.02} Bi ₂ Te ₃	7.68
Control SPS Cu _{0.04} Bi ₂ Te ₃	7.63
Control ingot Cu _{0.06} Bi ₂ Te _{3.17}	7.78
SPS Cu _{0.02} Bi ₂ Te _{3.17}	7.82
SPS Cu _{0.04} Bi ₂ Te _{3.17}	7.71
SPS Cu _{0.06} Bi ₂ Te _{3.17}	7.84

Table 3. 1. Mass density of the SPS Cu_xBi₂Te_{3.17} (x= 0.02, 0.04, and 0.06) and control samples.

3.3. Results and discussion

3.3.1 Synthesis and Structural Characterization.

The title compounds of this work with the nominal composition $\text{Cu}_x\text{Bi}_2\text{Te}_{3.17}$ ($x = 0.02, 0.04, \text{ and } 0.06$) were synthesized in ingot forms by the vacuum melting method, pulverized into fine powders, and subsequently pressed by spark plasma sintering (SPS) into dense pellets. The resulting samples are denoted as ‘SPS $\text{Cu}_x\text{Bi}_2\text{Te}_{3.17}$ ’ to emphasize the nominal composition. According to energy dispersive spectroscopy (EDS) analysis, the average composition for SPS $\text{Cu}_x\text{Bi}_2\text{Te}_{3.17}$ ($x = 0.02, 0.04, \text{ and } 0.06$) is “ $\text{Cu}_{0.01}\text{Bi}_2\text{Te}_{3.02}$ ”, “ $\text{Cu}_{0.04}\text{Bi}_2\text{Te}_{3.04}$ ”, and “ $\text{Cu}_{0.05}\text{Bi}_2\text{Te}_{3.03}$ ”, respectively (Table S2). Dark grey bubbles were ejected out of the resulting pellets after SPS, which were mostly Te with a trace of “ $\text{Cu}_x\text{Bi}_2\text{Te}_3$ ” according to the results of X-ray diffraction (XRD) (Figure 3. 1). This observation indicates that most of excess Te is forced out of the pellets during SPS under high temperature and pressure. The similar result was reported that an excess amount of Te is squeezed out from the reaction mixture of stoichiometric $\text{Bi}_{0.5}\text{Sb}_{1.5}\text{Te}_3$ and 25 weight% excess Te to give pure $\text{Bi}_{0.5}\text{Sb}_{1.5}\text{Te}_3$ by melt spinning and subsequent SPS processes.⁴⁰ We also prepared two kinds of control samples to compare their charge and phonon transport properties. The first one is as-grown ingots with the same nominal composition $\text{Cu}_x\text{Bi}_2\text{Te}_{3.17}$, which was obtained by

cooling the corresponding melts slowly without a subsequent SPS process to maintain the nominal composition in samples. These samples are designated as ‘Cu_xBi₂Te_{3.17} ingot’. The second one was prepared by the same procedure as the title samples except for the nominal composition Cu_xBi₂Te₃ ($x = 0.02$ and 0.04) with no excess Te, which is denoted as ‘SPS Cu_xBi₂Te₃’. Note that the analysed compositions by EDS for two kinds of control samples are close to their nominal ones (Table 3. 2 and 3. 3). Accordingly, SPS Cu_xBi₂Te_{3.17} and SPS Cu_xBi₂Te₃ samples have nearly the same quantitative compositions. This is the reason we use the nominal composition for samples.

To investigate the phase homogeneity of SPS Cu_xBi₂Te_{3.17} samples, we reground SPS specimens to fine powders and took XRD patterns. Despite the presence of a high degree of Cu doping detected by EDS, all samples crystallize in the Bi₂Te₃ type structure with the space group $R\bar{3}mH$ (PDF# 15-0863) without the extra Bragg reflection peaks from impurities within the detection limit of laboratory XRD instrument (Figure 3. 2a). We observed that the (006) reflection peak around $\sim 15^\circ$ shifts to a lower angle with the higher Cu concentration (Figure 3. 2b). The refined unit cells reveal that the cell dimension expands significantly from 30.409(5) Å for Bi₂Te_{3.17} to 30.471(6) Å for Cu_{0.06}Bi₂Te_{3.17} along the c -axis due to the widened interlayer distance (Figures 3. 2c). This result implies that a majority of Cu is intercalated into the van der Waals gaps between the Bi₂Te₃ layers. The slight

increase from 4.373(3) to 4.383(2) Å along the *a*-axis for the same samples strongly suggests that the rest of Cu presumably occupies interstitial voids in the Bi₂Te₃ lattices rather than replaces Bi, given the large difference in ionic radius of Cu⁺ (0.91 Å) and Bi³⁺ (1.17 Å) in octahedral coordination environment and the large enough interstitial holes to accommodate small Cu⁺ cations (Figure 3. 2d).⁵⁰ This model is further supported by their TE properties as described later.

The XRD patterns of control SPS Cu_{*x*}Bi₂Te₃ samples are also indexed as the Bi₂Te₃ structure without the presence of impurity phase. Neither the change in cell dimension nor evolution of secondary phase is observed before and after SPS, indicating no chemical change during SPS (Figure 3.3a). However, control SPS Cu_{*x*}Bi₂Te₃ samples show the narrower solubility limit of Cu in the Bi₂Te₃ matrix than SPS Cu_{*x*}Bi₂Te_{3.17} samples so that the *x* = 0.06 sample of the former cannot be obtained in a pure form. This implies that excess Te in the reaction mixture of the latter help the unusually high concentration of Cu atom to be stabilized in the Bi₂Te₃ structure. The former has nearly the same and slightly smaller cell dimension along the *a*- and *c*-axes, respectively, than the latter (Figure 3. 3b and 3c and Table 3. 4). For example, the respective cell parameter for the *c*-axis is 30.416(3) and 30.438(3) Å for the *x* = 0.02 and 0.04 samples.

Contrary to the phase homogeneity of SPS Cu_{0.06}Bi₂Te_{3.17}, the

control as-grown $\text{Cu}_{0.06}\text{Bi}_2\text{Te}_{3.17}$ ingot without post-SPS process shows the extra Bragg reflection peaks, which correspond to CuTe (~ 13 , 26 , and 31°) and elemental Te ($\sim 23^\circ$) (Figure 3. 4). We could not directly observe the position of Cu atoms in the Bi_2Te_3 structure by atomic-resolution scanning transmission electron microscopy due to the sensitivity of samples upon extended exposure to focused ion beams and electrons. In fact, the exact location of Cu atoms in Bi_2Te_3 -based materials could not be directly determined in the previous reports.⁴¹

Thermogravimetric analysis (TGA) data at a rate of 10 K min^{-1} under an Ar flow show that SPS $\text{Cu}_x\text{Bi}_2\text{Te}_{3.17}$ samples do not lose a weight up to 850 K , demonstrating their thermal stability and phase homogeneity despite the unusually high Cu concentration in the Bi_2Te_3 structure (Figure 3. 5). In contrast, the control $\text{Cu}_{0.06}\text{Bi}_2\text{Te}_{3.17}$ ingot sample without a post-SPS process loses weight above $\sim 670 \text{ K}$ as elemental Te does. This observation indicates that a majority of excess Te cannot be dissolved in the Bi_2Te_3 structure by the melting reaction, and decomposes out near its melting point of 720 K . The TGA results are consistent with those of XRD.

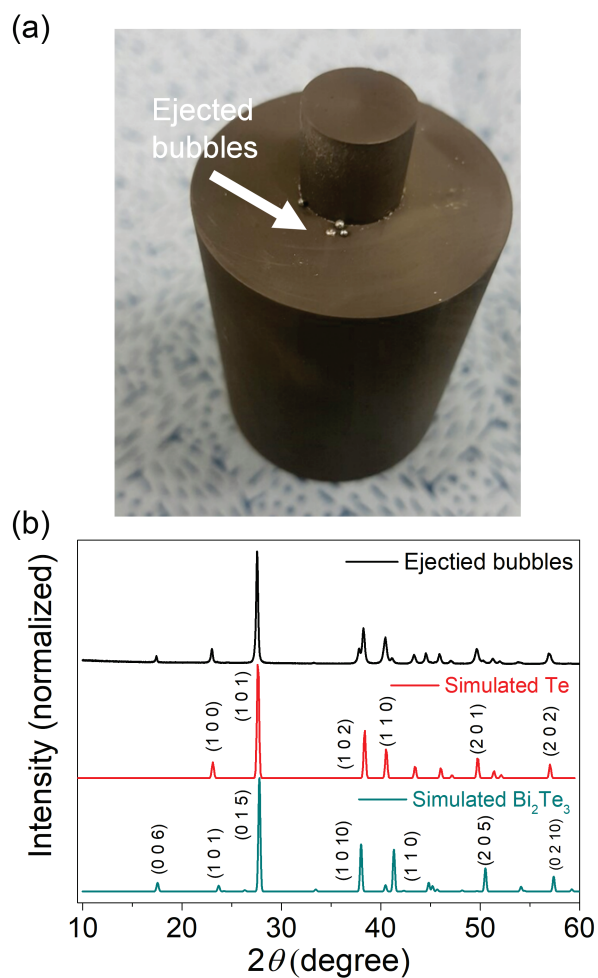


Figure 3. 1. (a) A photograph of the graphite mold after SPS for the $\text{Cu}_{0.06}\text{Bi}_2\text{Te}_{3.17}$ sample. Gray bubbles are seen, which were squeezed out of the pellet during SPS. (b) Powder XRD pattern for the ejected material in comparison with those of reference Bi_2Te_3 and Te. (The International Centre for Diffraction Data (ICDD) Bi_2Te_3 (PDF# 15-0863) and Te (PDF# 36-1452)).

Nominal composition	Analyzed average composition	
	Before SPS	After SPS
$\text{Cu}_{0.02}\text{Bi}_2\text{Te}_{3.17}$	“ $\text{Cu}_{0.01}\text{Bi}_2\text{Te}_{3.20}$ ”	“ $\text{Cu}_{0.01}\text{Bi}_2\text{Te}_{3.02}$ ”
$\text{Cu}_{0.04}\text{Bi}_2\text{Te}_{3.17}$	“ $\text{Cu}_{0.05}\text{Bi}_2\text{Te}_{3.18}$ ”	“ $\text{Cu}_{0.04}\text{Bi}_2\text{Te}_{3.04}$ ”
$\text{Cu}_{0.06}\text{Bi}_2\text{Te}_{3.17}$	“ $\text{Cu}_{0.07}\text{Bi}_2\text{Te}_{3.14}$ ”	“ $\text{Cu}_{0.05}\text{Bi}_2\text{Te}_{3.03}$ ”

Nominal composition	Analyzed average composition
Control ingot $\text{Cu}_{0.06}\text{Bi}_2\text{Te}_{3.17}$	“ $\text{Cu}_{0.07}\text{Bi}_2\text{Te}_{3.18}$ ”

Table 3. 2. The analyzed average chemical composition by EDS before and after SPS process for the title samples with the nominal composition $\text{Cu}_x\text{Bi}_2\text{Te}_{3.17}$ ($x = 0.02, 0.04, \text{ and } 0.06$) and the control ingot sample with the nominal composition $\text{Cu}_{0.06}\text{Bi}_2\text{Te}_{3.17}$.

Nominal composition	Analyzed average composition
Before SPS $\text{Cu}_{0.02}\text{Bi}_2\text{Te}_3$	" $\text{Cu}_{0.02}\text{Bi}_2\text{Te}_{3.01}$ "
SPS $\text{Cu}_{0.02}\text{Bi}_2\text{Te}_3$	" $\text{Cu}_{0.02}\text{Bi}_2\text{Te}_{3.07}$ "
Before SPS $\text{Cu}_{0.04}\text{Bi}_2\text{Te}_3$	" $\text{Cu}_{0.03}\text{Bi}_2\text{Te}_{2.99}$ "
SPS $\text{Cu}_{0.04}\text{Bi}_2\text{Te}_3$	" $\text{Cu}_{0.04}\text{Bi}_2\text{Te}_{3.02}$ "

Table 3. 3. The analyzed average chemical composition by EDS for control samples with the nominal composition $\text{Cu}_x\text{Bi}_2\text{Te}_3$ ($x= 0.02$ and 0.04) before and after SPS process.

Sample	Cell parameters	
	a, b (Å)	c (Å)
Control SPS $\text{Cu}_{0.02}\text{Bi}_2\text{Te}_3$	4.372(3)	30.416(3)
Control SPS $\text{Cu}_{0.04}\text{Bi}_2\text{Te}_3$	4.376(3)	30.438(3)
SPS $\text{Cu}_{0.02}\text{Bi}_2\text{Te}_{3.17}$	4.373(3)	30.430(4)
SPS $\text{Cu}_{0.04}\text{Bi}_2\text{Te}_{3.17}$	4.380(2)	30.456(6)
SPS $\text{Cu}_{0.06}\text{Bi}_2\text{Te}_{3.17}$	4.383(2)	30.471(6)

Table 3. 4. The refined cell parameters for SPS $\text{Cu}_x\text{Bi}_2\text{Te}_{3.17}$ ($x = 0.02, 0.04,$ and 0.06) and the control SPS $\text{Cu}_x\text{Bi}_2\text{Te}_3$ ($x = 0.02$ and 0.04).

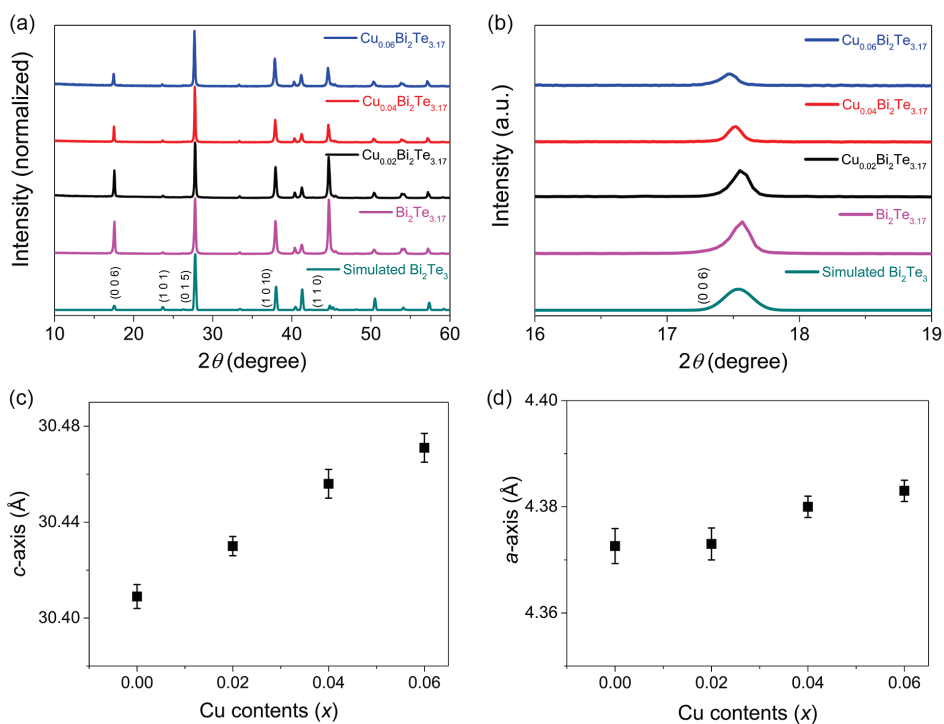


Figure 3. 2. (a) Powder XRD data for the SPS $\text{Cu}_x\text{Bi}_2\text{Te}_{3.17}$ ($x = 0-0.06$) samples in comparison with the theoretical pattern for Bi_2Te_3 (JCPDS 15-0863). (b) The (006) reflection peak shifts downward with the higher Cu concentration. The refined lattice parameters with respect to the Cu content along (c) the c- and (d) the a-axes are given with the standard deviation.

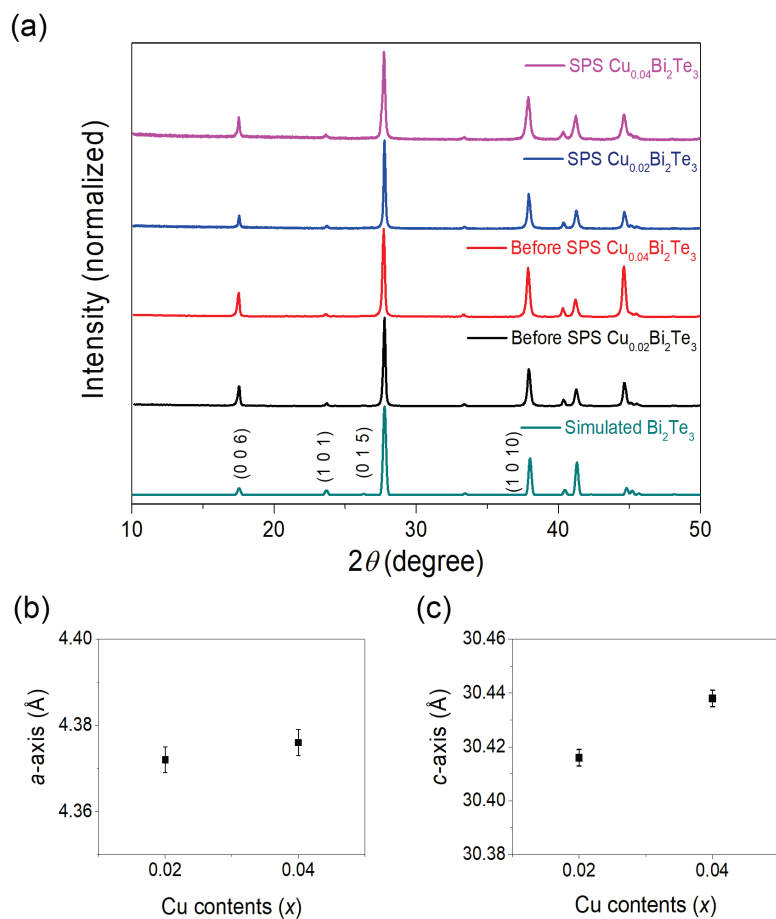


Figure 3. 3. (a) Powder XRD patterns for control $\text{Cu}_x\text{Bi}_2\text{Te}_3$ ($x = 0.02$ and 0.04) samples before and after SPS process. The refined lattice parameters with respect to the Cu content for control SPS $\text{Cu}_x\text{Bi}_2\text{Te}_3$ samples along (b) the a - and (c) the c -axes.

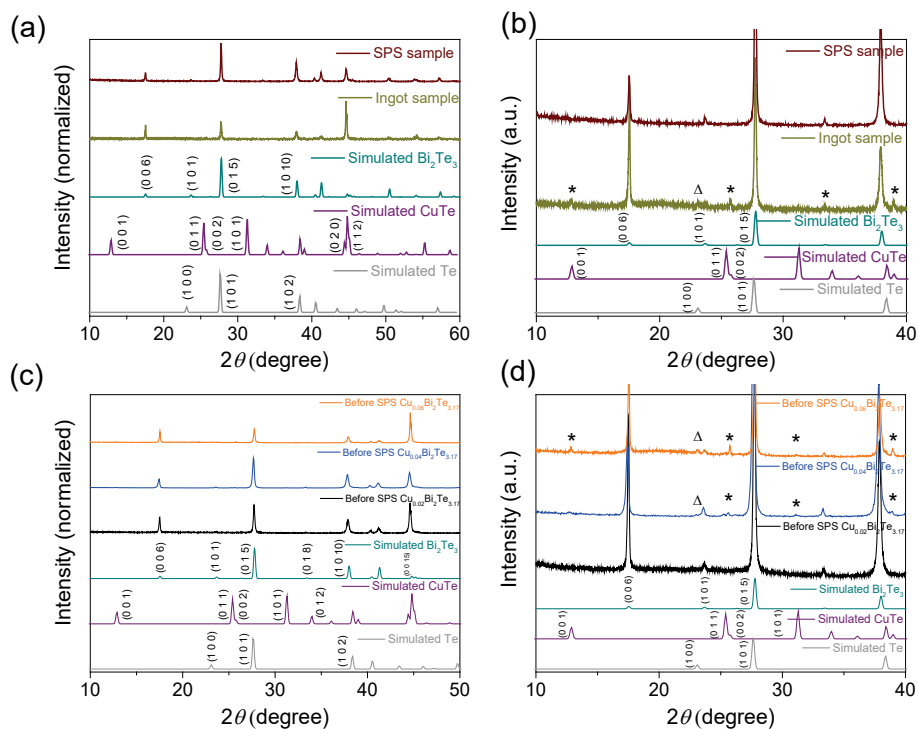


Figure 3. 4. (a) Powder XRD patterns and (b) magnified XRD patterns around $10 \sim 40^\circ$ for SPS $\text{Cu}_{0.06}\text{Bi}_2\text{Te}_{3.17}$ and control ingot $\text{Cu}_{0.06}\text{Bi}_2\text{Te}_{3.17}$ samples, which have the same nominal composition. The theoretically calculated patterns for Bi_2Te_3 , CuTe , and Te are given for comparison. (ICDD Bi_2Te_3 (PDF# 15-0863), CuTe (PDF# 01-070-8050), and Te (PDF# 36-1452)). The Bragg diffraction peaks for CuTe and Te are marked by asterisks and triangles, respectively. (c) Powder XRD patterns and (d) magnified XRD patterns around $10 \sim 40^\circ$ for $\text{Cu}_x\text{Bi}_2\text{Te}_{3.17}$ before SPS process.

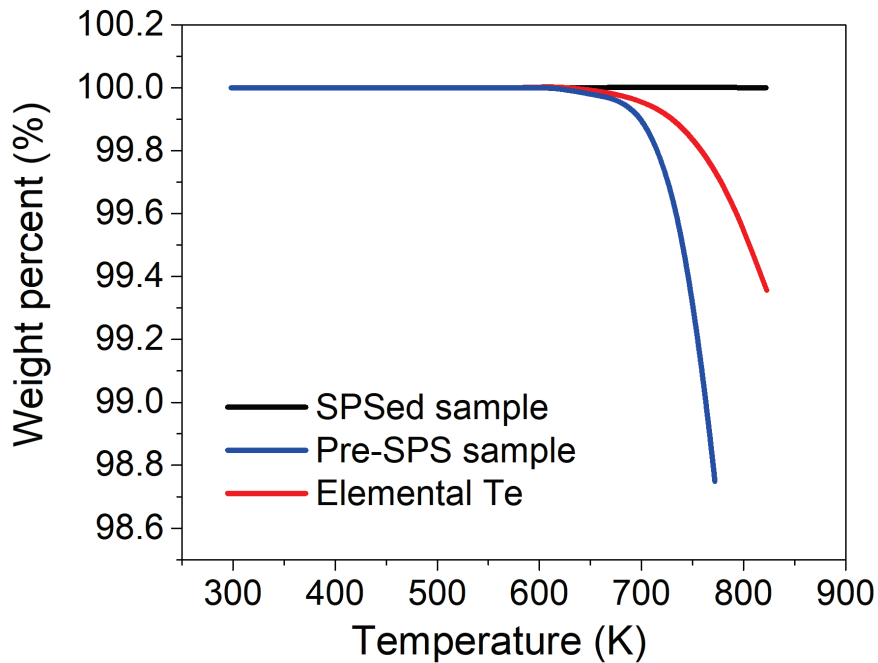


Figure 3. 5. Thermogravimetric analysis (TGA) data demonstrate the phase homogeneity and thermal stability of the SPS $\text{Cu}_{0.06}\text{Bi}_2\text{Te}_{3.17}$ sample. The control $\text{Cu}_{0.06}\text{Bi}_2\text{Te}_{3.17}$ ingot sample shows a weight loss around 680 K due to the evaporation of excess tellurium, as confirmed by the thermal behavior of elemental tellurium (melting point of Te ~ 720 K).

3.3.2 Microstructure

Representative scanning electron microscope (SEM) image of the SPS $\text{Cu}_{0.06}\text{Bi}_2\text{Te}_{3.17}$ sample shows a highly oriented lamellar morphology. (Figure 3. 6). We examined the polished surface of SPS $\text{Cu}_{0.06}\text{Bi}_2\text{Te}_{3.17}$ and its control $\text{Cu}_{0.06}\text{Bi}_2\text{Te}_{3.17}$ ingot samples to understand the effect of excess Te and SPS on their quantitative composition and microstructure. The SEM and elemental mapping images on the former demonstrate the homogeneous distribution of the constituent elements with no discernible phase segregation within the detection limit of SEM (Figures 3. 7a–d). In contrast, typical SEM image of the control ingot sample reveals a distinct line feature embedded in the Bi_2Te_3 matrix (Figure 3. 8a). The elemental maps taken on the rectangular region reveal that those lines consist of Cu and Te devoid of Bi atom (Figure 3. 8b–d), which is consistent with the result of the PXRD pattern showing the presence of CuTe secondary phase.

It is important to note that the results of PXRD, SEM, and EDS clearly demonstrate the uniqueness of the synthesis method in this work for stabilizing n-type Bi_2Te_3 compounds with the high extent of Cu doping. Excess Cu and Te cannot be fully dissolved in the Bi_2Te_3 structure by solid-state reaction. Post-SPS process ejects most of excess Te out of the resulting dense pellets, instead maintaining Cu atoms in the Bi_2Te_3 structure. As a result, SPS $\text{Cu}_{0.06}\text{Bi}_2\text{Te}_{3.17}$ behaves as single phase, and exhibits unusual TE

properties as discussed later. This finding implies that a combination of highly off-stoichiometric reaction melt and SPS can promise rich chemistry in stabilizing unusual compositions for unpredicted physical and chemical properties, which is unavailable by conventional reaction pathways.

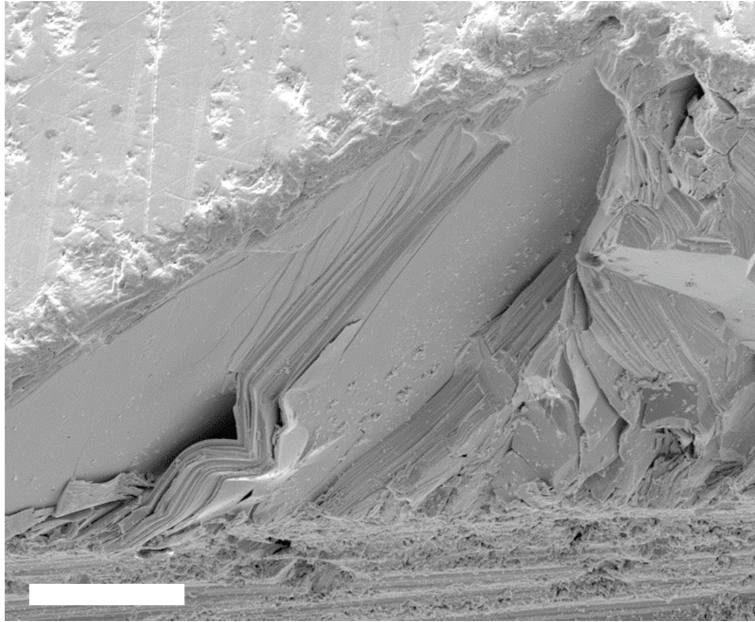


Figure 3. 6. Typical SEM image of the SPS $\text{Cu}_{0.06}\text{Bi}_2\text{Te}_{3.17}$ sample showing the highly oriented lamellar morphology. Scale bar: 100 μm .

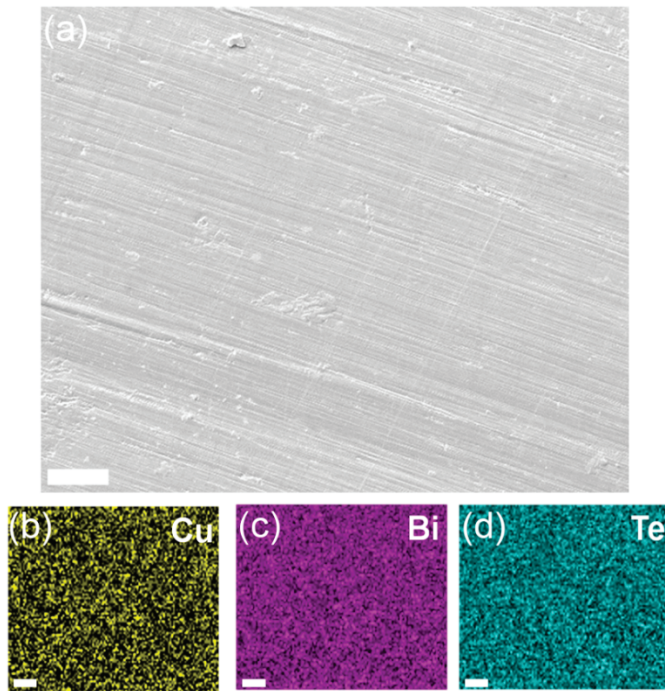


Figure 3. 7. (a) Typical SEM image and (b–d) EDS elemental maps for (b) Cu, (c) Bi, and (d) Te atoms on the polished surface of the SPS $\text{Cu}_{0.06}\text{Bi}_2\text{Te}_{3.17}$ sample show the homogeneous distribution of the constituent elements without phase segregation. White scale bar corresponds to 50 μm .

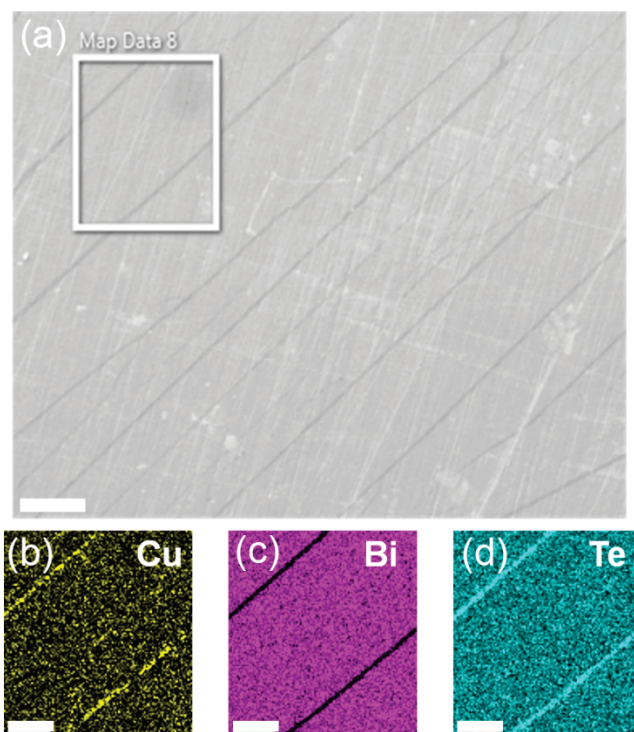


Figure 3. 8. (a) Typical SEM image of the control ingot $\text{Cu}_{0.06}\text{Bi}_2\text{Te}_{3.17}$ sample and EDS elemental maps (b-d) taken at the rectangular region in (a) reveal that the line features, consisting of Cu and Te and being absent of Bi atoms, are embedded in the Bi_2Te_3 matrix. White scale bar corresponds to 50 μm .

3.3.3 Charge Transport Properties

We compared thermoelectric (TE) properties of the title SPS $\text{Cu}_x\text{Bi}_2\text{Te}_{3.17}$ ($x = 0.02, 0.04, \text{ and } 0.06$) samples with the control samples of as-grown $\text{Cu}_x\text{Bi}_2\text{Te}_{3.17}$ ingots and SPS $\text{Cu}_x\text{Bi}_2\text{Te}_3$. Note that both the SPS $\text{Cu}_x\text{Bi}_2\text{Te}_{3.17}$ and $\text{Cu}_x\text{Bi}_2\text{Te}_3$ samples have nearly the same analyzed composition “ $\text{Cu}_x\text{Bi}_2\text{Te}_3$ ”. Because of the layered structure and resulting highly anisotropic TE properties of Bi_2Te_3 -based materials,³⁸ all SPS samples were measured perpendicular to the SPS press direction. The control as-grown $\text{Cu}_{0.06}\text{Bi}_2\text{Te}_{3.17}$ ingot exhibits positive Seebeck coefficient (S) values over the entire temperature range, indicative of p-type conduction possibly due to the presence of p-type conductor CuTe ⁵¹ as secondary phase (Figure 3. 9a). This observation is consistent with the previous report that Bi_2Te_3 with CuTe and Te impurities shows p-type conduction.⁴⁹

In striking contrast, the SPS $\text{Cu}_x\text{Bi}_2\text{Te}_{3.17}$ and the other control SPS $\text{Cu}_x\text{Bi}_2\text{Te}_3$ samples display negative S values in the full temperature range, showing n-type conduction (Figure 3. 10a). A magnitude of S ($|S|$) for the former reaches a peak at 323 K with a maximum of $\sim 230 \mu\text{V K}^{-1}$ for the $x = 0.06$ sample and decreases afterward, whereas that of the latter steadily declines with the increasing temperature. The diminishing $|S|$ at high temperature is attributed to the excitation of minor carriers, known as bipolar effect, because of the inverse relationship between $|S|$ and carrier

concentration. We theoretically plot the Pisarenko relation between S and carrier concentration (n_H) at room temperature (black line) based on a single parabolic band (SPB) model assuming acoustic phonon scattering mechanism (Figure 3. 10b).³⁶ The S values of SPS $\text{Cu}_x\text{Bi}_2\text{Te}_{3.17}$ samples fall near the theoretical Pisarenko line with an effective mass of $\sim 1.0 m_e$, indicating that Cu doping does not affect the conduction band near the Fermi level.

Remarkably, the Hall effect measurement at room temperature shows that both Hall carrier concentration (n_H) and mobility (μ_H) of the SPS $\text{Cu}_x\text{Bi}_2\text{Te}_{3.17}$ samples increase with the higher content of Cu (Figures 3. 10c and d). This observation is contrary to the general understanding that n_H and μ_H are inversely proportional with each other because of the carrier scattering mechanism. For SPS $\text{Cu}_x\text{Bi}_2\text{Te}_{3.17}$, n_H increases from $\sim 9.35 \times 10^{18}$ to $\sim 1.20 \times 10^{19} \text{ cm}^{-3}$ for the $x = 0.02$ and 0.06 samples, respectively. The corresponding μ_H improves from $\sim 442 \text{ cm}^2$ to $\sim 467 \text{ cm}^2 \text{ V}^{-1} \text{ s}^{-1}$, which is the highest reported to date among all polycrystalline n-type Bi_2Te_3 -based compounds. In contrast, n_H for control SPS $\text{Cu}_x\text{Bi}_2\text{Te}_3$ samples decreases with the increasing Cu amount, indicating that Cu serves as an electron acceptor (Figure 3. 11a). The corresponding μ_H is also considerably lower than that of SPS $\text{Cu}_x\text{Bi}_2\text{Te}_{3.17}$ samples. These results clearly show that

excess Te condition brings about the simultaneous enhancement in n_H and μ_H (Figure 3. 11b).

The achieved ultrahigh μ_H can arise from the simultaneous contribution from three factors. First, excess Te in the reaction mixture can reduce carrier scattering to enhance μ_H because low-melting excess Te may act as a ‘lubricant’ so that Bi_2Te_3 lamella grains may reorient to form better aligned and packed textures along the *ab*-planes during SPS under high temperature and pressure as similarly observed in the previous report.⁴⁰ Second, excess Te in the reaction mixture can suppress the generation of adverse Te vacancies (V_{Te}), thereby helping to maintain n_H at the optimal level to achieve ultrahigh μ_H . Otherwise, too high n_H could deteriorate μ_H due to carrier scattering and simultaneously reduce S because of the inverse proportionality between S and n_H . In contrast, SPS pristine Bi_2Te_3 exhibits considerably large $n_H \sim 4.79 \times 10^{19} \text{ cm}^{-3}$ and resultantly lowered $\mu_H \sim 164 \text{ cm}^2$ at room temperature. Third, Cu cations at van der Waals gaps between the Bi_2Te_3 layers can improve electrons transfer across them, consequently mitigating interface scatterings and increasing μ_H .⁴¹

We calculated μ_H for the SPS $\text{Cu}_x\text{Bi}_2\text{Te}_{3.17}$ samples with respect to n_H at room temperature based on a SPB model assuming acoustic phonon scattering (See Supporting Information for the details) (Figure 3. 12).¹⁴

Experimental μ_H of poly- and single crystalline Bi_2Te_3 ⁵² and $\text{Cu}_{0.01}\text{Bi}_2\text{Te}_{2.7}\text{Se}_{0.3}$ ⁴¹ from the previous reports fall near the calculated curve. In contrast, μ_H of SPS $\text{Cu}_x\text{Bi}_2\text{Te}_{3.17}$ is much larger than the theoretical prediction, displaying the markedly boosted μ_H in comparison with other Cu doped Bi_2Te_3 -based materials.^{41, 47}

We performed the temperature-dependent Hall effect measurements for the SPS $\text{Cu}_{0.06}\text{Bi}_2\text{Te}_{3.17}$ sample to better understand its ultrahigh μ_H and carrier scattering mechanism (Figure 3. 13). n_H gradually increases from $\sim 1.2 \times 10^{19}$ to $3.3 \times 10^{19} \text{ cm}^{-3}$ in the 298–473 K temperature range. The resulting temperature-dependent Hall coefficients $R_H = 1 / n_H e$, where e is the electron charge, are given in Figure 3. 14. The corresponding μ_H decreases from ~ 468 to $180 \text{ cm}^2 \text{ V}^{-1} \text{ s}^{-1}$ (Figure 3. 13b), consistent with their inversely proportional relationship. A temperature-dependent $\log(\mu_H)$ – $\log(T)$ plot shows complex scattering mechanisms in SPS $\text{Cu}_{0.06}\text{Bi}_2\text{Te}_{3.17}$ (Figure 3. 13c). From 323 to 373 K, the slopes of the curves are ~ -1.5 , indicating that scattering mechanism is dominated by acoustic phonon scattering if parabolic bands are assumed. It corresponds to electron-phonon scattering due to thermal lattice vibrations.⁵³ From 398 to 473 K, the slopes increase to ~ -1.8 . The slightly steeper slope at higher temperature probably results from nonparabolic bands, electron-electron scattering, and/or optical phonon

scattering due to lattice vibrations with high frequency.⁵⁴⁻⁵⁵ The similar reasons could be applied to the μ_H at 298 K that slightly deviates from the slope of -1.8 .

The temperature-dependent electrical conductivity (σ) of the SPS $\text{Cu}_x\text{Bi}_2\text{Te}_{3.17}$ samples increases significantly with the higher mole fraction of Cu doping (Figure 3. 15a). This observation results from the concurrently raised n_H and μ_H with the increasing concentration of Cu as well as the higher μ_H itself than the theoretical expectation. For instance, the σ rises from $\sim 665 \text{ S cm}^{-1}$ for $\text{Cu}_{0.02}\text{Bi}_2\text{Te}_{3.17}$ to $\sim 900 \text{ S cm}^{-1}$ for $\text{Cu}_{0.06}\text{Bi}_2\text{Te}_{3.17}$ at room temperature, indicating that Cu serves as an electron donor. In contrary, the σ of the control SPS $\text{Cu}_x\text{Bi}_2\text{Te}_3$ samples decreases considerably with the larger extent of Cu, for example, $\sim 590 \text{ S cm}^{-1}$ for $\text{Cu}_{0.02}\text{Bi}_2\text{Te}_3$ to $\sim 235 \text{ S cm}^{-1}$ for $\text{Cu}_{0.04}\text{Bi}_2\text{Te}_3$. It is consistent with the Hall effect measurement results for the control SPS $\text{Cu}_x\text{Bi}_2\text{Te}_3$ samples that both n_H and μ_H decrease with the increasing Cu amount (Figure 3. 11). This observation verifies the unique role of excess Te in the reaction mixture for charge transport properties in that the analysed EDS composition of SPS $\text{Cu}_x\text{Bi}_2\text{Te}_{3.17}$ and SPS $\text{Cu}_x\text{Bi}_2\text{Te}_3$ is almost the same to be “ $\text{Cu}_x\text{Bi}_2\text{Te}_3$ ”.

The $x = 0.06$ sample shows much higher σ and even slightly larger $|\mathcal{S}|$ than the other members in SPS $\text{Cu}_x\text{Bi}_2\text{Te}_{3.17}$, contrary to the general inverse

relationship between σ and $|S|$. This simultaneous enhancement leads to ultrahigh power factor (PF) for $\text{Cu}_{0.06}\text{Bi}_2\text{Te}_{3.17}$, exhibiting a maximum $\sim 45 \mu\text{W cm}^{-1} \text{K}^{-2}$ at room temperature, which is ~ 1.5 times larger than that of $\text{Cu}_{0.02}\text{Bi}_2\text{Te}_{3.17}$ (Figure 3. 15b). The achieved PF is the highest reported to date among bulk polycrystalline n-type Bi_2Te_3 -based materials (Figure 3. 15c).^{41, 47} Remarkably, polycrystalline SPS $\text{Cu}_{0.06}\text{Bi}_2\text{Te}_{3.17}$ displays even higher PF than single crystal $\text{Cu}_{0.07}\text{Bi}_2\text{Te}_3$ ⁴⁷ in the previous report despite their similar actual composition. The samples with $x = 0.08$ and 0.10 , which do not include secondary phase, show lower PF than that with $x = 0.06$ (Figure 3. 16).

Since a large amount of Cu atom is introduced into the Bi_2Te_3 lattices, the chemical stability of the sample under a large current is very important for practical TE applications. Figure 3. 17 shows a relative resistance of R/R_0 , where R_0 is an initial resistance of the sample, for the SPS $\text{Cu}_{0.06}\text{Bi}_2\text{Te}_{3.17}$ sample under a current density of 12 A cm^{-2} as a function of time. It is a typical stability test condition for superionic TE materials containing a large extent of highly mobile Cu or Ag atoms.⁵⁶ The R/R_0 value is nearly unchanged after about $50,000 \text{ s}$ (14 h), demonstrating the chemical robustness of the SPS $\text{Cu}_{0.06}\text{Bi}_2\text{Te}_{3.17}$ sample under a high current environment.

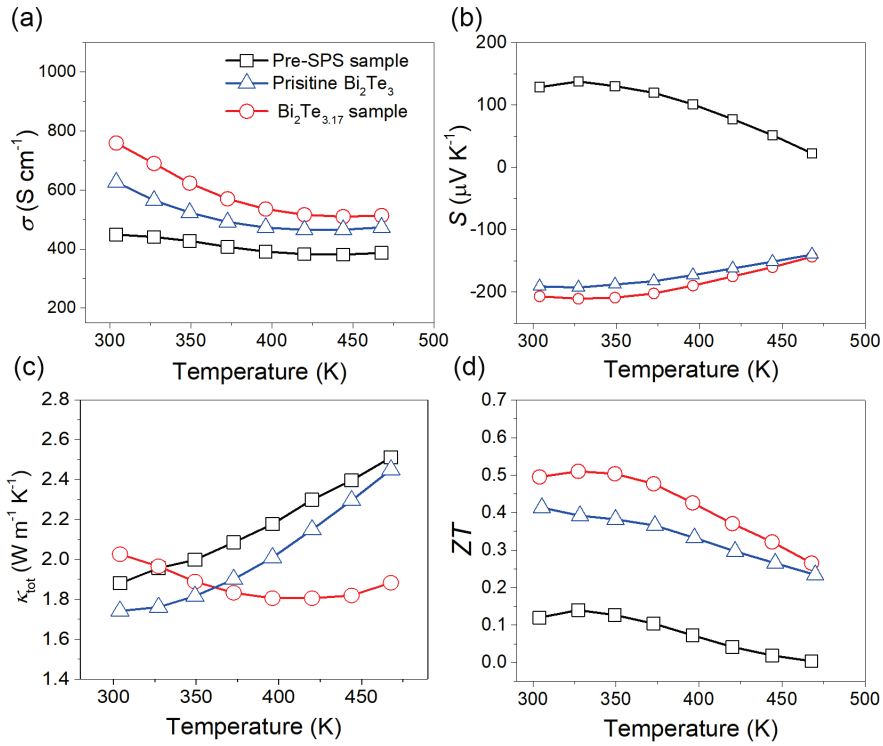


Figure 3. 9. Temperature dependence of (a) electrical conductivity, (b) Seebeck coefficient, (c) total thermal conductivity, and (d) thermoelectric figure of merit (ZT) for the control $\text{Cu}_{0.06}\text{Bi}_2\text{Te}_{3.17}$ ingot sample. Note that the control ingot sample shows p-type conduction. The corresponding data for pristine Bi_2Te_3 sample, which is similarly prepared to the other samples, are given for comparison.

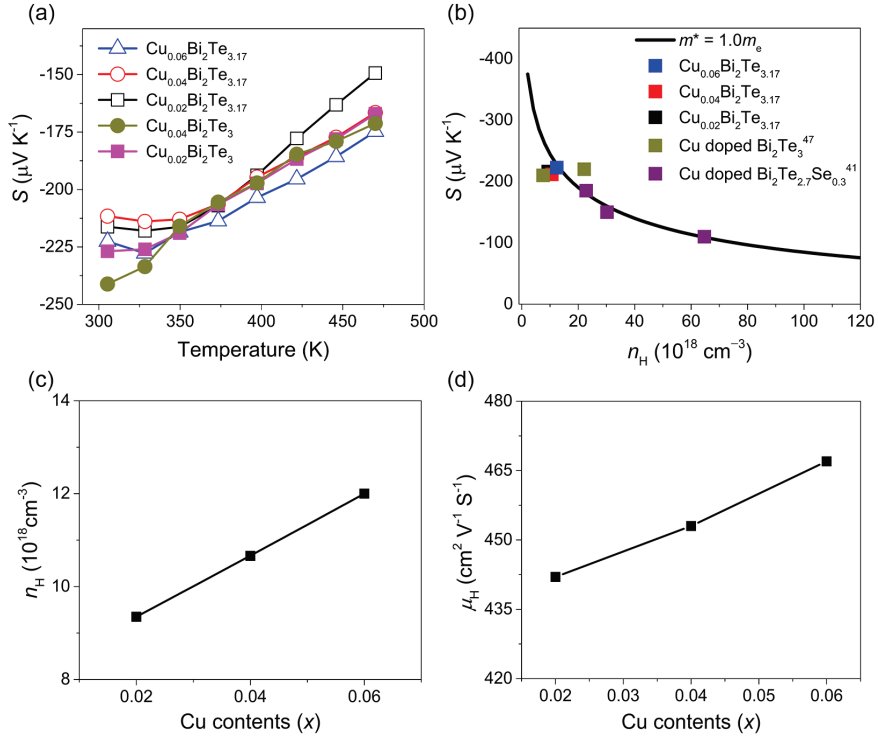


Figure 3. 10. Charge transport properties for the SPS $\text{Cu}_x\text{Bi}_2\text{Te}_{3.17}$ samples measured perpendicular to the SPS press direction. (a) Temperature dependence of the Seebeck coefficient in comparison with that of the control SPS $\text{Cu}_x\text{Bi}_2\text{Te}_3$ samples. (b) The Pisarenko relation based on a single parabolic band (SPB) model at room temperature. The reported experimental data for Cu-doped Bi_2Te_3 -based materials are given for comparison.^{41, 47} (c) Hall-effect charge-carrier concentration and (d) Hall mobility with respect to the Cu concentration at room temperature. Note that the nominal composition of samples are given in the panels.

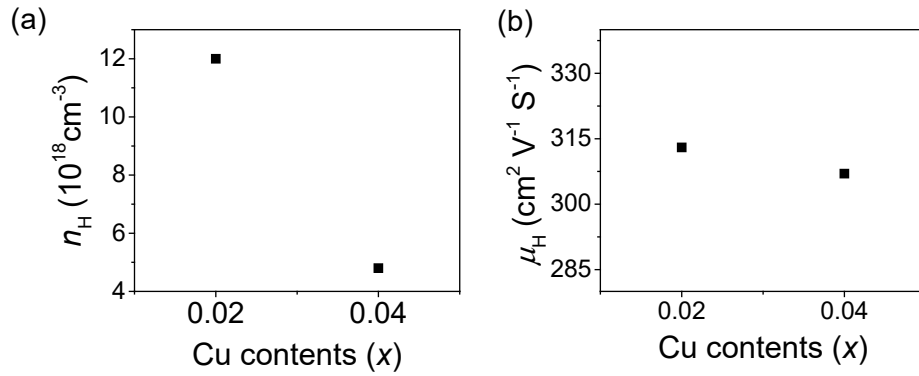


Figure 3. 11. (a) The Hall carrier concentration (n_H) and (b) the Hall mobility (μ_H) at room temperature for control SPS Cu_{*x*}Bi₂Te₃ samples measured perpendicular to the press direction.

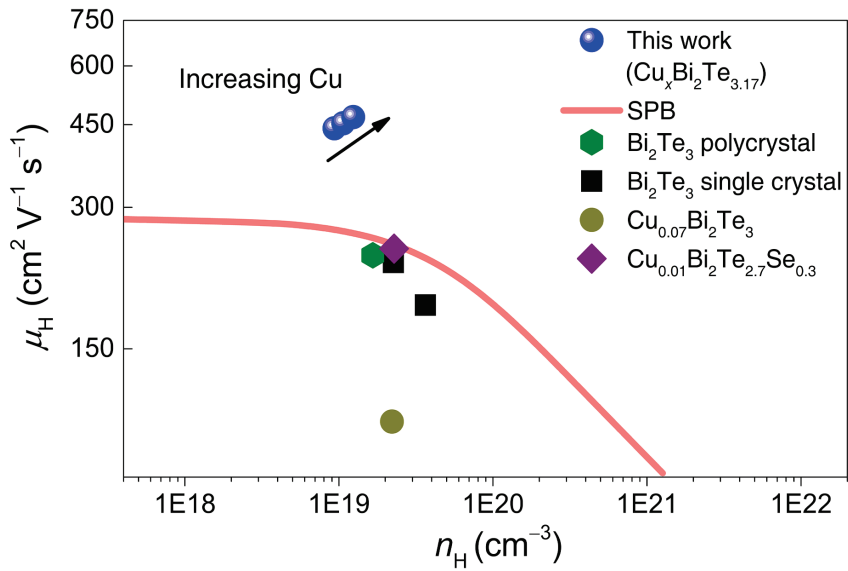


Figure 3. 12. Calculated μ_H with respect to n_H (solid lines) assuming acoustic phonon scattering. Experimental values for SPS $\text{Cu}_x\text{Bi}_2\text{Te}_{3.17}$ samples at room temperature are much higher than the theoretical prediction and increase with the higher concentration of Cu. Experimental data for single-crystal Bi_2Te_3 ,⁵² polycrystalline $\text{Cu}_{0.07}\text{Bi}_2\text{Te}_3$,⁴⁷ and polycrystalline $\text{Cu}_{0.01}\text{Bi}_2\text{Te}_{2.7}\text{Se}_{0.3}$ ⁴¹ from previous reports are also given for comparison.

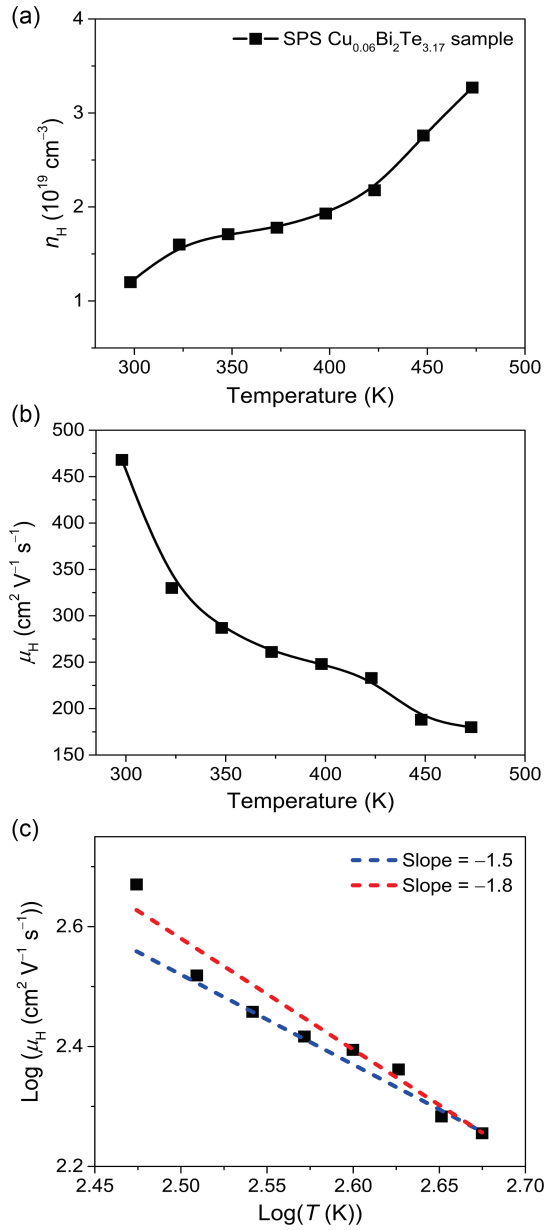


Figure 3. 13. Temperature-dependence of (a) n_H and (b) μ_H for the SPS $\text{Cu}_{0.06}\text{Bi}_2\text{Te}_{3.17}$ sample. (c) A $\text{log}(\mu_H)\text{--log}(T)$ plot shows different slopes with respect to temperature.

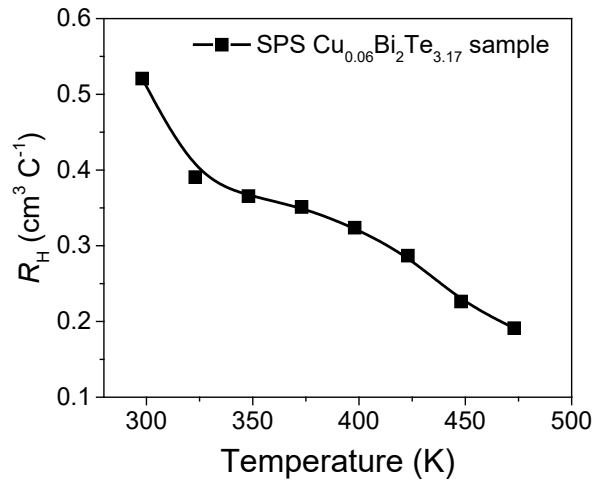


Figure 3. 14. The temperature-dependent Hall coefficient (R_H) for the SPS $\text{Cu}_{0.06}\text{Bi}_2\text{Te}_{3.17}$ sample. The R_H gradually decreases with increasing temperature.

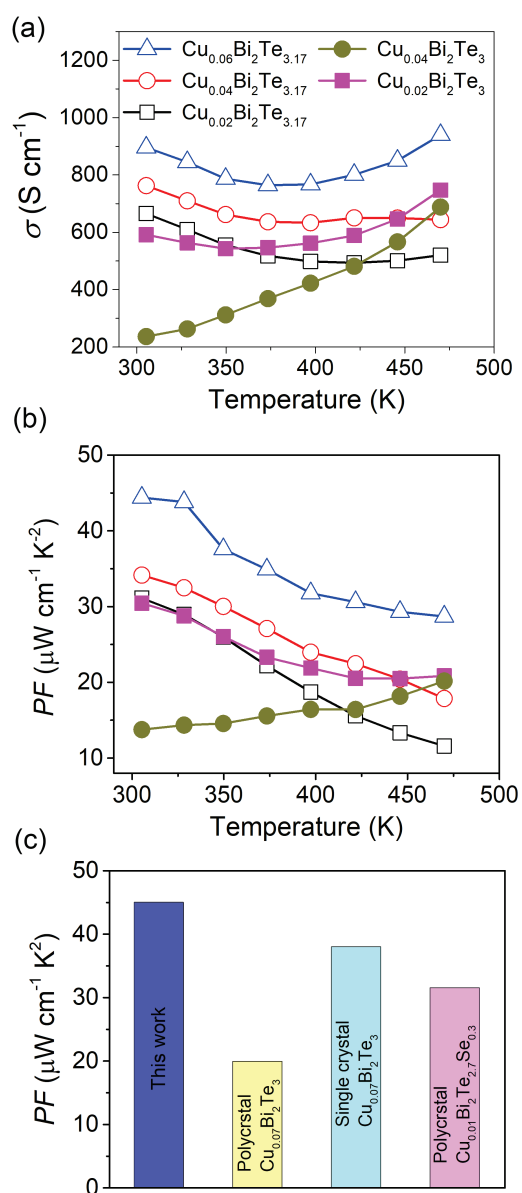


Figure 3. 15. Temperature dependence of (a) electrical conductivity and (b) power factor for the SPS Cu_xBi₂Te_{3.17} samples measured perpendicular to the SPS press direction. (c) Comparison of the power factor achieved in this work with those of the previous reports on Cu-doped Bi₂Te₃-based compounds.^{41, 47}

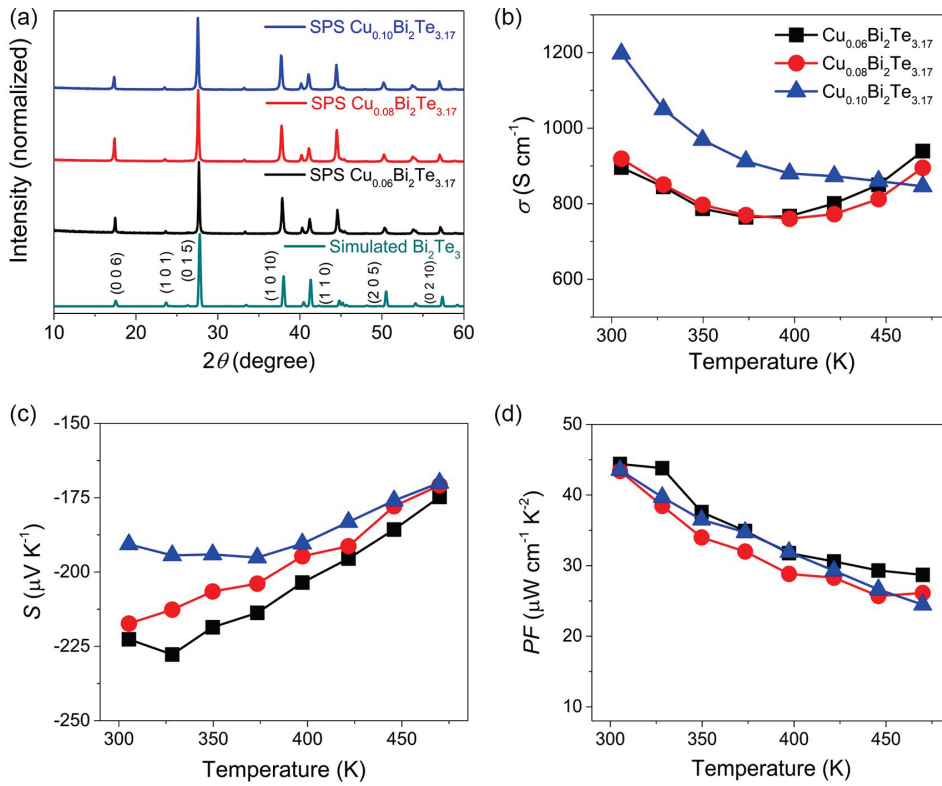


Figure 3. 16. (a) Powder XRD patterns for the SPS $\text{Cu}_x\text{Bi}_2\text{Te}_3$ ($x = 0.06, 0.08$ and 0.10) samples. Temperature dependence of (b) electrical conductivity, (c) Seebeck coefficient, and (d) power factor for the SPS $\text{Cu}_x\text{Bi}_2\text{Te}_{3.17}$ samples measured perpendicular to the SPS press direction.

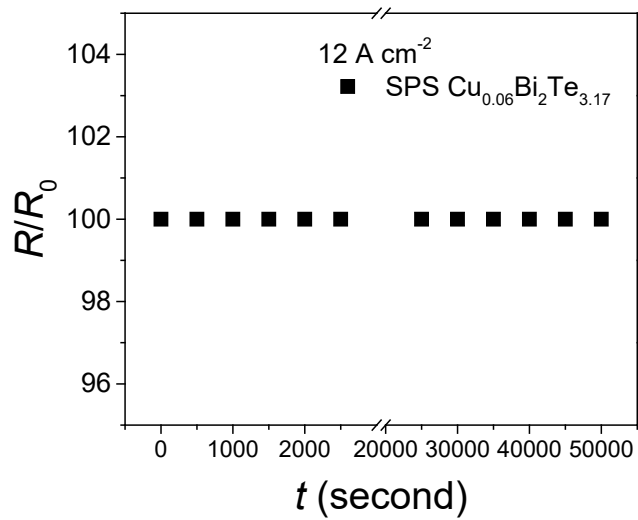


Figure 3. 17. The relative electrical resistance with respect to time for the SPS Cu_{0.06}Bi₂Te_{3.17} sample under the current density of 12 A cm⁻² at room temperature, demonstrating the high stability of this material under a large current flow.

3.3.4 Thermal conductivity

The total thermal conductivity (κ_{tot}) for both the SPS $\text{Cu}_x\text{Bi}_2\text{Te}_{3.17}$ and control SPS $\text{Cu}_x\text{Bi}_2\text{Te}_3$ samples increases with the rising temperature (Figure 3. 18a). The former shows lower κ_{tot} than the latter near ambient temperature. For example, the κ_{tot} at room temperature increases from $\sim 1.60 \text{ W m}^{-1} \text{ K}^{-1}$ for the SPS $\text{Cu}_{0.04}\text{Bi}_2\text{Te}_{3.17}$ to $\sim 1.85 \text{ W m}^{-1} \text{ K}^{-1}$ for the control SPS $\text{Cu}_{0.04}\text{Bi}_2\text{Te}_3$. The κ_{tot} of SPS $\text{Cu}_x\text{Bi}_2\text{Te}_{3.17}$ samples increases with the higher extent of Cu over the entire temperature range. Because κ_{tot} is contributed from charge carriers (κ_{ele}), lattice phonons (κ_{lat}), and bipolar conduction (κ_{bip}), examining their portion to κ_{tot} can reveal the effect of Cu doping and excess Te in the reaction mixture on thermal transport of the materials. κ_{ele} is expressed by the formula $\kappa_{\text{ele}} = L\sigma T$, where L is the Lorentz number, σ is the electrical conductivity, and T is the absolute temperature. κ_{lat} can be obtained by the Wiedemann-Franz formula $\kappa_{\text{lat}} = \kappa_{\text{tot}} - \kappa_{\text{ele}}$ (see Supporting Information for the details). The κ_{ele} of SPS $\text{Cu}_x\text{Bi}_2\text{Te}_{3.17}$ samples rises with the increasing content of Cu, indicating Cu atoms serve as an electron donor. This result is consistent with the trend of μ_{H} and σ (Figure 3. 18b). The κ_{lat} for the SPS $\text{Cu}_x\text{Bi}_2\text{Te}_{3.17}$ samples are comparable regardless of the Cu concentration and significantly lower than those of the control $\text{Cu}_x\text{Bi}_2\text{Te}_3$ samples up to $\sim 423 \text{ K}$, implying that the excess Te condition mainly determines κ_{lat} of the SPS $\text{Cu}_x\text{Bi}_2\text{Te}_{3.17}$ samples and differentiates it from κ_{lat} of the control SPS

$\text{Cu}_x\text{Bi}_2\text{Te}_3$ (Figure 3. 18c). The effect of point defects by Cu doping is minor in κ_{lat} for SPS $\text{Cu}_x\text{Bi}_2\text{Te}_{3.17}$.

To better understand this observation, we investigated microstructures of SPS $\text{Cu}_{0.06}\text{Bi}_2\text{Te}_{3.17}$ specimen using a transmission electron microscope (TEM). Figures 3. 19a – b show typical low-magnification TEM images. Line features with a different contrast are embedded in the matrix, revealing the presence of a high density of dislocation arrays. The selected area electron diffraction (SAED) pattern, which includes both the matrix and dislocation regions, shows a single set of spots corresponding to the Bi_2Te_3 structure along the [001] zone axis without any noticeable second phase (inset, Figure 3. 19b). High-resolution TEM and the corresponding inverse fast Fourier transform (IFFT) images clearly display edge dislocations marked by red symbols (Figures 3. 19c and d). An average density of dislocations is estimated to be $\sim 2 \times 10^{12} \text{ cm}^{-2}$ from the TEM image, which is much higher than $\sim 10^9$ and $10^3\text{--}10^6 \text{ cm}^{-2}$ observed in pristine Bi_2Te_3 ⁵⁷ and typical semiconductors,⁵⁸ respectively. The similar observation was also previously reported that a high density of dislocations is generated via squeezing excess Te out of the Bi_2Te_3 -based lattices by SPS under pressure, leading to the significant reduction in κ_{lat} .⁴⁰ Note that dense dislocations have been established as highly effective phonon scattering mechanism over others.⁵⁹

We theoretically calculated the temperature-dependent κ_{lat} for SPS

$\text{Cu}_{0.06}\text{Bi}_2\text{Te}_{3.17}$ using Debye–Callaway model (see Supporting Information for the details). According to our TEM observation, we considered various scattering mechanisms such as intrinsic Umklapp process, grain boundaries, point defects, and dislocations based on the Matthiessen’s equation.⁶⁰ Because bipolar conduction from minor carriers is important for narrow band gap semiconductor such as Bi_2Te_3 and PbTe , we also obtained bipolar thermal conductivity (κ_{bip}) to accurately calculate κ_{lat} (Figure 3. 20a).⁶¹ The theoretical κ_{bip} rapidly grows with the increasing temperature, as observed in κ_{tot} (Figure 3.18a), indicating that κ_{bip} mainly contributes to κ_{tot} at high temperature. The theoretical κ_{lat} based on phonon scattering mechanisms of Umklapp process, grain boundary, and point defect is much higher than the experimental values (Figure 3. 20b). The further consideration of high-density dislocations found in the TEM study greatly improves the agreement between the theoretical and experimental κ_{lat} , clearly demonstrating their major role in κ_{lat} . Overall, point defects by Cu doping and dense dislocations induced by excess Te synergistically reduce κ_{lat} . However, a degree of decrease in κ_{lat} is not significant in comparison with other representative bulk TE materials with dense dislocations.^{40, 59, 62} The enhanced PF and simultaneously reduced κ_{tot} lead to relatively high $ZT \sim 0.85$ for the SPS $\text{Cu}_{0.06}\text{Bi}_2\text{Te}_{3.17}$ sample (Figure 3. 18d). There are more rooms to improve ZT of SPS $\text{Cu}_x\text{Bi}_2\text{Te}_{3.17}$ system by developing strategies of further reducing κ_{lat} with a minimal influence on

powder factor, given its much higher κ_{lat} than the state-of-the-art n-type Bi_2Te_3 -based materials.

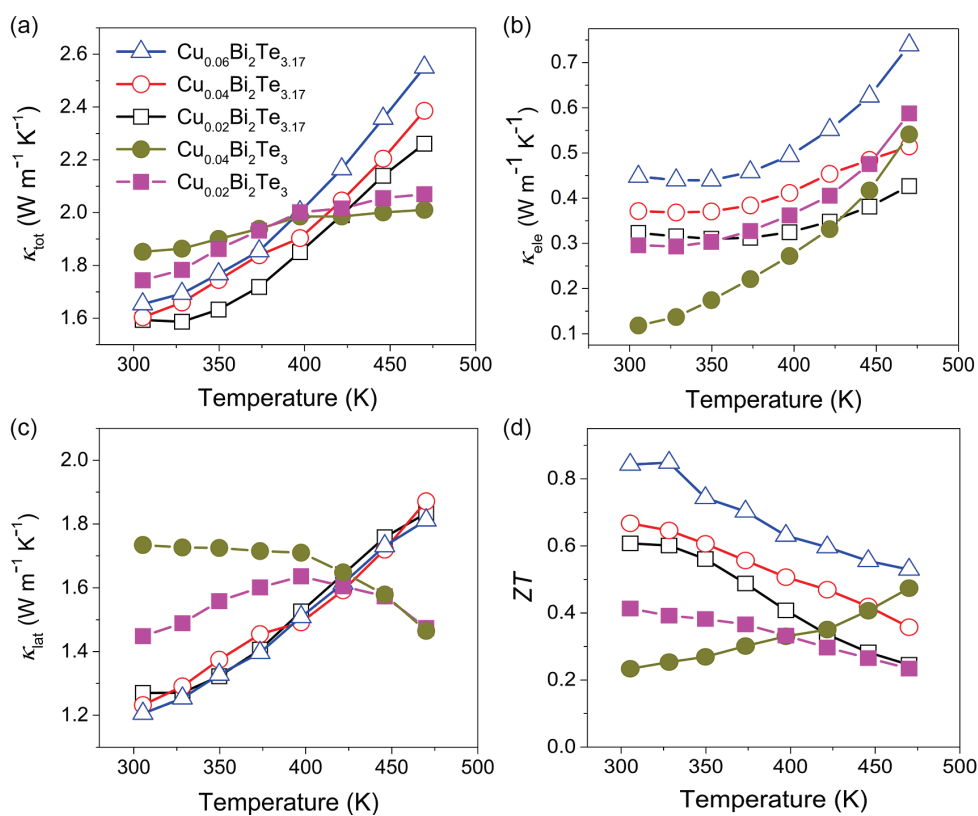


Figure 3. 18. Temperature dependence of (a) total, (b) electrical, and (c) lattice thermal conductivity. (d) Figure of merit ZT for the SPS $\text{Cu}_x\text{Bi}_2\text{Te}_{3.17}$ and control SPS $\text{Cu}_x\text{Bi}_2\text{Te}_3$ samples, measured perpendicular to the SPS press direction.

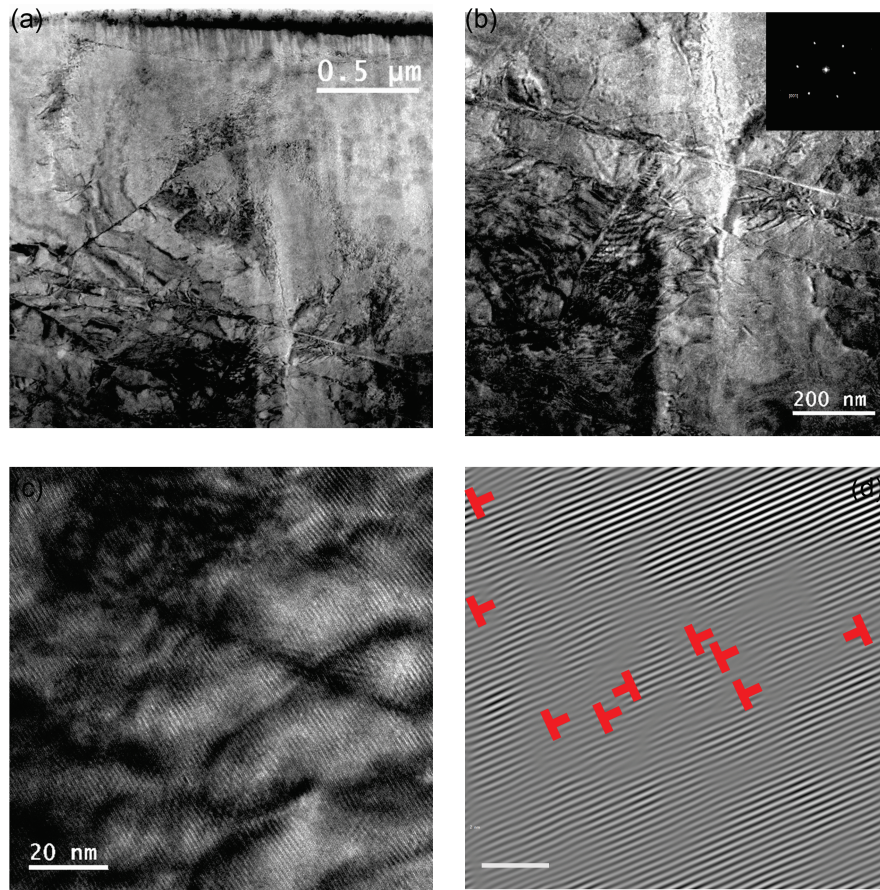


Figure 3. 19. (a, b) Typical low-magnification TEM images of SPS $\text{Cu}_{0.06}\text{Bi}_2\text{Te}_{3.17}$ specimen showing dislocations with a density of $\sim 2 \times 10^{12} \text{ cm}^{-2}$ embedded in the matrix. Inset of (b) shows the selected area electron diffraction pattern along the [001] zone axis, which is taken on the entire area of (b) that includes both the matrix and dislocations. (c) High-resolution TEM image taken on dislocations. (d) The corresponding inverse fast Fourier transform (IFFT) image indicates the presence of edge dislocations, indicated by red symbols.

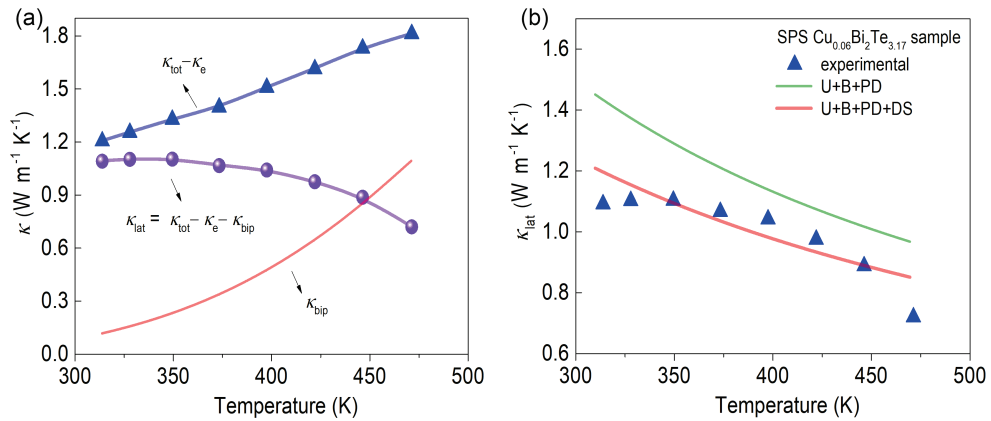


Figure 3. 20. (a) The calculated temperature-dependent bipolar (κ_{bip}) and lattice thermal conductivity (κ_{lat}). (b) The Comparison of experimental (triangles) and calculated κ_{lat} considering Umklapp (U), grain boundary (B), point defect (PD), and dislocation (DS) scattering processes using a Callaway-Debye model (solid line) for the SPS $\text{Cu}_{0.06}\text{Bi}_2\text{Te}_{3.17}$ sample.

3.4 Conclusion

We introduced new high performance n-type Bi₂Te₃-based thermoelectric materials with ultrahigh electron mobility and power factor. These specialize in maximizing power factor for high output power thermoelectric generators operating near ambient temperature. With this new system, both the n- and p-type Bi₂Te₃-based materials eventually show a similar maximum power factor value $\sim 45 \mu\text{W cm}^{-1} \text{K}^{-2}$ around room temperature. Accordingly, the thermoelectric devices comprising their couples can promise maximized output power although there are many other components that have to be advanced in thermoelectric device structure, for example, electrodes, metallization layers, and contact wires. Our new synthetic method widens the availability of chemical compositions to enhance thermoelectric properties, which is otherwise strictly governed by thermodynamic phase diagrams. This synthesis concept can be widely applied to other chemical systems for various technological applications.

3.5 References

- [1] Lewis, N. S.; Nocera, D. G. Powering The Planet: Chemical Challenges in Solar Energy Utilization. *Proc. Natl. Acad. Sci. U. S. A.* **2006**, *103*, 15729-15735.
- [2] Gingerich, D. B.; Mauter, M. S. Quantity, Quality, and Availability of Waste Heat from United States Thermal Power Generation. *Environ. Sci. Technol.* **2015**, *49*, 8297-8306.
- [3] Tan, G.; Zhao, L.-D.; Kanatzidis, M. G. Rationally Designing High-Performance Bulk Thermoelectric Materials. *Chem. Rev.* **2016**, *116*, 12123-12149.
- [4] Jana, M. K.; Pal, K.; Warankar, A.; Mandal, P.; Waghmare, U. V.; Biswas, K. Intrinsic Rattler-Induced Low Thermal Conductivity in Zintl Type TlInTe_2 . *J. Am. Chem. Soc.* **2017**, *139*, 4350-4353.
- [5] Banik, A.; Shenoy, U. S.; Saha, S.; Waghmare, U. V.; Biswas, K. High Power Factor and Enhanced Thermoelectric Performance of SnTe-AgInTe_2 : Synergistic Effect of Resonance Level and Valence Band Convergence. *J. Am. Chem. Soc.* **2016**, *138*, 13068-13075.
- [6] Fu, C.; Bai, S.; Liu, Y.; Tang, Y.; Chen, L.; Zhao, X.; Zhu, T. Realizing High Figure of Merit in Heavy-Band p-Type Half-Heusler Thermoelectric Materials. *Nat. Commun.* **2015**, *6*, 8144.
- [7] Shi, Y.; Assoud, A.; Ponou, S.; Lidin, S.; Kleinke, H. A New Material

with a Composite Crystal Structure Causing Ultralow Thermal Conductivity and Outstanding Thermoelectric Properties: $\text{Tl}_2\text{Ag}_{12}\text{Te}_{7+\delta}$. *J. Am. Chem. Soc.* **2018**, *140*, 8578-8585.

[8] Shuai, J.; Ge, B.; Mao, J.; Song, S.; Wang, Y.; Ren, Z. Significant Role of Mg Stoichiometry in Designing High Thermoelectric Performance for $\text{Mg}_3(\text{Sb,Bi})_2$ -Based n-Type Zintl. *J. Am. Chem. Soc.* **2018**, *140*, 1910-1915.

[9] Zeier, W. G.; Zevalkink, A.; Gibbs, Z. M.; Hautier, G.; Kanatzidis, M. G.; Snyder, G. J. Thinking Like a Chemist: Intuition in Thermoelectric Materials. *Angew. Chem. Int. Ed.* **2016**, *55*, 6826-6841.

[10] Kanatzidis, M. G. Nanostructured Thermoelectrics: The New Paradigm? *Chem. Mater.* **2010**, *22*, 648-659.

[11] Sootsman, J. R.; Chung, D. Y.; Kanatzidis, M. G. New and Old Concepts in Thermoelectric Materials. *Angew. Chem. Int. Ed.* **2009**, *48*, 8616-8639.

[12] Zhao, L.-D.; Dravid, V. P.; Kanatzidis, M. G. The Panoscopic Approach to High Performance Thermoelectrics. *Energy Environ. Sci.* **2014**, *7*, 251-268.

[13] Samanta, M.; Pal, K.; Pal, P.; Waghmare, U. V.; Biswas, K. Localized Vibrations of Bi Bilayer Leading to Ultralow Lattice Thermal Conductivity and High Thermoelectric Performance in Weak Topological Insulator n-Type BiSe. *J. Am. Chem. Soc.* **2018**, *140*, 5866-5872.

[14] Zhou, C.; Yu, Y.; Lee, Y. K.; Cojocaru-Mirédin, O.; Yoo, B.; Cho, S.-P.; Im, J.; Wuttig, M.; Hyeon, T.; Chung, I. High-Performance n-Type PbSe–Cu₂Se Thermoelectrics through Conduction Band Engineering and Phonon Softening. *J. Am. Chem. Soc.* **2018**, *140*, 9282-9290.

[15] Hao, F.; Xing, T.; Qiu, P.; Hu, P.; Wei, T.; Ren, D.; Shi, X.; Chen, L. Enhanced Thermoelectric Performance in n-Type Bi₂Te₃-Based Alloys via Suppressing Intrinsic Excitation. *ACS Appl. Mater. Interfaces* **2018**, *10*, 21372-21380.

[16] Cha, J.; Zhou, C.; Lee, Y. K.; Cho, S.-P.; Chung, I. High Thermoelectric Performance in n-Type Polycrystalline SnSe via Dual Incorporation of Cl and PbSe and Dense Nanostructures. *ACS Appl. Mater. Interfaces* **2019**, *11*, 21645–21654.

[17] Narducci, D. Do We Really Need High Thermoelectric Figures of Merit? A Critical Appraisal to The Power Conversion Efficiency of Thermoelectric Materials. *Appl. Phys. Lett.* **2011**, *99*, 102104.

[18] Liu, W.; Kim, H. S.; Chen, S.; Jie, Q.; Lv, B.; Yao, M.; Ren, Z.; Opeil, C. P.; Wilson, S.; Chu, C.-W.; Ren, Z. n-Type Thermoelectric Material Mg₂Sn_{0.75}Ge_{0.25} for High Power Generation. *Proc. Natl. Acad. Sci. U. S. A.* **2015**, *112*, 3269-3274.

[19] Park, S. H.; Jin, Y.; Cha, J.; Hong, K.; Kim, Y.; Yoon, H.; Yoo, C.-Y.; Chung, I. High-Power-Density Skutterudite-Based Thermoelectric Modules

with Ultralow Contact Resistivity Using Fe–Ni Metallization Layers. *ACS Appl. Energy Mater.* **2018**, *1*, 1603-1611.

[20] Salvador, J. R.; Cho, J. Y.; Ye, Z.; Moczygemba, J. E.; Thompson, A. J.; Sharp, J. W.; Koenig, J. D.; Maloney, R.; Thompson, T.; Sakamoto, J.; Wang, H.; Wereszczak, A. A. Conversion Efficiency of Skutterudite-Based Thermoelectric Modules. *Phys. Chem. Chem. Phys.* **2014**, *16*, 12510-12520.

[21] Ren, W.; Zhu, H.; Zhu, Q.; Saparamadu, U.; He, R.; Liu, Z.; Mao, J.; Wang, C.; Nielsch, K.; Wang, Z.; Ren, Z. Ultrahigh Power Factor in Thermoelectric System Nb_{0.95}M_{0.05}FeSb (M = Hf, Zr, and Ti). *Adv. Sci.* **2018**, *5*, 1800278.

[22] Liu, Z.; Mao, J.; Sui, J.; Ren, Z. High Thermoelectric Performance of α -MgAgSb for Power Generation. *Energy Environ. Sci.*, **2018**, *11*, 23-44.

[23] He, R.; Kraemer, D.; Mao, J.; Zeng, L.; Jie, Q.; Lan, Y.; Li, C.; Shuai, J.; Kim, H.; Liu, Y.; Broido, D.; Chu, C.; Chen, G.; Ren, Z. Achieving High Power Factor and Output Power Density in P-Type Half-Heuslers Nb_{1-x}Ti_xFeSb. *Proc. Natl. Acad. Sci. U. S. A.* **2016**, *113*, 13576-13581.

[24] Meng, Q.; Kong, S.; Huang, Z.; Zhu, Y.; Liu, H.; Lu, X.; Jiang, P. Bao, X. Simultaneous Enhancement in the Power Factor and Thermoelectric Performance of Copper Sulfide by In₂S₃ Doping. *J. Mater. Chem. A* **2016**, *4*, 12624-12629.

[25] Liu, W.; Kim, H. S.; Jie, Q.; Ren, Z. Importance of High Power Factor

in Thermoelectric Materials for Power Generation Application: A Perspective. *Scripta Mater.* **2016**, *111*, 3-9.

[26] Hsu, K. F.; Loo, S.; Guo, F.; Chen, W.; Dyck, J. S.; Uher, C.; Hogan, T.; Polychroniadis, E. K.; Kanatzidis, M. G. Cubic $\text{AgPb}_m\text{SbTe}_{2+m}$: Bulk Thermoelectric Materials with High Figure of Merit. *Science* **2004**, *303*, 818-821.

[27] Biswas, K.; He, J.; Zhang, Q.; Wang, G.; Uher, C.; Dravid, V. P.; Kanatzidis, M. G. Strained Endotaxial Nanostructures with High Thermoelectric Figure of Merit. *Nature Chemistry* **2011**, *3*, 160-166.

[28] Biswas, K.; He, J.; Blum, I. D.; Wu, C.-I.; Hogan, T. P.; Seidman, D. N.; Dravid, V. P.; Kanatzidis, M. G. High-Performance Bulk Thermoelectrics with All-Scale Hierarchical Architectures. *Nature* **2012**, *489*, 414-418.

[29] Zhang, J.; Wu, D.; He, D.; Feng, D.; Yin, M.; Qin, X.; He, J. Extraordinary Thermoelectric Performance Realized in n-Type PbTe through Multiphase Nanostructure Engineering. *Adv. Mater.* **2017**, *29*, 1703148.

[30] Tan, G.; Shi, F.; Hao, S.; Zhao, L.-D.; Chi, H.; Zhang, X.; Uher, C.; Wolverton, C.; Dravid, V. P.; Kanatzidis, M. G. Non-Equilibrium Processing Leads to Record High Thermoelectric Figure of Merit in PbTe–SrTe. *Nat. Commun.* **2016**, *7*, 12167.

[31] Pei, Y.; Shi, X.; LaLonde, A.; Wang, H.; Chen, L.; Snyder, G. J. Convergence of Electronic Bands for High Performance Bulk Thermoelectrics. *Nature* **2011**, *473*, 66-69.

[32] Zhao, L. D.; Wu, H. J.; Hao, S. Q.; Wu, C. I.; Zhou, X. Y.; Biswas, K.; He, J. Q.; Hogan, T. P.; Uher, C.; Wolverton, C.; Dravid, V. P.; Kanatzidis, M. G. All-Scale Hierarchical Thermoelectrics: MgTe in PbTe Facilitates Valence Band Convergence and Suppresses Bipolar Thermal Transport for High Performance. *Energy Environ. Sci.* **2013**, *6*, 3346-3355.

[33] Heremans, J. P.; Jovovic, V.; Toberer, E. S.; Saramat, A.; Kurosaki, K.; Charoenphakdee, A.; Yamanaka, S.; Snyder, G. J. Enhancement of Thermoelectric Efficiency in PbTe by Distortion of the Electronic Density of States. *Science* **2008**, *321*, 554-557.

[34] Zhang, Q.; Wang, H.; Liu, W.; Wang, H.; Yu, B.; Zhang, Q.; Tian, Z.; Ni, G.; Lee, S.; Esfarjani, K.; Chen, G.; Ren, Z. Enhancement of Thermoelectric Figure-of-Merit by Resonant States of Aluminium Doping in Lead Selenide. *Energy Environ. Sci.* **2012**, *5*, 5246-5251.

[35] Xiao, Y.; Wu, H.; Cui, J.; Wang, D.; Fu, L.; Zhang, Y.; Chen, Y.; He, J.; Pennycook, S. J.; Zhao, L.-D. Realizing High Performance n-Type PbTe by Synergistically Optimizing Effective Mass and Carrier Mobility and Suppressing Bipolar Thermal Conductivity. *Energy Environ. Sci.* **2018**, *11*, 2486-2495.

[36] Hu, L.; Wu, H.; Zhu, T.; Fu, C.; He, J.; Ying, P.; Zhao, X. Tuning Multiscale Microstructures to Enhance Thermoelectric Performance of n-Type Bismuth-Telluride-Based Solid Solutions. *Adv. Energy Mater.* **2015**, *5*, 1500411.

[37] Hu, L.; Zhu, T.; Liu, X.; Zhao, X. Point Defect Engineering of High-Performance Bismuth-Telluride-Based Thermoelectric Materials. *Adv. Funct. Mater.* **2014**, *24*, 5211-5218.

[38] Poudel, B.; Hao, Q.; Ma, Y.; Lan, Y.; Minnich, A.; Yu, B.; Yan, X.; Wang, D.; Muto, A.; Vashaee, D.; Chen, X.; Liu, J.; Dresselhaus, M. S.; Chen, G.; Ren, Z. High-Thermoelectric Performance of Nanostructured Bismuth Antimony Telluride Bulk Alloys. *Science* **2008**, *320*, 634-638.

[39] Shen, J.-J.; Zhu, T.-J.; Zhao, X.-B.; Zhang, S.-N.; Yang, S.-H.; Yin, Z.-Z. Recrystallization Induced in situ Nanostructures in Bulk Bismuth Antimony Tellurides: A Simple Top Down Route and Improved Thermoelectric Properties. *Energy Environ. Sci.* **2010**, *3*, 1519-1523.

[40] Deng, R.; Su, X.; Zheng, Z.; Liu, W.; Yan, Y.; Zhang, Q.; Dravid, V. P.; Uher, C.; Kanatzidis, M. G.; Tang, X. Thermal Conductivity in $\text{Bi}_{0.5}\text{Sb}_{1.5}\text{Te}_{3+x}$ and The Role of Dense Dislocation Arrays at Grain Boundaries. *Sci. Adv.* **2018**, *4*, eaar5606.

[41] Liu, W.-S.; Zhang, Q.; Lan, Y.; Chen, S.; Yan, X.; Zhang, Q.; Wang, H.; Wang, D.; Chen, G.; Ren, Z. Thermoelectric Property Studies on Cu-

Doped n-Type $\text{Cu}_x\text{Bi}_2\text{Te}_{2.7}\text{Se}_{0.3}$ Nanocomposites. *Adv. Energy Mater.* **2011**, *1*, 577-587.

[42] Yan, X.; Poudel, B.; Ma, Y.; Liu, W. S.; Joshi, G.; Wang, H.; Lan, Y.; Wang, D.; Chen, G.; Ren, Z. F. Experimental Studies on Anisotropic Thermoelectric Properties and Structures of n-Type $\text{Bi}_2\text{Te}_{2.7}\text{Se}_{0.3}$. *Nano Letters* **2010**, *10*, 3373-3378.

[43] Zheng, G.; Su, X.; Liang, T.; Lu, Q.; Yan, Y.; Uher, C.; Tang, X. High Thermoelectric Performance of Mechanically Robust n-Type $\text{Bi}_2\text{Te}_{3-x}\text{Se}_x$ Prepared by Combustion Synthesis. *J. Mater. Chem. A* **2015**, *3*, 6603-6613.

[44] Cui, J. L.; Mao, L. D.; Yang, W.; Xu, X. B.; Chen, D. Y.; Xiu, W. J. Thermoelectric Properties of Cu-Doped n-Type $(\text{Bi}_2\text{Te}_3)_{0.9}-(\text{Bi}_{2-x}\text{Cu}_x\text{Se}_3)_{0.1}$ ($x = 0 - 0.2$) Alloys. *J. Solid State Chem.* **2007**, *180*, 3583-3587.

[45] Zhang, Y.; Jia, X.; Sun, H.; Sun, B.; Liu, B.; Liu, H.; Kong, L.; Ma, H. Suppressing Adverse Intrinsic Conduction of Bi_2Te_3 Thermoelectric Bulks by Sb and Cu Co-Substitutions via HPHT Synthesis. *RSC Advances* **2016**, *6*, 7378-7383.

[46] Hao F.; Qiu P.; Tang Y.; Bai S.; Xing T.; Chu H.; Zhang Q.; Lu P.; Zhang T.; Ren D.; Chen J.; Shi X.; Chen L. High efficiency Bi_2Te_3 -based materials and devices for thermoelectric power generation between 100 and 300 °C. *Energy Environ. Sci.*, **2016**, *9*, 3120-3127.

[47] Han, M.-K.; Ahn, K.; Kim, H.; Rhyee, J.-S.; Kim, S.-J. Formation of

Cu Nanoparticles in Layered Bi₂Te₃ and Their Effect on *ZT* Enhancement. *J. Mater. Chem.* **2011**, *21*, 11365-11370.

[48] Park, K.; Ahn, K.; Cha, J.; Lee, S.; Chae, S. I.; Cho, S.-P.; Ryee, S.; Im, J.; Lee, J.; Park, S.-D.; Han, M. J.; Chung, I.; Hyeon, T. Extraordinary Off-Stoichiometric Bismuth Telluride for Enhanced n-Type Thermoelectric Power Factor. *J. Am. Chem. Soc.* **2016**, *138*, 14458-14468.

[49] Wu H.; Yen W. High Thermoelectric Performance in Cu-doped Bi₂Te₃ with Carrier-type Transition. *Acta Mater.* **2018**, *157*, 33-41

[50] Shannon, R. D. Revised Effective Ionic-Radii and Systematic Studies of Interatomic Distances in Halides and Chalcogenides. *Acta Crystallogr. Sect. A* **1976**, *32* (Sep1), 751-767.

[51] Seong S.; Albright T. A.; Zhang X.; Kanatzidis. M. G. Te-Te Bonding in Copper Tellurides. *J. Am. Chem. Soc.* **1994**, *16*, 7287-7293.

[52] Fleurial, J. P.; Gailliard, L.; Triboulet, R.; Scherrer, H.; Scherrer, S. Thermal Properties of High Quality Single Crystals of Bismuth Telluride—Part I: Experimental Characterization. *J. Phys. Chem. Solids* **1988**, *49*, 1237-1247.

[53] Lee Y.; Lo S.; Chen C.; Sun H.; Chung D.; Chasapis T.; Uher C.; Dravid V.; Kanatzidis. M. G. Contrasting Role of Antimony and Bismuth Dopants on the Thermoelectric Performance of Lead Selenide. *Nat. Commun.*

2014, 5, 3640.

[54] Batista, J.; Mandelis, A.; Shaughnessy, D. Temperature Dependence of Carrier Mobility in Si Wafers Measured by Infrared Photocarrier Radiometry. *Appl. Phys. Lett.* **2003**, 82, 4077-4079.

[55] Ravich, Y. I.; Efimova, B. A.; Tamarchenko, V. I. Scattering of Current Carriers and Transport Phenomena in Lead Chalcogenides ii. Experiment. *Physica. Status Solidi. B* **1971**, 43, 453.

[56] Qiu P.; Zhang T.; Qiu Y.; Shi X.; Chen L. Sulfide Bornite Thermoelectric Material: A Natural Mineral with Ultralow Thermal Conductivity. *Energy Environ. Sci.* **2014**, 7, 4000-4006.

[57] Peranio N.; Eibl O. Gliding Dislocations in Bi₂Te₃ Materials. *Phys. Status Solidi A* **2009**, 206, 42–49

[58] Walukiewicz W. Dislocation Density Reduction by Isoelectronic Impurities in Semiconductors. *Appl. Phys. Lett.* **1989**, 54, 2009.

[59] Zhou C.; Lee, Y. K.; Cha J.; Yoo B.; Cho, S.-P.; Hyeon, T.; Chung, I. Defect Engineering for High-Performance n-Type PbSe Thermoelectrics. *J. Am. Chem. Soc.* **2018**, 140, 9282-9290.

[60] Matthiessen, A.; Vogt, C. On The Influence of Temperature on the Electric Conducting-Power of Alloys. *Philos. Trans. R. Soc. Lond.* **1864**, 154,

167-200.

[61] Zhang L.; Xiao P.; Shi L.; Henkelman G.; Goodenough J. B.; Zhou J. Suppressing the Bipolar Contribution to the Thermoelectric Properties of $\text{Mg}_2\text{Si}_{0.4}\text{Sn}_{0.6}$ by Ge Substitution. *J. Appl. Phys.* **2015**, *117*, 155103.

[62] Chen, Z.; Ge, B.; Li, W.; Lin, S.; Shen, J.; Chang, Y.; Hanus, R.; Snyder, G. J.; Pei, Y. Vacancy-Induced Dislocations within Grains for High-Performance PbSe Thermoelectrics. *Nat. Commun.* **2017**, *8*, 13828.

Chapter 4. High Power Density Skutterudite-based Thermoelectric Modules with Ultralow Contact Resistivity Using Fe-Ni Metallization Layers

4.1 Introduction

The substantial amount of energy, for example, between 20% to 50% of industrial energy input, is lost as a waste heat every year.¹⁻² Developing economically feasible means of harnessing such a ubiquitous and huge energy source is a primary subject of renewable energy technologies and can significantly contribute to reducing evolution of green-house gases. Thermoelectric (TE) technology can directly generate electrical power from heat energy employing couples of n- and p-type semiconductors. Accordingly, it can provide highly mechanically and environmentally reliable solid-state electronic devices for waste heat recovery. The TE conversion efficiency of materials is defined by the dimensionless figure of merit $ZT = S^2\sigma T/\kappa$, where S is the Seebeck coefficient, σ is the electrical conductivity, κ is the thermal conductivity, T is the absolute temperature, and $S^2\sigma$ is power factor (PF). The ZT has been too low for broad commercialization of this technology, remaining at as low as unity until early

2000. In 2004, a new strategy of markedly reducing lattice thermal conductivity and consequently enhancing ZT by nanostructuring resulted in a surged ZT of ~ 1.8 for bulk materials of $\text{AgPb}_m\text{SbTe}_{2+m}$.³ Since then, discovering new materials and developing new strategies to enhance their TE performance have been a main theme of relevant researches and have surprisingly improved ZT.⁴⁻³¹ For example, a record high ZT of ~ 2.6 at 923 K was reported for SnSe single crystals.^{11,24-25} A comparably high ZT of ~ 2.5 at 923 K was found in polycrystalline phases of Na-doped PbTe-SrTe alloys.²⁶ With rising ZT, TE technology become more economically viable and its consumer products in various forms are being introduced to markets. Accordingly, it is time to more focus on device fabrication technologies for practical applications of thermoelectrics, which have been largely ignored so far in comparison to materials discovery.

TE devices generally consist of numerous couples of n- and p-type TE materials in a rectangular leg shape that generate electrical power. To maximally transfer energy generated, the TE legs should be interconnected onto metallic electrodes pre-deposited on a device substrate with minimal interface contact resistances. However, distinct physical and chemical nature between metallic electrodes and typical TE materials such as metal chalcogenide, Zintl, and intermetallic compounds makes it highly challenging to form seamless heterojunctions between them. As a result,

unfavourable extrinsic factors such as contact resistances at the interface and energy loss by convection and radiation can severely affect their overall power generation performance besides the inevitable intrinsic factor of ZT of constituent TE materials. Very importantly, binding metallic parts and TE legs requires high temperature processes and the hot side of TE power generator must be exposed to high temperatures continuously to keep large temperature difference across TE legs. Accordingly, chemical reactions and inter-diffusion occurring at that interface must be avoided to minimize the unfavorable external factors to TE module performance. It should be noted that the problems of contact resistances and thermal and chemical stability discussed above have been relatively less studied so far.

Indeed, recent studies reported that the electrical and thermal interface contact resistance is the most critical source of discrepancy between the measured and calculated performance of the TE module.³² Thermal resistance extrinsically induces the significant decrease in the open circuit voltage (V_{OC}), thereby dramatically degrading the electrical power output according to the following eqn.

$$P_{out} = I^2 R_{load} = V_{OC}^2 \left[\frac{R_{load}}{(R_{load} + R_{intrinsic})^2} \right]$$

The eqn (1) clearly shows that the output power strongly depends on the V_{OC} and its decay due to thermal resistance rapidly deteriorates power generation

performance of TE modules. Thermal resistance also decreases the temperature difference (ΔT) across TE legs, hence directly reducing the efficiency and power output of TE modules. Electrical resistance generated at each TE leg accumulates over many couples of n- and p- type TE legs to give higher overall resistance. Although the problems of high contact resistances found in TE modules have been raised recently by several research groups³²⁻³³ and solutions to these must be requisite for manufacturing TE devices, studies on these issues have been scarce.

Here we report that the Fe-Ni metallization layers can bind skutterudite(SKD)-based TE legs and metallic electrodes with minimal loss of energy transfer across them to form high performance TE power generators. We applied it to fabricate an 8 couple TE module comprising commercially available n-type $(\text{Mm,Sm})_y\text{Co}_4\text{Sb}_{12}$ ($ZT_{\text{max}} = 0.9$) and p-type $\text{DD}_y\text{Fe}_3\text{CoSb}_{12}$ ($ZT_{\text{max}} = 0.7$) SKD materials. Its introduction is attributed to the lowest electrical contact resistivity of $\sim 2.3\text{--}2.5 \mu\Omega \text{ cm}^2$ at the interface to date and resultant ultralow internal resistance of 42 m Ω . In comparison, top SKD-based TE modules exhibit 2–20 times larger values at $5\text{--}50 \mu\Omega \text{ cm}^2$.³⁴⁻
³⁶ Large contact resistivity is a main source of the deviation between theoretical and experimental TE module efficiencies.³² Accordingly, minimizing it can be a key to achieving high power TE generators. Indeed,

our device exhibits the maximum output power of 8.1 W and power density of 2.1 W cm^{-2} , driven by a temperature difference (ΔT) of 570 K. The latter is a core feature for commercialization of this technology and the obtained value is one of the highest among reported TE modules, regardless of constituent TE materials. In comparison, the highest value for the SKD³⁷ and PbTe-based modules³³ reported to date are 1.33 W cm^{-2} for a $\Delta T = 550 \text{ K}$ and 1.6 W cm^{-2} for a $\Delta T = 570 \text{ K}$, respectively. This result highlights the importance of low contact resistivity to attain high power output and density.

We also performed structural and elemental analysis for the interfacial layer between the SKD TE legs and the Fe-Ni metallization layer at the nanoscale level employing scanning transmission electron microscope (STEM). The results demonstrate that the Fe-Ni metallization layer almost perfectly blocks the atomic diffusion across the interface upon brazing and sintering processes at $\sim 900 \text{ K}$ and elongated exposure to high temperature at 773 K , confirming its high chemical and thermal stability in SKD-based TE modules.

4.2 Experimental section.

4.2.1 Reagents

The following chemicals were used as received: commercial n-type and p-type filled skutterudite (SKD) compounds of $(\text{Mm,Sm})_y\text{Co}_4\text{Sb}_{12}$ and $\text{DD}_y\text{Fe}_3\text{CoSb}_{12}$ (Mm stands for Misch metal that is an alloy of La, Ce, Pr, and Nd; and DD for didymium that is a mixture of Pr (4.76 mass%) and Nd (95.24 mass%)), respectively, reported in the literature³⁸ (Treibacher Industrie AG), and 325-mesh Fe-Ni powder ($\geq 99.9\%$, 35 wt% Ni-65 wt% Fe, Alfa Aesar).

4.2.2 Sample preparation and electrical and thermal transport measurements

We intentionally utilized commercially available, mass-produced SKD materials to save the total cost of module fabrication and to show general applicability of the Fe-Ni metallization layer to SKD-based TE modules although they show much lower ZT than the state-of-the-art SKD materials typically given by the lab-scale synthesis. The purchased SKD materials were powdered by a mechanical grinder, sieved to less than 45 μm , and loaded into a graphite-die in an argon-filled glove box. The powders were densified at 923 K for 10 min under an axial pressure of 50 MPa in a vacuum of $\sim 10^{-3}$ Torr by spark plasma sintering (SPS) (SPS-211LX, Fuji Electronic Industrial Co., Ltd.). The sintered compacts were cut and

polished into a disk with a radius of 13 mm and thickness of 2 mm under a N₂ atmosphere. The electrical conductivity and Seebeck coefficient were taken simultaneously under an He atmosphere from room temperature to 773 K using a ULVAC-RIKO ZEM-3 instrument system. A LFA 457 MicroFlash system (Netzsch) was employed to measure the thermal diffusivity of the samples coated with graphite. The thermal conductivity was obtained from $\kappa_{\text{tot}} = D \cdot C_p \cdot \rho$, where D is the thermal diffusivity, C_p is the heat capacity, and ρ is the mass density of the specimens. The temperature-dependent C_p values were indirectly derived using a standard sample (Pyroceram). The ρ values used were obtained from their geometrical dimensions and masses.

4.2.3 Module fabrication and characterization

We introduced the Fe-Ni metallization layer to reduce electrical and thermal contact resistivity and prevent inter-diffusion between TE legs and interconnecting electrodes simultaneously. The Fe-Ni pellet was prepared by cold-pressing 0.1 g of Fe-Ni powder using a stainless steel die ($\text{\O} = 12$ mm). 3 g of SKD powder was placed between two resulting Fe-Ni pellets and cold-pressed together using a graphite die ($\text{\O} = 12$ mm). The obtained Fe-Ni/SKD/Fe-Ni structure was subsequently sintered by SPS at 923 K for the n-type SKD and 893 K for the p-type SKD for 10 min under a uniaxial pressure of 50 MPa in a vacuum at $\sim 10^{-3}$ Torr. SPS processed joints were cut and polished with a 0.3 μm alumina suspension into rectangular-shaped legs

with a mirror-like finish. Afterwards, the Fe-Ni metallized SKD TE legs were diced into a cube with a dimension of 4 mm. They were subsequently joined onto to Cu electrodes pre-deposited on alumina substrates (20 mm × 20 mm) using Incusil-series brazing alloy for the hot side and using low temperature Sn-based solder alloy for the cold side. The latter was also used to connect wires to TE modules. To preliminarily investigate thermal stability, the Fe-Ni metallized SKD TE legs were loaded at elevated temperature of 773 K for 10 h in a vacuum of $\sim 10^{-3}$ Torr. The output voltage and power of fabricated TE modules were measured from 573 K to 873 K under a loading pressure of 2 MPa. The electrical contact resistivity between TE legs and metallization layers was measured using an in-house apparatus.³⁹

4.2.4 Scanning and Transmission Microscopy

The interfaces between metallization layer and TE legs were examined using a scanning electron microscope (SEM, JEOL JSM-7000F) equipped with an energy dispersive X-ray spectroscopy (EDS) detector. Structures at the nano-scale level and their chemical compositions on the interface were investigated employing high-angle annular dark-field scanning transmission electron microscopy (HAADF-STEM, JEOL J EM-2100F), STEM-EDS, and selected-area electron diffraction (SAED) studies.

The cross-sectional samples for those studies were prepared by focused ion beams (FIB, FEI Quanta 3D FEG). The SAED patterns were analysed using the CrysTBox software.⁴⁰

4.3. Results and discussion

4.3.1 Thermoelectric properties of skutterudite materials

Skutterudite (SKD) compounds MX_3 (M = transition metals of group 8 and X = pnictogens) adopt a distorted perovskite structure with an empty icosahedral site at the center of the cube formed by eight MX_3 octahedra. The central void can be filled by multiple guest atoms and their interplay with the MX_3 framework mainly contributes to thermoelectric (TE) properties of SKD materials, especially a reduction in lattice thermal conductivity.⁴¹ They are promising for TE power generators operating at the intermediate temperature range from 300–700 °C because of their considerably high power factors and ZTs both for n- and p-type materials as well as relatively high stability at operating temperatures.⁴²⁻⁴⁵

We conducted TE property characterization for the n- and p-type SKD materials of $(\text{Mm,Sm})_y\text{Co}_4\text{Sb}_{12}$ and $\text{DD}_y\text{Fe}_3\text{CoSb}_{12}$, respectively, utilized in our TE devices. Their temperature-dependent electrical conductivity (σ) and Seebeck coefficient (S) are shown in Figure 4. 1a and b, respectively, showing a typical conduction behavior of semiconductors. The former monotonously decreases with temperature. Their power factor (σS^2) gradually rises with temperature (Figure 4. 1c). The values of p- and n-type materials are ~ 47 and $\sim 25 \mu\text{W cm}^{-1} \text{K}^{-2}$ at 773K, respectively. In comparison, those of TE elements

in the best performing PbTe-based thermoelectric (TE) module reported exhibit much lower values.³³ The power factors of the p- and n-type nanostructured PbTe materials reach the peak value of ~ 25 and $\sim 22 \mu\text{W cm}^{-1} \text{K}^{-2}$ at ~ 600 K and decrease to ~ 22 and $15 \mu\text{W cm}^{-1} \text{K}^{-2}$ at 900 K, respectively. In fact, a high power factor is a signature feature of SKD materials. It can be a core of achieving high power output in TE modules because thermal conductivity does not affect the power density under steady-state heat conduction. Indeed, its effect, coupled with ultralow contact resistivity, is reflected on markedly high power density of our TE module, as discussed later in this work.

The temperature-dependent total thermal conductivity is shown in Figure 4. 1d. The values of the n-type material are much higher than those of the p-type counterpart over the entire temperature range, possibly due to the higher electronic contribution correlated with its larger electrical conductivity. It is important to note that both types of the SKD materials show a similar trend of respective TE properties over the entire range of temperature. Such a combination would be beneficial to overall module performance. The thermoelectric figure of merit values increase with temperature and reach the maximum of ~ 0.9 and ~ 0.7 at 773 K for n- and p-type materials, respectively (Figure 4. 2). The values are slightly lower than those reported in the

literature,⁴⁶ possibly due to the use of mass-produced samples and unoptimized densification process. In comparison, the n- and p-type nanostructured PbTe materials in the state-of-the-art PbTe-based TE module mentioned above display ZT_{\max} of ~ 1.4 at 750 K and ~ 1.8 at 810 K, respectively.³³

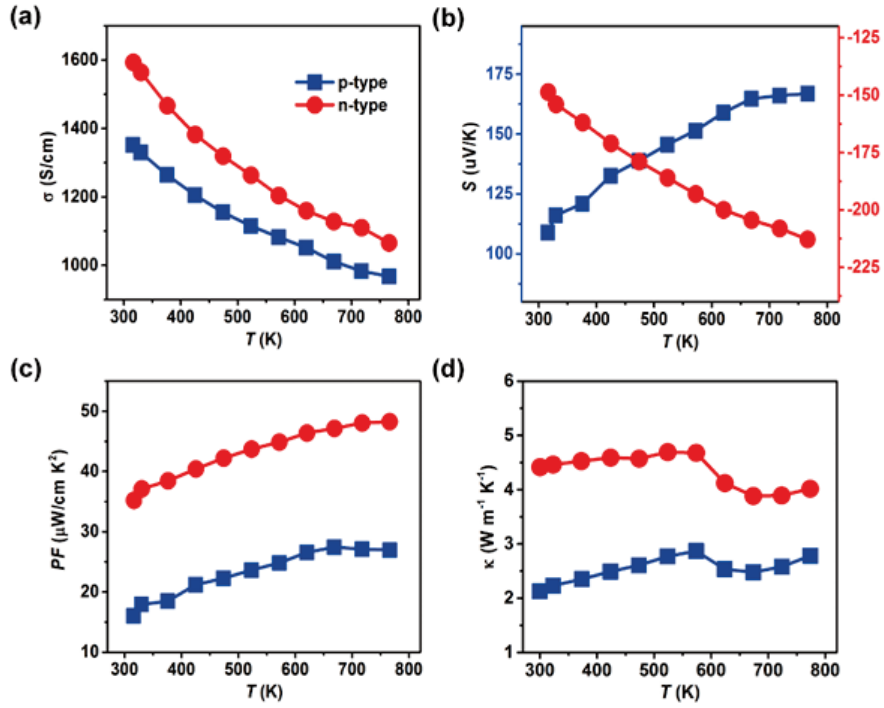


Figure 4. 1. (a) Electrical conductivity (σ), (b) Seebeck coefficient (S), (c) power factor (σS^2), and (d) total thermal conductivity (κ_{tot}) for the n-type $(\text{Mm,Sm})_y\text{Co}_4\text{Sb}_{12}$ and p-type $\text{DD}_y\text{Fe}_3\text{CoSb}_{12}$ as a function of temperature.

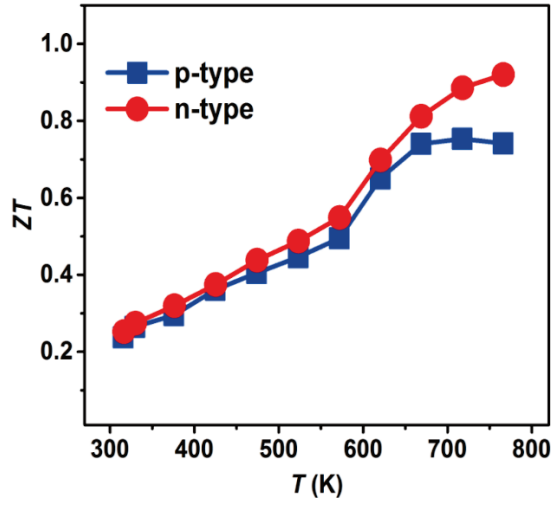


Figure 4.2. Thermoelectric figure of merit for n-type $(Mm,Sm)_yCo_4Sb_{12}$ and p-type $DD_yFe_3CoSb_{12}$ as a function of temperature.

4.3.2 Module fabrication and contact resistivity

Figure 4. 3a illustrates a schematic structure of our thermoelectric device operating at high temperatures. To minimize contact resistivity and interfacial diffusion, we selectively introduced the metallization layer of Fe-Ni alloy sandwiching TE materials. The metallization layer should be specialized for specific TE materials to avoid chemical reactions and mechanical failures at their interface because of high temperature operation of TE modules. We excluded expensive metals and alloys for price competitiveness with other renewable energy technology. Ni has been widely used for metallization barrier in Bi₂Te₃ and PbTe-based TE modules. However, it seriously reacts with SKD materials and does not form a robust interface with SKD materials because of chemical reactions between them. Ti also shows the similar problem as discussed later. Despite its relatively low reactivity with SKD materials, Mo gives rise to high contact resistivity because its constant of thermal expansion is significantly different from that of SKD materials. With all these considerations, we were able to develop the Fe-Ni metallization layer as an optimized diffusion barrier for SKD-based TE modules. Indeed, it readily secures the metallic electrodes by brazing because of their similar physical and thermal characteristic.

The Fe-Ni/SKD interfaces in this work exhibit ultralow electrical contact

resistivity of 2.52 and 2.32 $\mu\Omega \text{ cm}^2$ for n-type (Figure 4. 4a) and p-type (Figure 4. 4b) interfaces, respectively. The observed values are the lowest contact resistivity to date reported for TE modules of any classes of materials as shown in Table 4. 1.⁴⁷⁻⁵⁰ Especially, recently reported SKD-based modules show 2-20 times larger contact resistivities of 5–50 $\mu\Omega \text{ cm}^2$ at the metal/SKD interfaces.³⁴⁻³⁶

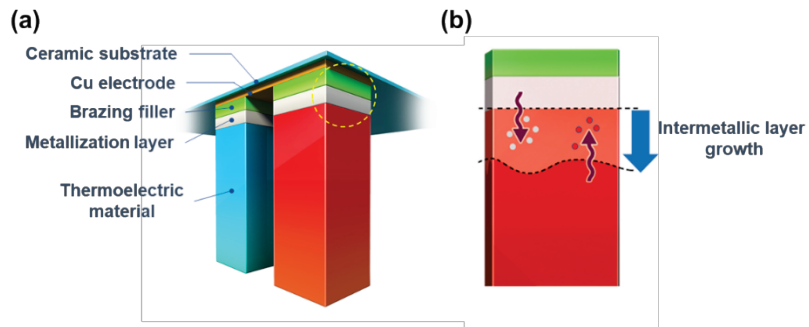


Figure 4. 3. (a) A schematic illustration of a TE module showing consecutive layers of a TE leg, metallization layer, brazing filler and metallic electrode on a ceramic substrate and (b) potential interfacial diffusion and intermetallic layer growth occurring at the metallization interface.

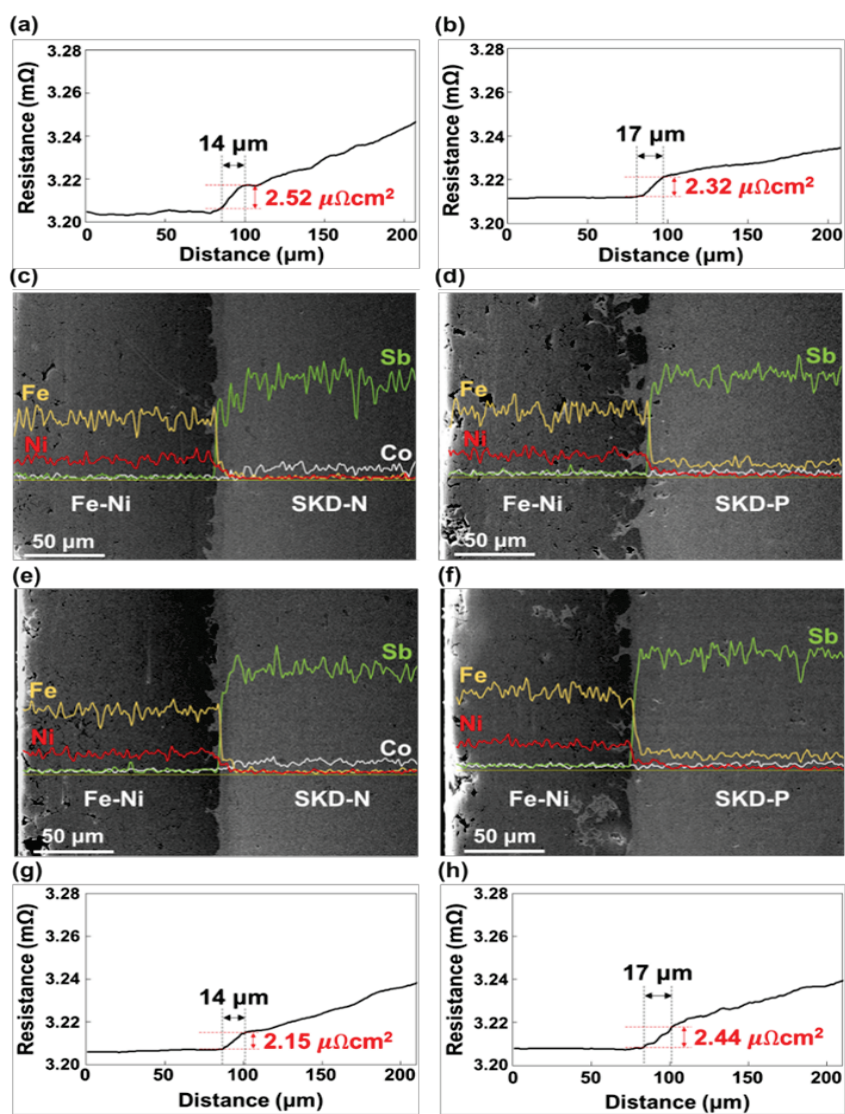


Figure 4.4. SEM images, SEM-EDS line scan profiles, and electrical resistivity profiles taken on the interface between the Fe-Ni metallization layer and n- (left) and p-type (right) SKD legs, respectively, before (a-d) and after (e-h) heat treatment at 773 K for 10 h in a vacuum.

Table 4. 1. Specific contact resistance for representative TE modules based on various classes of materials.

Thermoelectric materials	Metallization layer	Specific contact resistance ($\Omega \text{ cm}^2$)
$\text{Yb}_{0.3}\text{Co}_4\text{Sb}_{12}$ ⁴⁷	Mo-Ti	9×10^{-6}
Bi_2Te_3 ⁴⁸	Au	2.73×10^{-6}
Mg_2Si ⁴⁹	Ni	2.1×10^{-4}
$\text{Hf}_{0.5}\text{Zr}_{0.5}\text{CoSn}_{0.2}\text{Sb}_{0.8}$ ⁵⁰	Ag	3.8×10^{-5}
$(\text{Mm},\text{Sm})_y\text{Co}_4\text{Sb}_{12}$ – (This work)	Fe-Ni	2×10^{-6}

4.3.3 Metallization layer as a low contact resistivity diffusion barrier

Coupled with the ultralow electrical contact resistivity, another core role of the Fe-Ni metallization layer is effectively suppressing inter-diffusion between the constituent TE materials of SKD and the metallization layers and consequent undesirable growth of intermetallic layers at the interface. Indeed, maintaining their structure as well as electrical and thermal characteristics are prerequisite for low contact resistivity and long-term stability. However, it is highly challenging because TE power generation requires high operation temperatures, for example, ~ 773 K for SKD materials. As illustrated in Figure 4. 3b, atomic diffusion typically induces decomposition of TE materials and resultant formation of intermetallic layers at the interfaces, thereby ultimately degrading the long-term reliability of TE devices. Its growth can increase thermal and electrical contact resistances, decrease the V_{OC} , and cause mechanical cracks due to evolution of a deleterious secondary phase at the interfaces, eventually leading to failure of TE devices. In fact, the recent literatures reported that significant amounts of intermetallic layers grow between the Ti metallization layers and the SKD materials, damaging the module efficiency.⁵¹⁻⁵²

To verify capability of the Fe-Ni metallization layer as a diffusion

barrier, we analyzed the compositional variance across the Fe-Ni/SKD interface using a scanning electron microscope (SEM) equipped with an energy dispersive X-ray spectroscopy (EDS) detector. The cross-sectional SEM images and the corresponding SEM-EDS elemental line-scan profile taken on the n- and p-type junctions are shown in Figure 4. 4c and d, respectively. The data clearly demonstrate nearly negligible diffusion of constituent elements from both the n- and p-type SKD into the Fe-Ni layer. This observation confirms that our Fe-Ni metallization layer excellently prevents inter-diffusion between the SKD and the metallization layer during a module fabrication process under high-temperature and pressure conditions.

Observing an abrupt jump in the electrical resistivity profile across the interface indicates the formation of thin interfacial layer at the joint surface between the SKD and the metallization layer. Its width ranges from 14 to 17 μm for n- and p-type joints, respectively. It mainly composes of Fe, Ni and Sb for both the types. A slightly higher Fe concentration is observed for the p-type than the n-type according to the SEM-EDS elemental line-scan profile. This originates from the p-type SKD material of $\text{DD}_7\text{Fe}_3\text{CoSb}_{12}$ and not from the Fe-Ni layer. This interfacial layer shows the lowest electrical contact resistivity ever reported for TE modules as discussed above.

4.3.4 Thermal stability of metallization layer

To examine the preliminary thermal stability of the Fe-Ni metallization layer and the interface, the Fe-Ni metallized SKD TE legs were annealed at 773 K for 10 h in a vacuum at $\sim 10^{-3}$ Torr. The SEM images and the corresponding elemental line-scan profiles on the resulting n- and p-type legs show little atomic diffusion across the interface by heat treatment (Figure 4. 4e and f). More importantly, the electrical contact resistivity at the Fe-Ni/SKD interface negligibly changes (Figure 4. 4g and h). These results verify that the Fe-Ni metallization layer performs excellently as a diffusion barrier to keep the legs from chemical decomposition even operating at high temperatures up to 773 K. It should be noted that studies on thermal stability and its influence on contact resistivity of TE materials and adjoining metallic components implemented in TE modules are scarce. However, such researches are undoubtedly of paramount importance in achieving highly reliable TE power generators operating at high temperatures.

Afterwards, we performed structural analysis across the Fe-Ni/SKD interface by high-angle annular dark-field scanning transmission electron microscopy (HAADF-STEM) data and selected area electron diffraction (SAED) patterns because the compounds present at the interface are reported to play a crucial role in electrical contact resistivity of the TE modules.^{35, 51}

The HAADF-STEM images (Figure 4. 5a – b) show five and four discernible areas by contrast difference near the interface in the samples of metallized p- and n-type SKD, respectively. The STEM-EDS elemental line-scan profiles on the corresponding areas reduce them to three compositionally distinct regions both for the interfaces in the Fe-Ni/p-type SKD (A/B, C, and D/E) and the Fe-Ni/n-type SKD (F, G/H and I) joints (Figure 4. 5c and d). Interestingly, the Fe concentration is substantially high at the interface such as the regions of C, G, and H, consistent with the SEM-EDS results. Such areas correspond to those of the Sb concentration abruptly dropping. Accordingly, the Fe-rich regions appear to inhibit the diffusion of Sb atoms into the Fe-Ni metallization layer. In comparison, Sb atoms severely diffuse into the Ti diffusion barrier and react with SKD material, subsequently forming a brittle TiCoSb compound at the Ti/SKD interface upon thermal treatment. Resultantly, contact resistance was increased.⁵² The Mo diffusion barrier effectively prevents Sb atoms in the SKD from reacting with neighbouring metallic components. However, it develops large interface contact resistance³² possibly due to the substantially different constant of thermal expansion, thereby deteriorating the module efficiency.

The SAED patterns and the corresponding miller indices on the respective regions are shown in Figure 4. 5 e–j. Three independent types of

crystal structure are observed: cubic $\text{Fe}_{1-x}\text{Ni}_x$ structure (space group: $Im\bar{3}m$, lattice parameter: $a = 3.105(1) \text{ \AA}$ for Fe-Ni/p-type SKD and $Fm\bar{3}m$, $a = 3.603(1) \text{ \AA}$ for Fe-Ni/n-type SKD) near the Fe-Ni layer⁵³⁻⁵⁵, cubic Fe ($Im\bar{3}m$, $a = 2.846(1) \text{ \AA}$ for Fe-Ni/p-type SKD and $Im\bar{3}m$, $a = 2.762(1) \text{ \AA}$ for Fe-Ni/n-type SKD) structure near the interfacial surface, and hexagonal (Co, Ni, Fe)Sb (space group: $P6_3/mmc$) structure near the SKD region. For the last, the lattice parameters are calculated to be $a = 4.027(1) \text{ \AA}$ and $c = 5.171(1) \text{ \AA}$ for the p-type and $a = 3.978(1) \text{ \AA}$ and $c = 5.132(1) \text{ \AA}$ for the n-type specimens, respectively. These values match well with those of isostructural CoSb, FeSb and NiSb compounds.⁵⁶⁻⁵⁹ A detailed analysis of the SAED patterns are provided in the Supporting Information (Figure 4. 6). These results are consistent with those observed by the STEM-EDS line-scan profiles, verifying the rich concentration of Fe at the Fe-Ni/SKD interface and its role as a diffusion barrier. They also confirm that no detrimental phases to contact resistivity evolve at the interface.

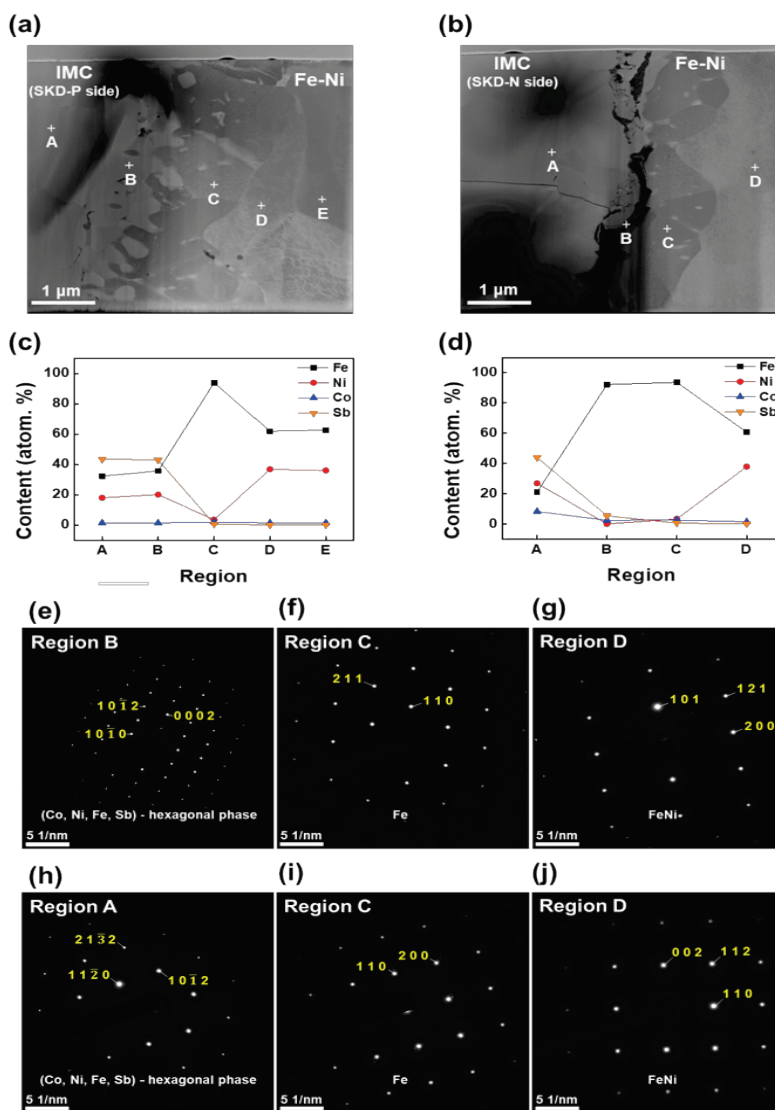


Figure 4. 5. HAADF-STEM images and STEM-EDS results at the interface of the p-type (a and c) and n-type (b and d) Fe-Ni/SKD interfaces and SAED patterns characterized by the $[uvw]$ indices on the corresponding regions (e-j) shown in the HAADF-STEM images.

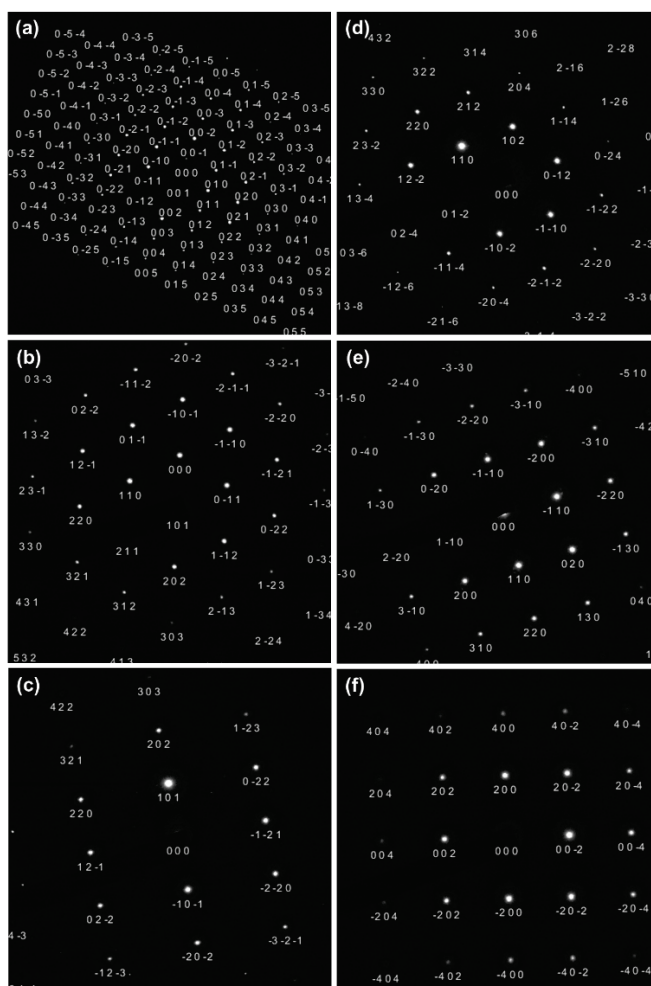


Figure 4. 6. Indexing of the selected area electron diffraction (SAED) patterns the interface of the Fe-Ni metallized p-type and n-type skutterudite/Fe-Ni: (a) indexing for zone axis $[\bar{1} 0 0]$ of the diffraction pattern of Region B in Figure 4. 5; (b) indexing for zone axis $[\bar{1} 1 1]$ of the diffraction pattern of Region C in Figure 4.5; (c) indexing for zone axis $[\bar{1} 1 1]$ of the diffraction pattern of Region D in Figure 4.5; (d) indexing for zone axis $[\bar{2} 2 0]$ of the diffraction pattern of Region F in Figure 4.5; (e) indexing for zone axis $[0 0 1]$ of the diffraction pattern of Region H in Figure 4.5; (f) indexing for zone axis $[0 1 0]$ of the diffraction pattern of Region I in Figure 4. 5.

4.3.5 High power density module

An 8 couple SKD TE device (Figure 4. 7a) applied with the Fe-Ni metallization layers shows extremely low internal resistance of 42 m Ω at room temperature, mainly due to the ultralow electrical contact resistivity characteristic (2.2–2.5 $\mu\Omega$ cm²) of the Fe-Ni metallization layer as shown in Figure 4. 4. However, such a device resistance can also be attributed from our fabrication engineering for the optimal thickness of electrodes, selecting connecting wires for power ports and soldering materials, and soldering processing conditions.

The power output of the module increases with higher hot side temperature (T_h) or temperature difference (ΔT) across the module (Figure 4. 7b). The maximum output power of 8.06 W is achieved at T_h of 873 K ($\Delta T = 570$ K). Considering the module dimension of $20 \times 20 \times 5$ mm³, the output power density reaches up to 2.1 W cm⁻². This value is the highest power density generated by a comparable ΔT among all TE power generators reported to date.^{33, 60-62} In contrast, the highest power density value for the SKD module reported previously is 1.3 W cm⁻² with $\Delta T = 460$ K.³⁷ Although the ZrNiSn/ZrCoSb-based half-Heusler module consists of TE materials with the comparable power factor to that of our SKD module, for example, ~ 43 and ~ 21 $\mu\text{W cm}^{-1} \text{K}^{-2}$ for the n-type and p-type, respectively, its power

density is nearly a half at 1.1 W cm^{-2} for a $\Delta T = 527 \text{ K}$.⁶² Note that, rather than a ZT, power factor directly affects power density under steady-state temperature gradients applied in TE modules because thermal conductivity has no influence on it. This observation clearly confirms that the significant power is lost by contact resistivity and highlights the importance of the metallization layer optimized for TE materials. The best-performing PbTe-based module comprising TE materials with the poorer power factors of $\sim 22\text{--}25 \mu\text{W cm}^{-1} \text{ K}^{-2}$ and higher contact resistivity shows the power density of 1.6 W cm^{-2} for a $\Delta T = 570 \text{ K}$.³³

Figure 4. 8 compares the output power density of the TE modules based on various materials reported.^{33,37,61-62} The normalized device internal resistance to one couple resistance also represents the lowest resistance characteristics of the Fe-Ni metallized SKD TE devices. Figure 4. 8 clearly reveals that the Fe-Ni metallization layer in this work enables the lowest contact resistivity with SKD materials as well as nearly inhibits atomic diffusion, consequently giving the high thermal stability and one of the highest power density under a comparable ΔT .

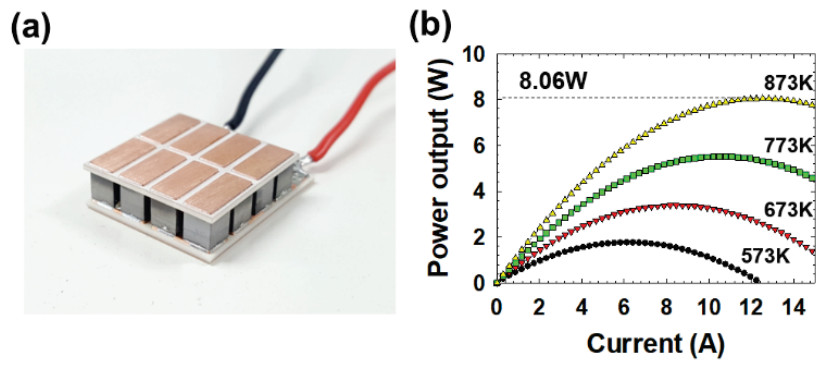


Figure 4. 7. (a) A photograph of the Fe-Ni metallized-SKD TE module and (b) its output power characteristics at various hot side temperature (T_h).

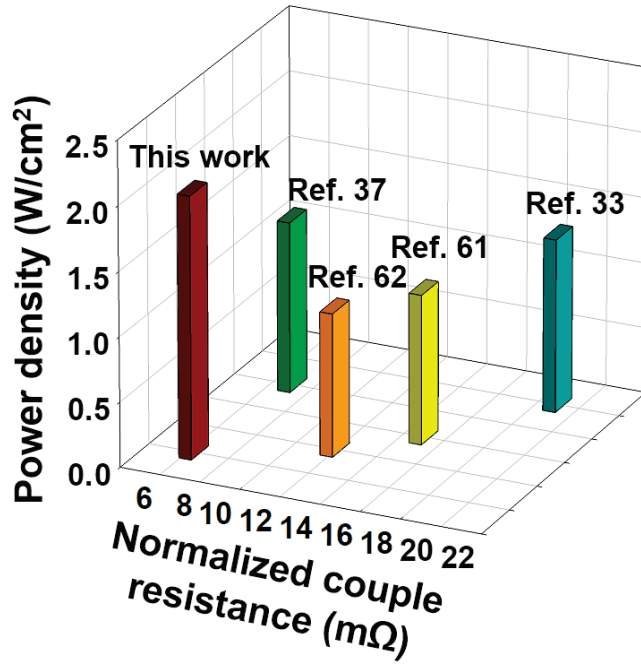


Figure 4. 8. Comparison of output power density for representative TE modules with their device internal resistance. The internal resistance is normalized to one thermocouple resistance.

4. 4 Conclusion

We introduced the Fe-Ni metallization layer to an 8 couple skutterudite thermoelectric module. This technology successfully binds naturally different skutterudite materials and a metallic electrode with minimally affecting electrical resistivity and chemical inertness between them. As a result, our thermoelectric device exhibits ultralow internal resistance of 42 m Ω and electrical contact resistivity of 2.2–2.5 $\mu\Omega$ cm² at room temperature. Importantly, such the lowest electrical contact resistivity to date does not deteriorate by brazing and sintering at 900 K and prolonged annealing at 773 K. Furthermore, this metallization layer does not permit atomic inter-diffusion between the interface, thereby keeping thermoelectric materials and metallic components from chemical degradation. It contributes to the highest reported power density of ~ 2.1 W cm⁻² of the module for a temperature difference of 570 K to date. This result confirms the paramount importance of ultralow contact resistivity given by the proposed metallization layer for high performance thermoelectric modules because our device is made of much lower ZT thermoelectric materials than other systems such as nanostructured PbTe and half-Heusler-based modules. The latter devices, in fact, suffer from lower power conversion efficiency than theoretical expectations. We will further reduce the electrical contact resistivity one order of magnitude to 10^{-7} Ω cm² for achieving higher power density. This work

strongly suggests that the metallization layers should be tailored to each class of thermoelectric materials for thermal and chemical stability and resulting low contact resistivity and high power density.

4. 5 References

[1] Johnson, I.; Choate, W. T.; Davidson, A. Waste Heat Recovery: Technology and Opportunities in US Industry. *US Department of Energy Industrial Technologies Program* **2008**.

[2] Gingerich, D. B.; Mauter, M. S. Quantity, Quality, and Availability of Waste Heat from United States Thermal Power Generation. *Environ. Sci. Technol.* **2015**, *49*, 8297-8306.

[3] Hsu, K. F.; Loo, S.; Guo, F.; Chen, W.; Dyck, J. S.; Uher, C.; Hogan, T.; Polychroniadis, E. K.; Kanatzidis, M.G. Cubic $\text{AgPb}_m\text{SbTe}_{2+m}$: Bulk Thermoelectric Materials with High Figure of Merit. *Science* **2004**, *303*, 818-821.

[4] Park, K. S.; Ahn, K. H.; Cha, J. I.; Lee, S. h.; Chae, S. I.; Cho, S. P.; Ryee, S. H.; Im, J.; Lee, J. K.; Park, S. D.; Han, M. J.; Chung, I.; Hyeon, T. H. Extraordinary Off-stoichiometric Bismuth Telluride for Enhanced N-type Thermoelectric Power Factor. *J. Am. Chem. Soc.* **2016**, *138*, 14458-14468.

[5] Son, J. S.; Park, K. S.; Han, M. K.; Kang, C. Y.; Park, S. G.; Kim, J. H.; Kim, W. C.; Kim, S. J.; Hyeon, T. H. Large-scale Synthesis and Characterization of the Size-dependent Thermoelectric Properties of Uniformly Sized Bismuth Nanocrystals. *Angew. Chem. Int. Ed.* **2011**, *50*, 1363-1366.

[6] Son, J. S.; Choi, M. K.; Han, M. K.; Park, K. S.; Kim, J. Y.; Lim, S. J.;

Oh, M. H.; Kuk, Y.; Park, C.; Kim, S. J.; Hyeon, T. H. n-Type Nanostructured Thermoelectric Materials Prepared from Chemically Synthesized Ultrathin Bi₂Te₃ Nanoplates. *Nano Lett.* **2012**, *12*, 640-647.

[7] Lee, Y. K.; Ahn, K. H.; Cha, J. I.; Zhou, C.; Kim, H. S.; Choi, G. R.; Chae, S. I.; Park, J. H.; Cho, S. P.; Park, S. H.; Sung, Y. E.; Lee, W. B.; Hyeon, T.; Chung, I. Enhancing P-type Thermoelectric Performances of Polycrystalline SnSe via Tuning Phase Transition Temperature. *J. Am. Chem. Soc.* **2017**, *139*, 10887-10896.

[8] Biswas, K.; He, J.; Blum, I. D.; Wu, C. I.; Hogan, T. P.; Seidman, D. N.; Dravid, V. P.; Kanatzidis, M. G. High-performance Bulk Thermoelectrics with All-scale Hierarchical Architectures. *Nature* **2012**, *489*, 414-418.

[9] Lee, Y. S.; Lo, S. H.; Androulakis, J.; Wu, C. I.; Zhao, L. D.; Chung, D.-Y.; Hogan, T. P.; Dravid, V. P.; Kanatzidis, M. G. High-Performance Tellurium-Free Thermoelectrics: All-Scale Hierarchical Structuring of P-type PbSe–MSe Systems (M = Ca, Sr, Ba). *J. Am. Chem. Soc.* **2013**, *135*, 5152-5160.

[10] Liu, H.; Shi, X.; Xu, F.; Zhang, L.; Zhang, W.; Chen, L.; Li, Q.; Uher, C.; Day, T.; Snyder, G. J. Copper Ion Liquid-like Thermoelectrics. *Nat. Mater.* **2012**, *11*, 422-425.

[11] Zhao, L. D.; Lo, S. H.; Zhang, Y.; Sun, H.; Tan, G.; Uher, C.; Wolverton, C.; Dravid, V. P.; Kanatzidis, M. G. Ultralow Thermal

Conductivity and High Thermoelectric Figure of Merit in SnSe Crystals.

Nature **2014**, *508*, 373-377.

[12] Zhao, L. D.; Tan, G.; Hao, S.; He, J.; Pei, Y.; Chi, H.; Wang, H.; Gong, S.; Xu, H.; Dravid, V. P.; Uher, C.; Snyder, G. J.; Wolverton, C.; Kanatzidis, M. G. Ultrahigh Power Factor and Thermoelectric Performance in Hole-doped Single-crystal SnSe. *Science* **2016**, *351*, 141-144.

[13] Banik, A.; Vishal, B.; Perumal, S.; Datta, R.; Biswas, K. The Origin of Low Thermal Conductivity in $\text{Sn}_{1-x}\text{Sb}_x\text{Te}$: Phonon Scattering via Layered Intergrowth Nanostructures. *Energy Environ. Sci.* **2016**, *9*, 2011-2019.

[14] Jana, M. K.; Pal, K.; Waghmare, U. V.; Biswas, K. The Origin of Ultralow Thermal Conductivity in InTe: Lone-Pair-Induced Anharmonic Rattling. *Angew. Chem. Int. Ed.* **2016**, *128*, 7923-7927.

[15] Shi, X.; Yang, J.; Salvador, J. R.; Chi, M.; Cho, J. Y.; Wang, H.; Bai, S.; Yang, J.; Zhang, W.; Chen, L. Multiple-Filled Skutterudites: High Thermoelectric Figure of Merit through Separately Optimizing Electrical and Thermal Transports. *J. Am. Chem. Soc.* **2011**, *133*, 7837-7846.

[16] Heremans, J. P.; Jovovic, V.; Toberer, E. S.; Saramat, A.; Kurosaki, K.; Charoenphakdee, A.; Yamanaka, S.; Snyder, G. J. Enhancement of Thermoelectric Efficiency in PbTe by Distortion of the Electronic Density of States. *Science* **2008**, *321*, 554-557

[17] Pei, Y.; Shi, X.; LaLonde, A.; Wang, H.; Chen, L.; Snyder, G. J.

Convergence of Electronic Bands for High Performance Bulk Thermoelectrics. *Nature* **2011**, *473*, 66-69.

[18] Tang, Y.; Gibbs, Z. M.; Agapito, L. A.; Li, G.; Kim, H. S.; Nardelli, M. B.; Curtarolo, S.; Snyder, G. J. Convergence of Multi-Valley Bands as the Electronic Origin of High Thermoelectric Performance in CoSb₃ Skutterudites. *Nat. Mater.* **2015**, *14*, 1223-1228.

[19] Zhang, Q.; Cao, F.; Liu, W.; Lukas, K.; Yu, B.; Chen, S.; Opeil, C.; Broido, D.; Chen, G.; Ren, Z. Heavy Doping and Band Engineering by Potassium to Improve the Thermoelectric Figure of Merit in P-type PbTe, PbSe, and PbTe_{1-y}Se_y. *J. Am. Chem. Soc.* **2012**, *134*, 10031-10038.

[20] Tan, G.; Shi, F.; Hao, S.; Chi, H.; Bailey, T. P.; Zhao, L.-D.; Uher, C.; Wolverton, C.; Dravid, V. P.; Kanatzidis, M. G. Valence Band Modification and High Thermoelectric Performance in SnTe Heavily Alloyed with MnTe. *J. Am. Chem. Soc.* **2015**, *137*, 11507-11516.

[21] Banik, A.; Shenoy, U. S.; Saha, S.; Waghmare, U. V.; Biswas, K. High Power Factor and Enhanced Thermoelectric Performance of SnTe-AgInTe₂: Synergistic Effect of Resonance Level and Valence Band Convergence. *J. Am. Chem. Soc.* **2016**, *138*, 13068-13075.

[22] Liu, W. S.; Zhang, Q.; Lan, Y.; Chen, S.; Yan, X.; Zhang, Q.; Wang, H.; Wang, D.; Chen, G.; Ren, Z. Thermoelectric Property Studies on Cu-doped N-type Cu_xBi₂Te_{2.7}Se_{0.3} Nanocomposites. *Adv. Energy Mater.* **2011**, *1*,

577-587.

[23] Biswas, K.; He, J.; Zhang, Q.; Wang, G.; Uher, C.; Dravid, V. P.; Kanatzidis, M. G. Strained Endotaxial Nanostructures with High Thermoelectric Figure of Merit. *Nat. Chem.* **2011**, *3*, 160-166.

[24] Zhao, L. D.; Chang, C.; Tan, G.; Kanatzidis, M. G. SnSe: A Remarkable New Thermoelectric Material. *Energy Environ. Sci.* **2016**, *9*, 3044-3060.

[25] Peng, K.; Lu, X.; Zhan, H.; Hui, S.; Tang, X.; Wang, G.; Dai, J.; Uher, C.; Wang, G.; Zhou, X. Broad Temperature Plateau for High ZTs in Heavily Doped P-type SnSe Single Crystals. *Energy Environ. Science* **2016**, *9*, 454-460.

[26] Tan, G.; Shi, F.; Hao, S.; Zhao, L. D.; Chi, H.; Zhang, X.; Uher, C.; Wolverton, C.; Dravid, V. P.; Kanatzidis, M. G. Non-equilibrium Processing Leads to Record High Thermoelectric Figure of Merit in PbTe-SrTe. *Nat. Commun.* **2016**, *7*, 12167-12175.

[27] Park, S. H.; Jin, Y. H.; Ahn, K. H.; Chung, I.; Yoo, C. Y. Ag/Ni Metallization Bilayer: A Functional Layer for Highly Efficient Polycrystalline SnSe Thermoelectric Modules. *J. Electron. Mater.* **2017**, *46*, 848-855.

[28] Zhang, X.; Wang, D.; Wu, H.; Yin, M.; Pei, Y.; Gong, S.; Huang, L.;

Pennycook, S. J.; He, J.; Zhao, L.-D. Simultaneously Enhancing the Power Factor and Reducing the Thermal Conductivity of SnTe via Introducing Its Analogues. *Energy Environ. Sci.* **2017**, *10*, 2420-2431.

[29] Ahn, K. H.; Shin, H. C.; Im, J.; Park, S. H.; Chung, I. ZnTe Alloying Effect on Enhanced Thermoelectric Properties of P-type PbTe. *ACS Appl. Mater. Interfaces* **2017**, *9*, 3766-3773.

[30] Fu, C.; Bai, S.; Liu, Y.; Tang, Y.; Chen, L.; Zhao, X.; Zhu, T. Realizing High Figure of Merit in Heavy-band P-type Half-Heusler Thermoelectric Materials. *Nat. Commun.* **2015**, *6*, 8144-8150.

[31] Girard, S. N.; He, J.; Zhou, X.; Shoemaker, D.; Jaworski, C. M.; Uher, C.; Dravid, V. P.; Heremans, J. P.; Kanatzidis, M. G. High Performance Na-Doped PbTe-PbS Thermoelectric Materials: Electronic Density of States Modification and Shape-controlled Nanostructures. *J. Am. Chem. Soc.* **2011**, *133*, 16588-16597.

[32] Salvador, J. R.; Cho, J. Y.; Ye, Z.; Moczygemba, J. E.; Thompson, A. J.; Sharp, J. W.; Koenig, J. D.; Maloney, R.; Thompson, T.; Sakamoto, J.; Wang, H.; Wereszczak, A. A. Conversion Efficiency of Skutterudite-Based Thermoelectric Modules. *Phys. Chem. Chem. Phys.* **2014**, *16*, 12510-12520.

[33] Hu, X.; Jood, P.; Ohta, M.; Kunii, M.; Nagase, K.; Nishiate, H.; Kanatzidis, M. G.; Yamamoto, A. Power Generation from Nanostructured PbTe-Based Thermoelectrics: Comprehensive Development from Materials

to Modules. *Energy & Environmental Science* **2016**, *9*, 517-529.

[34] Wojciechowski, K. T.; Zybala, R.; Mania, R. High Temperature CoSb₃-Cu Junctions. *Microelectron. Reliab.* **2011**, *51*, 1198-1202.

[35] Zhao, D.; Geng, H.; Chen, L. Microstructure Contact Studies for Skutterudite Thermoelectric Devices. *Int. J. Appl. Ceram. Technol.* **2012**, *9*, 733-741.

[36] Zhao, D.; Geng, H.; Teng, X. Fabrication and Reliability Evaluation of CoSb₃/W-Cu Thermoelectric Element. *J. Alloys Compd.* **2012**, *517*, 198-203.

[37] Nie, G.; Suzuki, S.; Tomida, T.; Sumiyoshi, A.; Ochi, T.; Mukaiyama, K.; Kikuchi, M.; Guo, J. Q.; Yamamoto, A.; Obara, H. Performance of Skutterudite-Based Modules. *J. Electron. Mater.* **2017**, *46*, 2640-2644.

[38] Rogl, G.; Grytsiv, A.; Failamani, F.; Hochenhofer, M.; Bauer, E.; Rogl, P. Attempts to Further Enhance ZT in Skutterudites via Nano-Composites. *J. Alloys Compd.* **2017**, *695*, 682-696.

[39] Kim, Y.; Yoon, G.; Park, S. H. Direct Contact Resistance Evaluation of Thermoelectric Legs. *Exp. Mech.* **2016**, *56*, 861-869.

[40] Klinger, M.; Jäger, A. Crystallographic Tool Box (CrysTBox): Automated Tools for Transmission Electron Microscopists and Crystallographers. *J. Appl. Crystallogr.* **2015**, *48*, 2012-2018.

[41] Zhu, T.; Liu, Y.; Fu, C.; Heremans, J. P.; Snyder, J. G.; Zhao, X.

Compromise and Synergy in High-Efficiency Thermoelectric Materials. *Adv. Mater.* **2017**, *29*, 1605884-1605909

[42] Rogl, G.; Rogl, P. Skutterudites, A Most Promising Group of Thermoelectric Materials. *Curr. Opin. Green Sustainable Chem.* **2017**, *4*, 50-57.

[43] Dahal, T.; Gahlawat, S.; Jie, Q.; Dahal, K.; Lan, Y.; White, K.; Ren, Z. Thermoelectric and Mechanical Properties on Misch Metal Filled P-type Skutterudites $Mm_{0.9}Fe_{4-x}Co_xSb_{12}$. *J. Appl. Phys.* **2015**, *117*, 055101-055108.

[44] Gayner, C.; Kar, K. K. Recent Advances in Thermoelectric Materials. *Prog. Mater. Sci.* **2016**, *83*, 330-382.

[45] Tomida, T.; Sumiyoshi, A.; Nie, G.; Ochi, T.; Suzuki, S.; Kikuchi, M.; Mukaiyama, K.; Guo, J. Q. Fabrication of 200 mm Diameter Sintering Body of Skutterudite Thermoelectric Material by Spark Plasma Sintering. *J. Electron. Mater.* **2016**, *46*, 2944-2949.

[46] Rogl, G.; Grytsiv, A.; Rogl, P.; Bauer, E.; Hochenhofer, M.; Anbalagan, R.; Mallik, R. C.; Schafner, E. Nanostructuring of P- and N-type Skutterudites Reaching Figures of Merit of Approximately 1.3 and 1.6, Respectively. *Acta Mater.* **2014**, *76*, 434-448

[47] Fan, X. C.; Gu, M.; Shi, X.; Chen, L. D.; Bai, S. Q.; Nunna, R. Fabrication and Reliability Evaluation of $Yb_{0.3}Co_4Sb_{12}/Mo-Ti/Mo-Cu/Ni$ Thermoelectric Joints. *Ceram. Int.* **2015**, *41*, 7590-7595.

[48] Yong, H.; Na, S. K.; Gang, J. G.; Shin, H. S.; Jeon, S. J.; Hyun, S. M.; Lee, H. J. Study on the Contact Resistance of Various Metals (Au, Ti, and Sb) on Bi–Te and Sb–Te Thermoelectric Films. *Jpn. J. Appl. Phys* **2016**, *55*, 06JE03

[49] Zhang, B.; Zheng, T.; Wang, Q.; Zhu, Y.; Alshareef, H. N.; Kim, M. J.; Gnade, B. E. Contact Resistance and Stability Study for Au, Ti, Hf and Ni Contacts on Thin-film Mg₂Si. *J. Alloys Compd.* **2017**, *699*, 1134-1139.

[50] Ngan, P. H.; Van Nong, N.; Hung, L. T.; Balke, B.; Han, L.; Hedegaard, E. M. J.; Linderoth, S.; Pryds, N. On the Challenges of Reducing Contact Resistances in Thermoelectric Generators Based on Half-Heusler Alloys. *J. Electron. Mater.* **2015**, *45*, 594-601.

[51] Gu, M.; Xia, X.; Li, X.; Huang, X.; Chen, L. Microstructural Evolution of the Interfacial Layer in the Ti–Al/Yb_{0.6}Co₄Sb₁₂ Thermoelectric Joints at High Temperature. *J. Alloys Compd.* **2014**, *610*, 665-670.

[52] Gu, M.; Xia, X.; Huang, X.; Bai, S.; Li, X.; Chen, L. Study on the Interfacial Stability of P-type Ti/Ce_yFe_xCo_{4-x}Sb₁₂ Thermoelectric Joints at High Temperature. *J. Alloys Compd.* **2016**, *671*, 238-244.

[53] Sumiyama, K.; Kadono, M.; Nakamura, Y. Metastable *bcc* Phase in Sputtered Fe-Ni Alloys. *Trans. Jpn. Inst. Metals* **1983**, *24*, 190-194.

[54] Chaudhuri, D. K.; Ravindran, P. A.; Wert, J. J. Comparative X-Ray Diffraction and Electron Microscopic Study of the Transformation-Induced

Substructures in the Iron-nickel Martensites and Their Influence on the Martensite Properties. *J. Appl. Phys.* **1972**, *43*, 778-788.

[55] Dumpich, G.; Wassermann, E. F.; Manns, V.; Keune, W.; Murayama, S.; Miyako, Y. Structural and Magnetic Properties of $\text{Ni}_x\text{Fe}_{1-x}$ Evaporated Thin Films. *J. Magn. Magn. Mater.* **1987**, *67*, 55-64.

[56] Chen, T.; Mikkelsen, J. C.; Charlan, G. B. Crystal Growth and Crystal Chemistry of NiAs-type Compounds: MnSb, CoSb, and NiSb. *J. Cryst. Growth* **1978**, *43*, 5-12.

[57] Castelliz, L. Kristallstruktur Von Mn_5Ge_3 und Einiger Ternärer Phasen Mit zwei Übergangselementen. *Monatsh. Chem.* **1953**, *84*, 765-776

[58] Rosenqvist, T. Magnetic and Crystallographic Studies on the Higher Antimonies of Iron, Cobalt and Nickel. *Acta Metall.* **1953**, *1*, 761-763.

[59] Kjekshus, A.; Walseth, K. P. On the Properties of the Cr_{1+x}Sb , Fe_{1+x}Sb , Co_{1+x}Sb , Ni_{1+x}Sb , Pd_{1+x}Sb and Pt_{1+x}Sb Phases. *Acta Chem. Scand.* **1969**, *23*, 2621-2630

[60] Zong, P.; Hanus, R.; Dylla, M.; Tang, Y.; Liao, J.; Zhang, Q.; Snyder, G. J.; Chen, L. Skutterudite with Graphene-Modified Grain-Boundary Complexion Enhances ZT Enabling High-efficiency Thermoelectric Device. *Energy Environ. Sci.* **2017**, *10*, 183-191

[61] Zhang, Q.; Zhou, Z.; Dylla, M.; Agne, M. T.; Pei, Y.; Wang, L.; Tang, Y.; Liao, J.; Li, J.; Bai, S.; Jiang, W.; Chen, L.; Jeffrey Snyder, G. Realizing

High-performance Thermoelectric Power Generation through Grain Boundary Engineering of Skutterudite-based Nanocomposites. *Nano Energy* **2017**, *41*, 501-510

[62] Bartholomé, K.; Balke, B.; Zuckermann, D.; Köhne, M.; Müller, M.; Tarantik, K.; König, J. Thermoelectric Modules Based on Half-Heusler Materials Produced in Large Quantities. *J. Electron. Mater.* **2014**, *43*, 1775-1781.

Bibliography

International Publications

1) **Joonil Cha**, Chongjian Zhou, Yong Kyu Lee, Sung-Pyo Cho, and In Chung,

“High Thermoelectric Performance in n-Type Polycrystalline SnSe via

Dual Incorporation of Cl and PbSe and Dense Nanostructures”

ACS Applied Materials & Interfaces, **2019**, 11, 21645–21654.

2) **Joonil Cha**, Chongjian Zhou, Sung-Pyo Cho, Sang Hyun Park, and In Chung,

“Ultrahigh Power Factor and Electron Mobility in n-Type $\text{Bi}_2\text{Te}_3-x\%$ Cu Stabilized

under Excess Te Condition”

ACS Applied Materials & Interfaces, **2019**, 11, 30999-31008.

3) Sang Hyun Park, Younghwan Jin, **Joonil Cha**, Kimin Hong, Yeongseon Kim,

Hana Yoon, Chung-Yul Yoo, and In Chung,

“High Power Density Skutterudite-based Thermoelectric Modules

with Ultralow Contact Resistivity Using Fe-Ni Metallization Layers”

ACS Applied Energy Materials, **2018**, 1, 1603–1611.

4) Chongjian Zhou, Yong Kyu Lee, **Joonil Cha**, Byeongjun Yoo, Sung-Pyo Cho,

Taeghwan Hyeon, and In Chung,

“Defect Engineering for High-Performance n-Type PbSe Thermoelectrics”

Journal of the American Chemical Society, **2018**, 140, 9282-9290.

5) Kunsu Park, Kyunghan Ahn, **Joonil Cha**, Sanghwa Lee, Sue In Chae, Sung-Pyo Cho, Siheon Ryee, Jino Im, Jaeki Lee, Su-Dong Park, Myung Joon Han, In Chung, and Taeghwan Hyeon,

“Extraordinary Off-Stoichiometric Bismuth Telluride for Enhanced n-Type Thermoelectric Power Factor”

Journal of the American Chemical Society, **2016**, 138, 14458-14468.

6) Yong Kyu Lee, Kyunghan Ahn, **Joonil Cha**, Chongjian Zhou, Hyo Seok Kim, Garam Choi, Sue In Chae, Jae-Hyuk Park, Sung-Pyo Cho, Sang Hyun Park, Yung-Eun Sung, Won Bo Lee, Taeghwan Hyeon, and In Chung,

“Enhancing p-Type Thermoelectric Performances of Polycrystalline SnSe via Tuning Phase Transition Temperature”

Journal of the American Chemical Society, **2017**, 139, 10887-10896.

7) Sejin Byun, **Joonil Cha**, Chongjian Zhou, Yong Kyu Lee, Hyungseok Lee, Sang Hyun, Park, Won Bo Lee, and In Chung,

“Unusual n-Type Thermoelectric Properties of Bi₂Te₃ Doped with Divalent Alkali Earth Metals”

Journal of Solid State Chemistry, **2019**, 269, 396-400.

국 문 초 록

최근 세계 인구의 빠른 성장과 심각한 환경 오염 문제로 인해 지속 가능하고 환경 친화적인 대체 에너지 기술 개발이 요구 되고 있다. 열전 기술은 원하지 않는 화학 잔류물을 방출하지 않고 열을 전기 에너지로 직접 변환할 수 있는 좋은 대체 에너지 기술 중 하나이다. 해당 기술이 보다 실용적이고 광범위하게 적용되기 위해서는 열전 소재의 성능 향상이 필수적이다. 본 학위 논문은 고효율 열전 소재 개발을 위한 새로운 합성법 개발 및 개발된 소재의 열전 특성에 대하여 기술하였다. 본 논문은 보고된 다양한 열전 소재 중에서 n형 SnSe 와 n형 Bi₂Te₃ 소재에 대한 연구 및 새로운 금속 층이 도입된 열전 소자의 효율에 대해서 논의하고자 한다.

먼저, 고유한 p형 전도 특성을 보이는 SnSe 반도체에 n형 전도 특성을 유도하기 위해 Cl과 PbSe를 동시에 도입하였다. PbSe 합금은 역률(power factor)을 향상시킬 뿐만 아니라 동시에 격자 열전도도를 억제하여 823 K 에서 1.2의 최고 ZT 값을 얻을 수 있었다. 놀랍게도, 추가적인 불밀 및 어닐링 공정을 통해서 구조적 이방성을 상당히 감소시킬 수 있었고, 그 결과 양방향에서 비슷한 $ZT_{max} \sim 1.2$ 를 보이는 것을 확인하였다. 즉, 해당 시스템에서 높은 열전 효율을 보이는 방향을 특별한 합성 방법을 통해 조절할 수 있었다. 또한, 구면수차보정 주사투과전자

현미경 분석을 통해서 격자 열전도도를 낮추는데 기여하는 매우 조밀한 edge dislocation과 strain field 를 관측할 수 있었다.

두번째로, 새로운 n 형 Bi_2Te_3 시스템에서 전하 이동도가 $467 \text{ cm}^2 \text{ V}^{-1} \text{ s}^{-1}$ 및 역률이 $\sim 45 \mu \text{ W cm}^{-1} \text{ K}^{-2}$ 값을 가지는 소재를 개발하였다. 해당 소재는 Bi_2Te_3 와 과량의 Cu 및 Te을 함께 반응시킨 후 스파크 플라즈마 소결 (SPS) 장비를 통해 분말 생성물을 가압함으로써 얻을 수 있다. SPS 과정에서 과량의 Te은 방출되지만 높은 함량의 Cu를 구조 내에 안정화 시키는 중요한 역할을 한다. 그 결과 분석된 조성은 " $\text{Cu}_x\text{Bi}_2\text{Te}_3$ "에 가까우며, 독특한 전하 운송 특성을 보인다. 전형적인 전하 산란 메커니즘과는 다르게 전하 농도 및 이동도가 Cu의 함량에 따라 동시에 증가하는 것을 확인하였다. 그 결과, 전기 전도도가 Cu 도입을 통해 상당히 향상되었다. 하지만 전기 전도도와 제벡 계수 사이의 일반적인 이해와는 반대로 Cu 함량이 증가함에 따라 제벡 계수는 거의 변하지 않았다. 이러한 효과들이 협력적으로 작용하여 매우 높은 곱률을 얻을 수 있었으며, 이 값은 다결정 n형 비스무스 텔루라이드 중 가장 높은 값이다.

마지막으로, 보고 된 대부분의 열전 소자의 경우 열전 소재와 금속 전극 사이의 인터페이스에서 발생하는 높은 전기 및 열 저항으로 인해 상당한 전력 손실이 발생한다. 본 연구에서는 Skutterudite 재료와 금속 전극을 완벽하게 고정하는 Fe-Ni 합금의 금속 층을 고안하여 전달되는

에너지 손실을 최소화 시켰다. 개발한 금속 층은 계면에서의 화학 반응을 억제하는 확산 방지막 역할을 하는 것을 확인하였다. 결과적으로 개발한 소자는 보고된 값 중 가장 낮은 전기 접촉 저항을 가지며 ($2.2\text{--}2.5 \mu\text{C cm}^2$), 온도 차이가 570K 에서 2.1W cm^{-2} 의 높은 열전 전력 밀도를 보였다. 우리는 열전 모듈의 에너지 전달과 열 안정성에 유해한 2차상의 형성이 무시할 수준인 것을 주사투과전자현미경 분석을 통해 확인하였다.

주요어 : 열전, 다결정, n-형, 틴 셀레나이드, 비스무스 텔러라이드, 소자.

학 번 : 2015-31028